

# **DILUTION JET MIXING PROGRAM PHASE III REPORT**

by

**R. SRINIVASAN  
G. MYERS  
E. COLEMAN  
C. WHITE**

**Garrett Turbine Engine Company**  
A Division of the Garrett Corporation

**September 1985**

Prepared for

**National Aeronautics and Space Administration  
NASA-Lewis Research Center**

**Contract NAS3-22110**

## TABLE OF CONTENTS

	<u>Page</u>
1.0 SUMMARY	1
2.0 INTRODUCTION	3
3.0 TEST RIG AND FACILITY DESCRIPTION	7
3.1 Test Rig	7
3.1.1 Test Sections	8
3.1.2 Dilution Orifice Plate Geometry	8
4.0 DATA ACQUISITION AND REDUCTION	11
4.1 Data Acquisition	11
4.2 Data Reduction	12
5.0 EXPERIMENTAL DATA DISCUSSION	19
5.1 Series 9 Tests	19
5.1.1 Test Series 9 Conclusions	31
5.2 Series 10 Tests	34
5.2.1 Test Series 10 Conclusions	43
6.0 JET MIXING CORRELATION DEVELOPMENT	47
6.1 NASA/Garrett Correlations for Multiple Rows and Non-Circular Jets	49
6.1.1 Empirical Model for Mixing of Double Row of Dilution Jets in a Confined Cross Flow	49
6.1.2 Empirical Model for Mixing of a Row of Non-Circular Jets in a Confined Cross Flow	55
7.0 CONCLUSIONS AND RECOMMENDATIONS	59
REFERENCES	63
LIST OF SYMBOLS	65
APPENDIX A	121

## LIST OF FIGURES

<u>Figure</u>	<u>Title</u>	<u>Page</u>
1	Multiple Jet Study Coordinate System and Important Nomenclature	67
2	Dilution Jet Mixing Rig Schematic and Orifice Plates	68
3	Wall Statics and Thermocouples in the Test Section	69
4	Dilution Orifice Plate Configurations	70
5	Total Pressure, Thermocouple, and Static Pressure Rake	71
6	X-Y-Z Actuator with the Rake Mounted Thereon	72
7	Jet Mixing Rig as Viewed from Rig Discharge End	73
8	Measured Theta Distribution for Test No. 1	75
9	Predicted Theta Distributions for Test No. 1	76
10	Measured Theta Distributions for Test No. 2	77
11	Predicted Theta Distributions for Test No. 2	78
12	Measured Theta Distributions for Test No. 3	79
13	Predicted Theta Distributions for Test No. 3	80
14	Measured Theta Distributions for Test No. 4	81
15	Predicted Theta Distributions for Test No. 4	82
16	Measured Theta Distributions for Test No. 5	83
17	Predicted Theta Distributions for Test No. 5	84
18	Measured Theta Distributions for Test No. 6	85
19	Predicted Theta Distributions for Test No. 6	86
20	Measured Theta Distributions for Test No. 7	87
21	Predicted Theta Distributions for Test No. 7	88

# LIST OF FIGURES (Contd)

<u>Figure</u>	<u>Title</u>	<u>Page</u>
22	Measured Theta Distributions for Test No. 8	89
23	Predicted Theta Distributions for Test No. 8	90
24	Measured Theta Distributions for Test No. 9	91
25	Predicted Theta Distributions for Test No. 9	92
26	Measured Theta Distributions for Test No. 10	93
27	Predicted Theta Distributions for Test No. 10	94
28	Measured Theta Distributions for Test No. 11	95
29	Predicted Theta Distributions for Test No. 11	96
30	Measured Theta Distributions for Test No. 12	97
31	Predicted Theta Distributions for Test No. 12	98
32	Measured Theta Distributions for Test No. 13	99
33	Predicted Theta Distributions for Test No. 13	100
34	Measured Theta Distributions for Test No. 14	101
35	Predicted Theta Distributions for Test No. 14	102
36	Measured Theta Distributions for Test No. 15	103
37	Predicted Theta Distributions for Test No. 15	104
38	Measured Theta Distributions for Test No. 16	105
39	Predicted Theta Distributions for Test No. 16	106
40	Measured Theta Distributions for Test No. 17	107
41	Predicted Theta Distributions for Test No. 17	108
42	Measured Theta Distributions for Test No. 18	109
43	Predicted Theta Distributions for Test No. 18	110
44	Measured Theta Distributions for Test No. 19	111
45	Predicted Theta Distributions for Test No. 19	112



# LIST OF FIGURES (Contd)

<u>Figure</u>	<u>Title</u>	<u>Page</u>
46	Measured Theta Distributions for Test No. 20	113
47	Predicted Theta Distributions for Test No. 20	114
48	Measured Theta Distributions for Test No. 21	115
49	Predicted Theta Distributions for Test No. 21	116
50	Measured Theta Distributions for Test No. 22	117
51	Predicted Theta Distributions for Test No. 22	118
52	Schematic of Typical Vertical Theta Profile	119
53	Theta Distributions Obtained from NASA/Garrett Correlation for Angled Slots.	120

## LIST OF TABLES

<u>Table</u>	<u>Title</u>	<u>Page</u>
1	ORIFICE PLATE CONFIGURATIONS	9
2	SERIES 9 TEST CONFIGURATIONS AND FLOW CONDITIONS WITH TEST SECTION I.	20
3	SERIES 10 TEST CONFIGURATIONS AND FLOW CONDITIONS	36

## 1.0 SUMMARY

The main objectives of the NASA Dilution Jet Mixing Phase III Program were as follows:

- o Extend the data base on mixing of single-sided row of jets in a confined cross flow to discrete slots including streamlined, bluff and angled slots
- o Quantify the effects of geometrical and flow parameters on penetration and mixing of multiple rows of jets into a confined cross flow. Investigate in-line, staggered and dissimilar hole configurations
- o Determine the effects of unequal flow rates through double row of jets
- o Develop empirical correlations for predicting temperature distributions for discrete slots as well as multiple rows of dilution holes

The general conclusions derived from Phase III efforts are:

- o Jet penetrations and mixing characteristics of streamlined and bluff slots are similar to those of equivalent area circular holes with the same  $S/H_0$  value at constant momentum flux ratio.
- o The jet penetration and mixing rates for 45-degree slots are lower than those of equivalent area circular holes, streamlined, or bluff slots.
- o The 45-degree slots generate skewed vortex field, which shifts the jet centerplanes along the slot centerline.

In addition, the vortex field rotates the temperature contours about the axis of the slot.

- o Temperature fields due to double row of jets are very similar to those of equivalent single row of circular jets at the same momentum flux ratio.
- o The temperature profile development with double row of jets is dominated by the leading row of jets.
- o The empirical model developed in this phase, predicts the temperature distributions due to axially-staged jets and non-circular jets within engineering accuracy. These models have provided a valuable extension of existing empirical models to analyze practical dilution zone configurations. They provide a very useful first-order tool for designing gas turbine dilution zones.

## 2.0 INTRODUCTION

Advanced technology gas turbine engines require increased thrust or horsepower per unit mass airflow rate. With the improvements in manufacturing technology of surface coating and other high-temperature materials, emphasis has been directed toward increasing combustor exit temperatures. Increases in combustor exit temperatures are often achieved with reduction of available dilution air. This necessitates effective use of the available dilution air to meet the combustor discharge temperature distribution requirements.

The combustor discharge temperature quality is influenced by nearly all aspects of the combustor design and in particular by the dilution zone. To tailor the combustor discharge temperature pattern, the discharge temperature distribution must be characterized in terms of the dilution zone geometric and flow parameters. Such characterization requires an improved understanding of the dilution jet mixing processes.

Considerations of dilution zone mixing in gas turbine combustors have motivated several studies of multiple jets injected into a confined cross flow to identify the dominant flow and geometric parameters governing the mixing. For example, the studies reported in References 1 to 5 investigated the mixing characteristics of a single row of jets injected normally into an isothermal flow of a different temperature in a constant area duct. Recent experiments reported in references 6 to 9 extended the previous studies to investigate the role of several flow and geometric variations typical of gas turbine combustion chambers, namely variable temperature mainstream, flow area convergence,

and opposed in-line and staggered injection. Based upon these experiments, empirical correlations have been developed to characterize the dilution-zone temperature distributions. These empirical correlations provide a valuable tool to the combustor designer for modifying the dilution zone geometries to meet the combustor-exit temperature profile quality. The correlations developed in these investigations are applicable only within the range of experimental configurations. Extrapolation of these results outside the range of the test conditions can lead to large errors.

Although these investigations covered a wide range of values of geometrical and flow parameters, they do not include several configurations frequently used in practical gas turbine systems. Many gas turbine engines use multiple rows of dilution jets. The investigations reported in References 1 through 9 are limited to only a single row of jets. For small gas turbine applications, it is possible to encounter situations where the dilution holes may require very small hole spacing, which would make the combustor liner structurally weak. In such circumstances, it is feasible to employ discrete slots instead of circular holes. These slots can be streamlined, bluff, or angled with respect to the hot-gas stream. A data base on such configurations is not available in the open literature. This phase of the Dilution Jet Mixing Program has been undertaken to acquire a data base on these practical dilution zone configurations.

The NASA Dilution Jet Mixing Program was a three phase effort to provide data base on the effect of dilution zone orifice pattern and geometry on mixing. The results of the first two phases have previously been reported.

The objective of Phase I was to quantify the effect of density ratio, flow area convergence, and nonuniform mainstream profile on the mixing of a single row of jets with a confined cross flow. The temperature field results of this study are reported in reference 6.

The objectives of Phase II were to extend the data base on the mixing of a single-sided row of jets in a confined cross flow and to quantify the mixing of opposed jets in a confined cross flow. The temperature field results of this study are reported in reference 7.

The main objectives of NASA Dilution Jet Mixing Phase III Program were as follows:

- o Extend the data base on mixing of single-sided row of jets in a confined cross flow to discrete slots including streamlined, bluff and angled slots
- o Quantify the effects of geometrical and flow parameters on penetration and mixing of multiple rows of jets into a confined cross flow. Investigate in-line, staggered and dissimilar hole configurations
- o Determine the effects of unequal flow rates through double row of jets
- o Develop empirical correlations for predicting temperature distributions for discrete slots as well as multiple rows of dilution holes

The results of this investigation are reported herein. The description of the experimental setup is presented in Section 3.0. Data acquisition and reduction details are presented in Section 4.0. Test results and the predictions obtained from the correlations are presented in Section 5.0. The details of the correlation are presented in Section 6.0 and conclusions and recommendations are provided in Section 7.0.



### 3.0 TEST RIG AND FACILITY DESCRIPTION

#### 3.1 Test Rig

The jet mixing test rig schematic layout is presented in Figures 1 and 2. The mainstream airflow is ducted from the test cell main air supply through a 15.24 centimeter (cm) internal diameter pipe. A transition section connects the inlet pipe to a rectangular cross section of constant width (30.48 cm) and adjustable height.

A perforated plate with 25 holes of 1.43-cm diameter provides a relatively uniform airflow in the mainstream. The mainstream duct has an adjustable bottom wall to match the test section inlet height, which can vary from 10.16 to 15.24 cm.

A separate air supply feeds the dilution jet orifices. The dilution orifices are mounted on the end of a plenum, which is attached to the top wall of the test section. The dilution jet plenum includes a perforated plate to ensure uniform distribution of air flow to all the jet orifices.

The rig walls are insulated with a 2.54-cm thick layer of Kaolite insulation to minimize the rig heat losses.

The rig instrumentation includes a number of wall static pressure taps and flow thermocouples in addition to a traversing  $P_t/P_s/T$  rake, as shown in Figure 2.

A brief description of the test section and the dilution orifice plates is provided in the following paragraphs.

### 3.1.1 Test Sections

In the present investigation, all the tests were performed in a constant area rectangular duct with a constant channel height,  $H_0$ , of 10.16 cm. The test section had a length of slightly more than  $2H_0$  to allow vertical profile measurements at  $X/H_0 = 0.25, 0.5, 1.0$  and  $2.0$ .

To provide a well-controlled boundary layer profile at the injection plane, a boundary-layer trip (0.41-cm high and 0.33-cm wide) was welded to the four walls of the test sections. The trip is located 15.24 cm upstream of the jet injection plane.

A number of static pressure taps are installed on the four walls of the test sections. As indicated in Figure 3, a total of 32 wall taps were used to measure static pressure distribution. Four thermocouples (two thermocouples extending from the top wall and two through the bottom wall) were used for monitoring the mainstream gas temperature levels. These thermocouples were immersed 1.27 and 3.81 cm from the bottom and top walls, respectively.

### 3.1.2 Dilution Orifice Plate Geometry

Seven different orifice configurations were used in this investigation. Table 1 gives the important dimensions of the orifice plates. These orifice plates are also illustrated in Figure 4. In Table 1,  $S$  represents the orifice spacing along the jet injection plane and  $S_x$  represents the spacing between rows of jets. The aspect ratio of these orifices (defined as frontal width/streamwise length) is unity for circular holes and is different for the other orifice plates as shown in Table 1.

TABLE 1. ORIFICE PLATE CONFIGURATIONS.

Plate	Row	$S/H_0$	AR*	$A_j/A_m$	Angle	$S_x/H_0$	Dia (cm)
M-1	1	0.5	0.36	0.098	0	0	2.54
M-2	1	0.5	2.8	0.098	90	0	2.54
M-3	1	0.5	1	0.049	0	-0.25	1.80
	2	0.5	1	0.049	0	+0.25	1.80
M-4	1	1	1	0.049	0	-0.25	2.54
	2	1	1	0.049	0	+0.25	2.54
M-5	1	0.5	1	0.049	0	-0.125	1.80
	2	0.25	1	0.049	0	+0.125	1.27
M-6	1	0.25	1	0.049	0	-0.125	1.27
	2	0.5	1	0.049	0	+0.125	1.80
M-7	1	0.5	1	0.098	45	0	2.54
01/02/04	1	0.5	1	0.098	0	0	2.54

\*AR = Frontal width/streamwise length.

All of the orifice plates tested in this phase had the same total jet-to-mainstream area ratio,  $A_j/A_m$ , of 0.098. For the tests involving axially staged jets, each row of jets had an area ratio of 0.049. All of these plates have the same geometric area as the orifice plate designated by 01/02/04 ( $S/D = 2$ ,  $H_0/D = 4$ ), where  $H_0$  (test section height) = 10.16 cm.

For the majority of the test cases the nominal mainstream temperature and flow rate were 644K and 0.27 kilogram/second (kg/sec), respectively. The mainstream temperature was measured by thermocouples located at the test-section entrance. A standard ASME orifice section installed in a 15-cm inside diameter pipe was used for measuring the mainstream airflow rate.

A second air supply was used for controlling the dilution-jet flow conditions. The dilution-jet temperature was maintained at the ambient temperature and no external heater was required for the test cases. The dilution air flow rates were measured using a standard bellmouth nozzle section.

## 4.0 DATA ACQUISITION AND REDUCTION

### 4.1 Data Acquisition

The dilution jet mixing characteristics were determined by measuring temperature and pressure distributions within the test section at different axial stations. A traversing probe (Figure 5) was used for this purpose.

The probe consists of a 20-element thermocouple rake with 20 total-pressure sensors on one side and 20 static-pressure rakes on the other side. The nominal transverse spacing between the thermocouple rake and the total pressure rake is 0.508 cm. The spacing between the thermocouple and the static pressure elements is 0.508 cm.

The center-to-center height of the probe is 9.35 cm. The first element is located 0.405 cm from the top wall of the constant-height test section. All the elements are equally spaced in the vertical direction, providing a nominal spacing of 0.492 cm.

The total-pressure sensor elements are made of Inconel tubes with an outside diameter of 0.16 cm and a wall thickness of 0.023 cm. The internal conical design of the tube at the inlet provides a  $\pm 15$  degree flow insensitivity angle. The static pressure tubes, similar to the total pressure sensors, are dead-ended with four bleeding holes of 0.03-cm diameter, 90 degrees apart and 0.7 cm from the tip. The total temperature sensors are type-K thermocouple wires with insulated junctions encased in 0.10-cm inside diameter tubes, supported by 0.21 cm inside

diameter enveloping tubes. The insulated junction tubes exposed to the air stream are 0.76-cm long. The sensing elements have a straight length of 1.52 cm or more before the first bend to the probe core where all tubes are inserted in a rectangular probe shield, 4.32 x 0.67 cm.

The probe is mounted on a traversing system (Figure 6) that allows travel in three directions. This system allows for a 30.48 cm traverse in the X-direction (mainstream flow direction) and 22.86 cm in the radial (Y) and transverse (Z) directions with an accuracy of  $\pm 0.015$  percent (References 1 and 2). The flow field mapping in the Z direction is done over a distance equal to the hole spacing (S) for any given orifice plate. The measurements in the Z direction for single-sided injections and in-line configurations with axially staged injection were made at the eleven transverse planes identified by  $Z/S = -0.5, -0.4, -0.3, -0.2, -0.1, 0, 0.1, 0.2, 0.3, 0.4, \text{ and } 0.5$ , where  $Z/S = 0$  denotes the center of the orifice. For the staggered configuration with double row injection, the measurements were made at a total of sixteen transverse planes made at  $Z/S = -0.5$  to  $1.0$  at intervals of  $0.1$ . The measurements in the X-direction were made at the four axial planes  $X/H_0 = 0.25, 0.5, 1.0, \text{ and } 2.0$ . The probe was traversed over a matrix of  $11 \times 4$  survey locations for single row or in-line orifice configurations and  $16 \times 4$  for staggered configurations with two rows of injection.

The temperature and pressure values from the test rig instrumentation were recorded on magnetic tape through a central computerized data acquisition system. An on-line data display system provided real-time information on selected raw data for monitoring the flow conditions. The raw data from the magnetic

tape was later used for detailed data reduction, analysis, and correlation.

#### 4.2 Data Reduction

The rectangular grid network at which the measurements were made can be described with the aid of Figures 6 and 7. The X-axis is the axis along the length of the duct in the direction of the main flow. The X=0 station is located at the jet injection plane. For double row of jets, the X = 0 station is located midway between the two rows. The Y-axis (radial or vertical direction) is the direction along the jet injection direction. The Y=0 plane is located at the top jet orifice exit plane. The Z-axis is in the cross-stream direction. The Z=0 plane is the vertical X, Y plane at a jet centerline. The streamwise (X) and radial (Y) distances are nondimensionalized by  $H_0$ , the channel height at the jet injection plane. The transverse distance, Z, is nondimensionalized by S, the dilution orifice spacing.

The measured gas temperature distributions are presented in a nondimensionalized form as:

$$\theta(X, Y, Z) = \frac{T_m - T(X, Y, Z)}{T_m - \bar{T}_j}$$

where,

$T_m$  or TMAIN = Mainstream stagnation temperature

$\bar{T}_j$  or TJET = Average jet stagnation temperature

$T(X, Y, Z)$  = Stagnation temperature at the point  $(X, Y, Z)$  in the flow field.

$\theta$  is a measure of the temperature change due to the jet injections at any point  $(X, Y, Z)$  compared to the maximum possible temperature change and can vary from 0.0 to 1.0.  $\theta$  is equal to zero when the local temperature equals the mainstream temperature; and  $\theta$  is 1.0 when the local temperature equals the jet temperature. When the jet and the mainstream are perfectly mixed, the local temperature reaches ideal equilibrium temperature,  $T_{EB}$ , given by:

$$T_{EB} = \frac{\dot{m}_m T_m + \dot{m}_j T_j}{\dot{m}_m + \dot{m}_j}$$

The ideal equilibrium temperature difference ratio ( $\theta_{EB}$  or  $T_{HEB}$ ) is defined as:

$$\theta_{EB} = \frac{T_m - T_{EB}}{T_m - T_j}$$

By using the definition for  $T_{EB}$ , it can be seen that

$$\theta_{EB} = \dot{m}_j / (\dot{m}_j + \dot{m}_m)$$

The parameter,  $\theta_{EB}$ , provides a measure of the quality of the jet mixing. The arithmetic average temperature ( $T_{av}$ ) at any  $X$  plane and the corresponding  $\theta_{av} = (T_m - T_{av}) / (T_m - T_j)$  are also presented with the reduced data to provide the information on the average value of the temperature field at that plane.



The measured  $\theta$  values are presented in 3-D (oblique) plots and isotherm contour plots at each X-station. The oblique plots provide a convenient means of presenting the jet trajectory and mixing and the isotherms provide a more quantitative representation for comparison with correlations. These plots are presented over a  $2S$  span in the  $Z$  direction by assuming symmetry of the  $\theta$  distribution with respect to the midplane between two orifices. This assumption was invoked only for the purpose of improving the clarity of visual presentation of the temperature distribution. The accuracy of this assumption depends upon the uniformity of the flow distribution across the jet orifices. Preliminary tests were performed to ensure that the mainstream and the jet mass flows were uniformly distributed over the entire width of the test section. A comparison of the data and correlations is presented in a radial profile of  $\theta$  versus  $Y/H_0$  along the jet centerplane at each of the measured  $X/H_0$  stations.

The pressure recordings from the probe rake were used to compute the velocity  $V(X,Y,Z)$  at the point  $(X,Y,Z)$ . An interpolation scheme was used to compute pressure ( $P_s$ ) values at the point where probe thermocouples are located. From these total and static pressures, a nondimensionalized velocity,  $[V(X, Y, Z) - V_m]/V_j$ , was computed.  $V(X,Y,Z)$  is obtained from:

$$V(X,Y,Z) = 2 \left\{ [P_t (X,Y,Z) - P_s (X,Y,Z)]/\rho(X,Y,Z) \right\}^{0.5}$$

The jet velocity,  $V_j$ , is calculated from:

$$V_j = 4 \dot{m}_j / \rho_j N \pi D^2 C_D$$

where  $D$  is the orifice diameter,  $N$  is the number of orifices,  $\rho_j$  is the jet density ( $P_j/RT_j$ ), and  $C_D$  is the orifice discharge coefficient.

The mainstream velocity,  $V_m$ , is calculated from:

$$V_m = (\dot{m}_m / \rho_m A_m)$$

where  $\rho_m$  is the mainstream density ( $P_m/RT_m$ ) and  $A_m$  is the mainstream effective area.

The orifice discharge coefficients were determined by measuring the pressure drop across the orifice plate (without cross-flow) for a range of mass flow rates. The discharge coefficient,  $C_D$ , was obtained from the relation:

$$\frac{\Delta P}{P} = 1.99 \left( \frac{\dot{w}_c}{AC_D} \right)^2$$

where,  $\dot{w}_c$  is the corrected flow rate in  $\text{lbm/sec}$  and  $A$  is the geometric area of the orifices in square inches.

Note:  $\dot{w}_c = \dot{w}_a \frac{\sqrt{\beta}}{\delta}$ ,  $\beta = \frac{T(OR)}{517}$ , and  $\delta = \frac{P(\text{psi})}{14.696}$

The velocity vector in the vicinity of the jet injection plane is predominantly in the radial direction. In such regions, the velocity values obtained from the rake probe are not expected to be accurate. For the sake of brevity, the measured velocity distributions are not presented in this report. However, tables of non-dimensional velocity distribution,  $[V(X,Y,Z) - V_m]/V_j$ , are provided for each test case in the Comprehensive Data Report (CDR) for this program.

An important parameter relevant to the jet penetration and mixing is the jet momentum flux ratio,  $J$ , defined as:

$$J = \rho_j V_j^2 / (\rho_m V_m^2)$$

where:

$$\rho_j = \text{Jet density} = P_j / RT_j$$

$$\rho_m = \text{Mainstream density} = P_m / (RT_m)$$

$$V_j \text{ or } V_{JET} = \text{Jet velocity at the orifice vena contracta}$$

$$V_m \text{ or } V_{MAIN} = \text{Mainstream Velocity} = \dot{m}_m / (\rho_m A_m)$$

$$A_m = \text{Cross-sectional area of the duct.}$$

Other flow parameters of interest are:

$$\text{Blowing rate, } M \text{ or } BLORAT \text{ (mass flux ratio)} = \rho_j V_j / \rho_m V_m$$

$$\text{Temperature ratio, } TRATIO = T_j / T_m$$

$$\text{Density ratio, } DENRATIO = \rho_j / \rho_m$$

$$\text{Velocity ratio} = V_j / V_m$$

The geometric parameters of importance associated with the orifice configuration are:  $S/D_j$  and  $H_0/D_j$ , where  $D_j$  is the effective jet diameter defined by:

$$D_j = D \sqrt{C_D}$$

The quantities described in this section define the geometric and flow conditions of each test and are reported along with the reduced data.

The average mainstream velocity,  $V_m$  and the average jet velocity,  $V_j$ , are mass weighted average values for the test. They represent the correct momentum flux for the mainstream and the jet respectively. For the two rows of injections, this procedure is adopted for the front and the aft injections while reducing the test data. The results are presented in nondimensional form for the two rows of injection as:

$$\theta = \frac{T_m - T}{T_m - \overline{T}_j} ,$$

where,  $\overline{T}_j = (T_{jF} + T_{jA}) / 2$

with  $T_{jF}$  and  $T_{jA}$  being the stagnation temperatures of the front and aft jets, respectively.

## 5.0 EXPERIMENTAL DATA DISCUSSION

The Phase III test program was divided into two test series (Series 9 and 10). Series 1 through 8 testing was conducted during Phase I and Phase II programs (References 6 and 7). For each of the Phase III tests, the measured data and predictions obtained from the correlations are discussed in the following paragraphs. Paragraph 5.1 provides the discussion of results obtained in Series 9. The Series 10 results are discussed in paragraph 5.2.

### 5.1 Series 9 Tests

The purpose of this test series was to investigate the jet mixing characteristics of discrete slotted jets and double rows of jets with equal momentum flux ratios injected into an isothermal, hot confined cross flow in a straight duct with a channel height of 10.16 cm. A total of 12 tests were performed in this test series. The geometrical orifice description and the nominal flow conditions for these tests are listed in Table 2. In Phase III tests, the dilution jets were injected from the top wall of the test section.

Test No. 1 was performed with streamlined slots (orifice plate M-1). The momentum flux ratio of the jets ( $J$ ) for this test was 6.60. Figure 8 shows the measured distribution of non-dimensional temperature difference ( $\theta$  or  $\theta$ ) for test No. 1.

The top half of Figure 8 shows the oblique plot of the  $\theta$  profiles at four axial stations of  $X/H_0 = 0.25, 0.5, 1.0$  and  $2.0$ . The bottom half of the figure provides the measured  $\theta$  contours for the corresponding stations.

TABLE 2. SERIES 9 TEST CONFIGURATIONS AND FLOW CONDITIONS<sup>†</sup> WITH TEST SECTION I.

Test No.	Orifice Plate	* Orifice Dia (CM)	S H <sub>0</sub>	MAINSTREAM				FORE DILUTION JET				AFT DILUTION JET				REGIONS OF MEASUREMENT		
				Mass Flow Rate (KG/S)	Temp (T <sub>MAIN</sub> ) (°K)	Velocity (V <sub>MAIN</sub> ) (M/S)	Mass Flow Rate (KG/S)	Velocity (V <sub>JP</sub> ) (M/S)	Momentum Flux Ratio J <sub>F</sub>	Temp (T <sub>JP</sub> ) (°K)	Mass Flow Rate (KG/S)	Momentum Ratio J <sub>A</sub>	Temp (T <sub>JA</sub> ) (°K)	Velocity (V <sub>JA</sub> ) (M/S)	(C <sub>p</sub> ) <sub>A</sub>	Equilibrium Theta (THEB)	Axial Direction X/H <sub>0</sub>	Transverse Direction Z/S
1	M-1	2.54	0.5	0.2683	690.1	17.8	0.07637	6.60	317.1	30.9	0.764	-	-	-	0.2216	0.25 - 2.0	-0.5 to +0.5	
2	M-1	2.54	0.5	0.2661	661.0	16.7	0.1339	26.47	307.3	58.5	0.707	-	-	-	-	0.3447	-0.5 to +0.5	
3	M-2	2.54	0.5	0.2676	675.0	17.2	0.1803	26.59	316.5	60.3	0.904	-	-	-	-	0.4026	-0.5 to +0.5	
4	M-2	2.54	0.5	0.2025	655.3	12.6	0.2690	106.5	315.0	88.6	0.891	-	-	-	-	0.5705	-0.5 to +0.5	
5	M-3	1.80	0.5	0.2674	690.3	17.7	0.03302	6.65	319.2	30.9	0.662	0.03291	6.63	320.5	30.95	0.662	0.1978	-0.5 to +0.5
6	M-3	1.80	0.5	0.2687	665.9	17.1	0.06488	26.27	310.4	59.2	0.650	0.06555	26.85	310.9	59.9	0.650	0.3268	-0.5 to +0.5
7	M-3	1.80	0.5	0.2681	636.7	16.3	0.1231	107.2	309.6	113.9	0.611	0.1224	106.0	310.2	113.2	0.611	0.4780	-0.5 to +0.5
8	M-4	2.54	1.0	0.2668	682.0	17.4	0.03596	6.67	314.0	30.4	0.719	0.03715	6.32	314.1	29.6	0.764	0.2151	-0.5 to +0.5
9	M-4	2.54	1.0	0.2694	671.6	17.3	0.06567	26.77	313.5	60.7	0.649	0.06786	26.68	314.8	60.8	0.675	0.3314	-0.5 to +0.5
10	M-5	1.80	0.5	0.2672	695.5	17.8	0.03730	6.72	321.1	31.2	0.744	0.03781	6.67	320.4	31.1	0.756	0.2194	-0.5 to +0.5
11	M-5	1.80	0.5	0.2675	677.2	17.3	0.06911	26.79	313.5	60.2	0.685	0.07006	26.63	312.9	60.1	0.700	0.3422	-0.5 to +0.5
12	M-5	1.80	0.5	0.2670	645.0	16.4	0.1310	106.3	313.7	113.3	0.651	0.1365	106.4	313.2	114.7	0.685	0.5004	-0.5 to +0.5

\* Equivalent circular hole diameter

† See Table 1 for geometrical descriptions of orifice plates.

The mixing performance for any given configuration can be assessed from the deviation of the theta distribution about the ideal equilibrium value  $\theta_{EB}$ . A small deviation from  $\theta_{EB}$  characterizes nearly complete mixing of the jets and the mainstream. For Test 1, the value of  $\theta_{EB}$  is 0.2216, which corresponds to contour 5 in Figure 8.

At  $X/H_0 = 0.25$ , the jets penetrate to about 50 percent of the local duct height. The streamlined slots show the familiar kidney-shaped symmetric vortex structure behind the jets. These vortices entrain the mainstream, interact with adjacent jets, and gradually approach equilibrium conditions. As the mixing process progresses, the jets spread in both vertical (Y) and transverse (Z) directions. The jet spreading in a transverse direction can be inferred from the smoothness of the theta contour shapes. In Test No. 1, the jet spreading rate in the transverse direction is faster than the rate in the vertical direction. In the vertical direction, most of the jet spreading occurs towards the injection wall. Near the bottom wall of the test section, the theta values are essentially zero, which corresponds to hot-mainstream conditions. In the wake region behind the jets, the theta values are larger, which is indicative of the effects of jet spreading.

The streamlined slots have the same geometric area and  $S/H_0$  value as orifice plate 01/02/04 ( $S/D = 2$  and  $H_0/D = 2$ ). The latter orifice plate was tested in Phase I at comparable momentum flux ratio (Figure 12, Reference 6). Comparison between the data for streamlined slots and orifice plate 01/02/04 at low-momentum flux ratios shows that in the near field ( $X/H_0 < 1$ ), the streamlined slots have deeper jet penetration than the circular holes. However, in the far field ( $X/H_0 > 1$ ), the two orifices have very similar theta distributions.

Figure 9 presents the predicted theta distributions for Test No. 1 obtained from the empirical correlations. The correlations

are developed based upon the expressions given in Reference 7. Details of this development are described in Paragraph 6.1. For discrete slots, the jet penetration expressions were modified to include the effects of aspect ratio (defined as frontal width/streamwise length). In Figure 9, the top part illustrates the predicted theta distributions, while the bottom part illustrates the comparison between measured and predicted centerplane theta profiles. The predictions are represented by solid lines and the symbols correspond to the data. The predicted theta distributions underestimate the jet spreading in the transverse direction. This is partially due to the form of the distribution used in the transverse direction (Equation 23). For streamlined slots, the validity of Gaussian profile in the vertical direction is questionable. The predicted results slightly overestimates the jet spreading in the vertical direction. However, the predicted theta distributions are in agreement with the data within engineering accuracy.

Figure 10 shows the measured theta distributions for Test No. 2 with single-sided injection using streamlined slots. In this test case, the jet-to-mainstream momentum flux ratio is 26.47, and the value of  $\theta_{EB}$  is 0.3447. The value of  $\theta_{EB}$  also represents the ratio of jet-to-total mass flow rates. At  $X/H_0 = 0.25$ , the jets penetrate to about 70 percent of the local duct height. The jets gradually penetrate deeper downstream and reach the opposite wall at  $X/H_0 = 1.0$ . Beyond that station, the jet spreading rates are enhanced in both the vertical and transverse directions. A similar test was conducted in Phase I using the equivalent area circular jets with the same  $S/H_0$  ratio, namely, orifice plate 01/02/04 (Reference 6, Figure 14). While evaluating the Phase I test results, it was discovered that the momentum flux ratio reported for that test case was incorrect. To provide a baseline comparison for non-circular jets, a test was conducted in Phase III with orifice plate 01/02/04 at  $J=26.4$ . The results for that test are presented in Figure 50. Comparison



of the data for streamlined slots and equivalent area circular orifices show very similar theta distributions beyond  $X/H_0 = 0.5$ . In the region closer to the jet injection plane, the streamlined slots show deeper jet penetration than circular jets.

The predicted theta distributions for Test No. 2, obtained from empirical correlations, are presented in Figure 11. As observed in Figure 9, the predicted results underestimate the jet spreading rate in the transverse direction. The measured center-plane profiles for streamlined slots do not show a Gaussian distribution. Despite the lack of validity of the Gaussian profile assumption, the empirical correlations predict the theta distributions for streamlined slots within engineering accuracy.

Test No. 3 used a row of bluff slots (orifice plate M-2). The dilution jets were injected from the top wall of the constant area test section. The jet-to-mainstream momentum flux ratio in Test No. 3 was 26.59. Figure 12 shows the measured theta distributions for this test case. The value of  $\theta_{EB}$  for Test No. 3 was 0.4026.

At  $X/H_0 = 0.25$ , the jets penetrate to about 60 percent of the duct height. This penetration is smaller than that of the streamlined slot (Figure 11). At  $X/H_0 = 1.0$ , the jets penetrate to the opposite wall, followed by rapid mixing in the vertical and transverse directions. In the near field ( $X/H_0 < 1.0$ ), the jet penetration for bluff slots are very similar to those of equivalent area circular holes with  $S/H_0 = 0.5$  (Figure 50). However, the jet spreading rates for bluff slots are slightly slower than streamlined slots, especially in the near field.

The theta distributions calculated from empirical model for Test No. 3 are presented in Figure 13. For bluff slots, the empirical model was modified to account for the slot configuration. These modifications are described in Section 6.1. The

model calculations underestimate the jet penetration as well as the jet spreading rates for bluff slots. The measured center-plane profiles for bluff slots do show a Gaussian profile, unlike those observed for streamlined slots. For the bluff slots, the agreement between data and predictions is poor.

Figure 14 presents the measured theta distributions using bluff slots (orifice plate M-2) at momentum flux ratio of 106.5. For this case, the value of  $\theta_{EB} = 0.5705$ . At  $X/H_0 = 0.25$ , the jets in this test case penetrate to about 80 percent of the duct height. The jets penetrate to the opposite wall at  $X/H_0 = 0.5$ . However, beyond that station, the jet spreading rates are enhanced and produce completely mixed theta distributions at  $X/H_0 = 2.0$ .

The bluff slots have the same geometric area and  $S/H_0$  value as the orifice plate 01/02/04 (circular holes with  $S/D = 2$  and  $H/D = 4$ ). The latter orifice plate was tested at a comparable momentum flux ratio during the Phase III program. The results of that test will be presented later (Figure 48). Comparison of data for bluff slots and equivalent area circular orifices, at high-momentum flux ratio, shows that the jet mixing in the vertical direction is faster for bluff slots than that for circular holes. The data for circular holes show larger vertical gradients than those for bluff slots. This is not apparent at lower momentum flux ratios.

The theta distributions calculated using the empirical model for Test No. 4 are shown in Figure 15. At this high momentum flux ratio, the predicted results slightly overestimate the jet spreading rates in the transverse direction. The empirical model, however, underestimates the jet penetrations for the bluff slots. The measured profiles do not exhibit a Gaussian distribution for this test case. The predicted profiles for this test are in poor agreement with data.

The next three tests were conducted using the orifice plate M-3. This orifice plate consists of two rows of circular holes in an aligned configuration (Figure 4). Each of the rows is composed of six orifices with a diameter of 1.80 cm, and having orifice spacing to a diameter ratio of 2.83. Spacing between the rows is  $0.5 H_0$ . The total geometric area of each row is  $0.049 A_m$ , where  $A_m$  is the mainstream cross-sectional area ( $A_m = 0.03097 \text{ m}^2$ ). The overall geometric area of this plate is equal to that of orifice plate 01/02/04. The measurements in these cases were made at  $X/H_0 = 0.5, 0.75, 1.0$  and  $1.5$ . For these tests, the axial distances are measured from the mid-plane between the two rows of jets (i.e.,  $X/H_0 = 0$  is  $0.25H$  from the centerline of the lead row).

Test No. 5 was performed with orifice plate M-3 at momentum flux ratios of 6.65 for the first row, and 6.63 for the downstream row of jets. The equilibrium theta value for this test case is 0.1978. This value represents the ratio of jet-to-total mass flow rate. The theta distributions for Test No. 5 (Figure 16), are very similar to those for a single row of equivalent area circular holes (Figure 12, Reference 6). This similarity suggests that superposition of the theta distributions, due to each individual row, may accurately predict the overall distributions for this orifice plate. This approach was adopted for correlating the temperature distributions for multiple rows of jets. This similarity between single and double rows of jets was also observed in Reference 1.

The theta distributions calculated from the empirical model for Test No. 5 are presented in Figure 17. These calculations were obtained by superimposing the theta distributions due to each single row of jets independently. The predicted results correctly estimate the jet penetration and spreading rate in the vertical direction. However, the jet mixing rates in the

transverse direction is underestimated by the model. This is primarily due to the assumption of Gaussian distributions in the off-centerplanes. The overall agreement between data and the empirical model predictions for this test case is very good.

Figure 18 presents the measured data for Test No. 6, using orifice plate M-3 with momentum flux ratios of 26.27 for the first row of jets and 26.85 for the downstream row. The equilibrium theta value for this test case was 0.3268. At  $X/H_0 = 0.5$ , the jet penetration is about 60 percent of the duct height. The jet penetration is established by the lead row. The jets do not penetrate deeper than 60 percent of the duct height at downstream stations. For the case of equivalent single row of jets, at comparable momentum flux ratio (Figure 50), the jets penetrate to the bottom wall of the test section at  $X/H_0 = 1.0$ . One explanation for this characteristic in multiple rows of jets is the influence of a pair of vortices originating from each row of jets which tends to coalesce together, thereby inhibiting further jet penetration. The theta profiles for Plate M-3 and the corresponding profiles for orifice plate 01/02/04 are similar, if the differences in jet penetrations are taken into account.

The predicted results for Test No. 6 are illustrated in Figure 19. The predicted results underestimate the jet penetration at  $X/H_0 = 0.5$ , but gives good agreement with data at the downstream stations. The empirical model slightly overestimates the maximum centerplane theta values, but the jet half widths are accurately estimated. The overall agreement between data and empirical model predictions is within first order accuracy.

Figure 20 illustrates the measured theta distributions for Test No. 7 using orifice plate M-3 with  $J = 107.2$  for the leading row and  $J = 106.0$  for the trailing row. At  $X/H_0 = 0.5$ , the jet penetration is about 75 percent of duct height and at  $X/H_0 = 0.75$ , the jets penetrate to the bottom wall of the duct.

Beyond the impingement station, the jet mixing in the vertical as well as transverse directions is enhanced. These theta distributions are very similar to those for equivalent area single row of holes having the same  $S/H_0$  ratio (Figure 48). This similarity supports the validity of the superposition principle used for predicting theta distributions for multiple rows of jets.

The predicted results for Test No. 7 are presented in Figure 21. The empirical model accurately predicts the jet penetrations for this case. The predicted minimum theta value, at the injection wall is almost 60 percent lower than the data at  $X/H_0 = 0.5$ . This difference between data and model predictions is progressively smaller at the downstream stations. The jet half widths are accurately estimated by the empirical model. The overall correlation between the data and the empirical model predictions is very good.

The next two tests (Test No. 8 and 9) were performed with orifice Plate M-4, which consists of two-staggered rows of orifices with diameters of 2.54 cm, having orifice spacing  $S/D = 4.0$ . The spacing between the two rows is  $0.5 H_0$ . In each row of this plate, there is a total of three orifices with the ratio of total orifice geometrical area to mainstream area of 0.049. The total open area of plate M-4 is the same as the single row of 6 orifices with  $S/D = 2$  and  $H_0/D = 4$  (orifice plate 01/02/04). However, the values of  $S/H_0$  are different for these two plates.

The measured theta distributions for Test No. 8, using orifice plate M-4 with  $J = 6.67$  for the leading row and  $J = 6.32$  for the trailing row, are presented in Figure 22. At  $X/H_0 = 0.5$ , the jets from the lead row penetrate to about 55 percent of the local duct height, while those from the trailing row penetrate to about 35 percent of duct height. The trailing row jets do not penetrate much further, but interact with adjacent jets and the

mainstream. The jets from the leading row penetrate farther across the duct than the equivalent area single row (Plate 01/02/04) of jets (Figure 12, Reference 6). This is mostly due to the larger orifice spacing in the leading row in Plate M-4. The penetration of the trailing row of jets is suppressed by the vortex field of the lead row. At the downstream stations, the temperature fields for Plate M-4 are similar to those from an equivalent area single row (Figure 12, Reference 6), as well as the double row in-line configuration shown in Figure 16.

The theta distributions calculated from the empirical model for Test No. 8 are presented in Figure 23. The calculations are obtained by superimposing the theta distributions due to each individual row of jets. While superimposing the theta distributions for Plate M-4, the centerplanes of the two rows of jets were staggered. Details of this procedure are presented in Section 6.1. The empirical model underestimates the peak theta values, but accurately predicts the jet penetrations. The predicted jet spreading rate in the transverse direction is slower than the data. The agreement between the data and model predictions is poor.

Figure 24 presents the measured theta distributions for Test No. 9, using orifice Plate M-4 with  $J = 26.77$  for the leading row and  $J = 26.68$  for the trailing row. The equilibrium theta value for this test is 0.3314. At  $X/H_0 = 0.5$ , the jets from the lead row penetrate across to the bottom wall of the duct, while the trailing row of jets penetrate to about 50 percent of the duct height. As observed in the last test case, the penetration of the trailing row of jets is suppressed by the vortex field of the leading row of jets. The jet mixing in the transverse direction is enhanced beyond the location of jet impingement on the bottom wall of the duct. In the far field ( $X/H_0 > 1.0$ ), the temperature field for this test case is similar to that for equivalent area single row of holes (Figure 50).

The theta distributions calculated from the empirical model for Test No. 9 are presented in Figure 25. The empirical model underestimates the peak theta values for this case. The data for this case clearly exhibits a non-Gaussian theta profile and hence the superposition of Gaussian profiles would not be expected to give accurate results. However, at the far downstream station ( $X/H_0 = 1.5$ ), the predicted results are in good agreement with the data.

The following three test cases were conducted using orifice plate M-5. This plate consists of two rows of holes with  $S_X/H_0 = 0.25$ , and  $S/H_0 = 0.5$ ,  $H_0/D = 5.66$  in the lead row and  $S/H_0 = 0.25$ ,  $H_0/D = 8$  in the trailing row (Figure 4). Despite the differences in hole diameter and spacing, the two rows of jets have the same total geometric area. The ratio of total orifice area to mainstream area for this plate is 0.098.

Test No. 10 was performed using orifice plate M-5 with  $J = 6.72$  for the lead row ( $S/D = 2.83$ ,  $H_0/D = 5.66$ ) and  $J = 6.67$  for the trailing row of jets ( $S/D = 2.0$ ,  $H_0/D = 8$ ). The station where  $X/H_0 = 0$  is midway between the two rows of jets, or  $0.125 H_0$  downstream of the centerline of the lead row. For this test, the discharge coefficients for the leading and the trailing rows were 0.744 and 0.756, respectively. The measured theta distributions for Test No. 10 are shown in Figure 26. At  $X/H_0 = 0.25$ , the lead row of jets penetrate to about 40 percent of the duct height while the trailing row of jets penetrate to about 20 percent of the duct height. Since the centerplanes of the two rows of jets do not coincide, the effect of the downstream row of jets is primarily to improve the jet mixing in the transverse direction. At the far downstream stations ( $X/H_0 \geq 1.0$ ), the measured temperature field for this test is very similar to the equivalent single row (Figure 12, Reference 6) and the in-line double row of jets (Figure 16). The effects of the downstream row of jets are confined to the near-injection locations ( $X/H_0 < 1$ ).

The predicted results for Test No. 10 are presented in Figure 27. The empirical model predictions are obtained by superimposing the temperature fields due to each individual row of jets. In the regions close to the jet injection plane, the empirical model underestimates the jet penetration. At  $X/H_0 = 0.25$  and  $0.5$ , the measured centerplane theta profiles do not exhibit Gaussian characteristics. At these stations, the empirical model predictions do not correlate well with the data. In the downstream stations, the data show a Gaussian centerplane profile, and the empirical model predictions also show good comparison with the data.

Figure 28 shows the measured theta distributions for Test No. 11 with orifice Plate M-5, having  $J = 26.79$  for the leading row and  $J = 26.63$  for the trailing row of smaller jets. The discharge coefficients for the leading and trailing rows are  $0.685$  and  $0.698$ , respectively. At  $X/H_0 = 0.25$ , the leading row of jets penetrate to about 55 percent of the duct height and penetration of the trailing jets is approximately  $0.35 H_0$ . These values are comparable to those of single rows of jets with orifice plates 01/03/06 ( $S/D = 2.83$ ,  $H_0/D = 5.66$ ), (Reference 7, Figure 123) and 01/02/08 ( $S/D = 2$ ,  $H_0/D = 8$ ), (Reference 6, Figure 20), respectively. This suggests that the jet penetrations are not significantly influenced by axial staging in this orifice configuration. Because of the differences in jet penetrations, the mixing in the vertical direction is enhanced, especially in the regions close to the jet injection station ( $X/H_0 \leq 0.5$ ). At the downstream stations, the temperature field is very similar to those for equivalent single row (Figure 50) or two rows of in-line jets (Figure 18).

The temperature field calculated from the empirical model for Test No. 11 is presented in Figure 29. At  $X/H_0 = 0.25$ , the data show a non-Gaussian centerplane profile, where the empirical model is in poor agreement with the data. At this station, the



model underestimates the jet penetrations due to superposition of the axially-stage injections. At the downstream locations, the model predictions are in good agreement with the data. At these stations, the data also exhibit Gaussian-like centerplane profiles. The good correlation between the empirical model and the data beyond  $X/H_0 = 0.5$  clearly demonstrates the usefulness of the model for designing combustor dilution zones with multiple rows of jets.

Figure 30 illustrates the measured temperature fields for Test No. 12 with orifice plate M-5 at  $J = 106.3$  for the leading row and  $J = 106.4$  for the trailing row of jets. The discharge coefficients for the leading and trailing rows for this test case are 0.651 and 0.685, respectively. The equilibrium theta value for this test case is 0.5004. In this test case, the total jet flow rate is nearly equal to the mainstream flow rate, which is not typical for the dilution zone. This momentum flux rate could be expected to cause overpenetration of the lead row, but, is optimum for the trailing row. At this momentum flux ratio, the lead row of jets should nominally impinge on the bottom wall at  $X/H_0 = 0.25$  and the trailing row of jets should penetrate to the middle of the duct (Figure 22 of Reference 6 and Figure 20). But, the data for Test No. 11 show significant suppression of the jet penetrations of both the rows of jets. Such suppression seems to arise only when the nominal jet penetration for each row is about 50 percent of the duct height or greater. This could provide a minimum value of the vortex strength required for suppression of jet penetrations. At  $X/H_0 = 0.5$ , the leading row of jets impinge on the bottom wall. Beyond that station, the mixing of jets with the mainstream is enhanced. In addition, the mixing in the vertical direction is slightly improved because of the interaction of the vortices created by the two rows of jets. The temperature fields for this test case show overall similarity to those of equivalent single row of jets (Figure 48) or two rows of in-line jets (Figure 21).

The temperature distributions calculated from the empirical model for Test No. 12 are presented in Figure 31. At  $X/H_0 = 0.25$ , the empirical model underpredicts the lead row jet penetration, but, overestimates the jet penetration of the trailing row for this test case. At the downstream regions, the model predictions correlate well with the data.

In all of these test cases performed with Plate M-5, the effects of the mixing characteristics are dominated by the leading row of jets. The influence of the downstream row is confined mostly to the regions near the jet injection plane ( $X/H_0 \leq 0.5$ ).

#### 5.1.1 Test Series 9 Conclusions

The tests in Series 9 were performed with constant cross-sectional area ducts, and uniform mainstream temperature. A total of 5 different orifice plates were tested in this series. They included discrete streamlined and bluff slots, and axially-staged jets with in-line staggered and dissimilar configuration. The tests with double rows of jets had equal momentum flux ratios. The NASA/Garrett empirical model was extended to these test configurations and the model predictions were compared with the test data. The following conclusions were made from these efforts:

- o The jet penetrations of streamlined slots are slightly deeper than the equivalent circular jets in the region near the injection plane ( $X/H_0 < 1$ ). Farther downstream, the temperature field for streamlined slots and equivalent circular holes at constant momentum flux ratio, are very similar.
- o The jet penetrations for bluff slots are slightly less, than for equivalent circular holes and streamlined slots. For  $X/H_0 < 1$ , the bluff slots produce a more

two-dimensional temperature field than the streamlined slots. Farther downstream, the streamlined and bluff slot configurations, and the circular holes, produce very similar temperature distributions.

- o The temperature distributions for double row of in-line jets are very similar to those for single row of jets with the same  $S/H_0$ . The development of temperature profile shape is dominated by the lead row. But, the interaction of the vortices generated by the two rows of jets, tends to suppress the penetrations of the jets in the lead row.
- o For double row of staggered jets, the lead row has a dominant influence on the temperature profile development. In this case, the penetration of the jets in the trailing row is suppressed by the vortex field of the lead row. These effects are predominant in the near field ( $X/H_0 < 1$ ). At the downstream stations, the temperature fields from double row of staggered jets are similar to those from equivalent single row or double row of in-line jets.
- o In the case of a double row of dissimilar jets (Plate M-5), the lead row has a dominant influence on the temperature profile development. In cases, where the trailing row of jets penetrated near mid-channel, the lead row jet penetrations were suppressed. Furthermore, because of the differences in the jet penetrations and orifice configurations of the two rows, the jet mixing in the vertical (or radial) direction is enhanced with this orifice plate. However, in the far field ( $X/H_0 \geq 1.0$ ), the temperature field produced by this orifice configuration is similar to those of equivalent single row of holes or double row of in-line jets.

- o The NASA/Garrett empirical model (Reference 7) was modified to include the effects of aspect ratio on the jet mixing characteristics for predicting the temperature fields due to discrete slots. The modified model predicts the temperature field due to streamlined slots within first order accuracy. For the case of bluff slots, this empirical model gives inferior agreement with the data. Additional work is needed to improve the correlation between the model results and the test data.
- o In the test cases involving axially-staged injections, the similarity between the temperature fields for double row and equivalent single row suggests that superposition of the temperature fields, due to each individual row of jets, could predict the combined field within first order accuracy. This hypothesis is used in developing the empirical model for multiple rows of injections. The empirical model gives good correlation with the data, especially in the far field ( $X/H_0 \geq 1.0$ ). In the regions closer to the jet injection plane, the data show non-Gaussian profiles, which cannot be predicted by the model. However, the empirical model provides a very valuable tool for designing the gas turbine combustor dilution zone configurations.

## 5.2 Series 10 Tests

The objective of this test series was to investigate orifice configurations that were not tested in the earlier test series, and to extend the applicability of the empirical models to wider range of flow conditions. In this test series, a total of 10 tests were performed. The first five tests were performed with double rows of jets having unbalanced momentum flux ratios. These tests were performed primarily for validating and verifying the accuracy of the empirical model. The next three tests were performed using discrete slots angled at 45 degrees to the mainstream. The final two tests were performed to obtain data base on the equivalent area single row of holes with  $S/D = 2$  and  $H_0/D = 4$  (Plate A). The geometrical orifice description and nominal flow conditions for these tests are listed in Table 3.

Test No. 13 was performed using the double row of dissimilar holes, orifice Plate M-5, with  $J = 26.2$  for the lead row of jets ( $S/D = 2.83$ ,  $H_0/D = 5.66$ ) and  $J = 6.36$  for the trailing row of jets ( $S/D = 2$ ,  $H_0/D = 8$ ). For this test case, the discharge coefficients of the leading and trailing rows were 0.683 and 0.756, respectively. The equilibrium theta value for this test case is 0.2820. One of the objectives of this test is to verify the dominant influence of the larger sized lead row of jets on the temperature profile development. The measured temperature field for Test No. 13 is presented in Figure 32. At  $X/H_0 = 0.25$ , the leading row of larger jets penetrate to about 60 percent of the duct height, while the trailing row of jets penetrate to about 20 percent of the duct height. Comparing this to the data for Test No. 11 (Figure 28) which used the same orifice plate (having balanced momentum flux ratios for two rows), it is apparent that because of the large differences in the jet penetrations, the interaction between the leading and the trailing rows of jets is minimal. However, as the trailing jets penetrate deeper at downstream locations, jet mixing is enhanced. Beyond

TABLE 3. SERIES 10 TEST CONFIGURATIONS AND FLOW CONDITIONS

Test No.	Orifice Plate	Orifice Dia (in)	Mainstream			Fore Dilution Jet					Aft Dilution Jet					Regions of Measurement			
			Mass Flow Rate (kg/s)	Temp (°K)	Velocity (Main) (m/s)	Mass Flow Rate (kg/s)	Momentum Flux Ratio $\frac{V_j F}{j_F}$	Temp (°K)	Velocity (m/s)	Flux Ratio $\frac{V_j F}{j_F}$	(C <sub>D</sub> ) <sub>F</sub>	Mass Flow Rate (kg/s)	Momentum Flux Ratio $\frac{V_j F}{j_A}$	Temp (°K)	Velocity (m/s)	(C <sub>D</sub> ) <sub>A</sub>	Equilibrium Dislocation (THEB)	Axial Dislocation X/H <sub>0</sub>	Transverse Dislocation Z/S
13	M-5	1.80	0.5	0.2657	672.0	17.0	0.06769	26.20	310.1	58.5	0.683	0.03663	6.36	310.9	29.1	0.756	0.2821	0.25 - 2.0	-0.5 to +0.5
14	M-5	1.27	0.25																
		1.80	0.5	0.2650	666.3	16.8	0.1338	106.5	304.5	113.0	0.650	0.03662	6.48	312.5	29.2	0.756	0.3938	0.25 - 2.0	-0.5 to +0.5
15	M-5	1.27	0.25																
		1.80	0.5	0.2655	660.0	16.7	0.1329	106.3	305.8	112.9	0.650	0.06941	26.37	302.3	57.6	0.700	0.4318	0.25 - 2.0	-0.5 to +0.5
16	M-6	1.27	0.25																
		1.80	0.5	0.2670	656.6	16.7	0.1401	106.8	306.7	114.4	0.685	0.03726	6.46	290.6	28.2	0.744	0.3939	0.25 - 2.0	-0.5 to +0.5
17	M-6	1.27	0.25																
		1.80	0.5	0.2671	663.8	16.9	0.1414	106.8	305.1	114.8	0.685	0.07057	26.49	297.3	57.9	0.695	0.4409	0.25 - 2.0	-0.5 to +0.5
18	M-7	2.54	0.5	0.2666	684.2	17.4	0.07156	6.64	316.3	30.4	0.719	-	-	-	-	-	0.2116	0.25 - 2.0	-0.5 to +0.5
		1.80	0.5	0.2672	675.5	17.2	0.1338	27.13	314.5	60.5	0.662	-	-	-	-	-	0.3336	0.25 - 2.0	-0.5 to +0.5
19	M-7	2.54	0.5	0.2672	675.5	17.2	0.1338	27.13	314.5	60.5	0.662	-	-	-	-	-	0.3336	0.25 - 2.0	-0.5 to +0.5
		1.80	0.5	0.2672	675.5	17.2	0.1338	27.13	314.5	60.5	0.662	-	-	-	-	-	0.3336	0.25 - 2.0	-0.5 to +0.5
20	M-7	2.54	0.5	0.2672	675.5	17.2	0.1338	27.13	314.5	60.5	0.662	-	-	-	-	-	0.3336	0.25 - 2.0	-0.5 to +0.5
		1.80	0.5	0.2672	675.5	17.2	0.1338	27.13	314.5	60.5	0.662	-	-	-	-	-	0.3336	0.25 - 2.0	-0.5 to +0.5
21	A	2.54	0.5	0.2574	629.1	15.3	0.2929	103.2	307.0	104.3	0.764	-	-	-	-	-	0.5322	0.25 - 2.0	-0.5 to +0.5
		1.80	0.5	0.2574	629.1	15.3	0.2929	103.2	307.0	104.3	0.764	-	-	-	-	-	0.5322	0.25 - 2.0	-0.5 to +0.5
22	A	2.54	0.5	0.2663	668.5	16.9	0.1515	26.24	312.7	58.6	0.765	-	-	-	-	-	0.3626	0.25 - 2.0	-0.5 to +0.5
		1.80	0.5	0.2663	668.5	16.9	0.1515	26.24	312.7	58.6	0.765	-	-	-	-	-	0.3626	0.25 - 2.0	-0.5 to +0.5

$X/H_0 = 1$ , the temperature fields for Test No. 13 and Test No. 12 are very similar. This implies that the leading row dominates the temperature field development, and that the increasing mass flows through the downstream row of holes does not make appreciable difference in the far field temperature distributions.

The predicted temperature distributions for Test No. 13 are shown in Figure 33. At  $X/H_0 = 0.25$  and  $0.5$ , the predicted centerplane profiles show poor agreement with the data. But, at the downstream stations, the two profiles are in very good agreement. These results demonstrate the validity of the superposition scheme, even for unbalanced momentum flux ratios.

Figure 34 provides the measured temperature distributions for Test No. 14, using orifice plate M-5, with  $J = 106.5$  for the lead row and  $J = 6.48$  for the trailing row of jets. The discharge coefficients for the two rows are  $0.650$  and  $0.756$ , respectively, in this test case. The equilibrium theta value for Test No. 14 is  $0.3998$ . At  $X/H_0 = 0.25$ , the leading row of jets overpenetrate to the bottom wall of the test section, while the trailing jet penetration is suppressed at 10 percent of the duct height. At the downstream stations, the mixing is dominated by the lead row of jets and produce completely mixed temperature distributions beyond  $X/H_0 = 1.0$ . These profiles are similar to those obtained in Test No. 12 (Figure 30) in which both rows of jets had high-momentum flux ratios.

The predicted temperature distributions for Test No. 14 are shown in Figure 35. At  $X/H_0 = 0.25$  and  $0.5$ , the empirical model predicts suppression of jet penetrations for the lead row, while the data does not show such characteristics. Consequently, at those stations, the predictions are in poor agreement with the data. However, beyond  $X/H_0 = 1.0$ , the model predictions correlate well with the data. In the regions between  $X/H_0 = 0.25$  and  $0.5$ , the data show non-Gaussian profiles, where the empirical model is not expected to be accurate.

Figure 36 illustrates the measured temperature distributions for Test No. 15, using orifice Plate M-5 with  $J = 106.3$  for the lead row and  $J = 26.37$  for the trailing row. The discharge coefficients for these two rows are 0.685 and 0.695, respectively. These temperature profiles are very similar to those obtained in Test No. 14 (Figure 34). Thus, the addition of mass flow in the downstream row has influenced only the near field ( $X/H_0 \leq 0.5$ ) temperature distributions.

The predicted results for Test No. 15 are presented in Figure 37. In the regions  $X/H_0 \leq 0.5$ , the data show non-Gaussian profiles, and hence the empirical model does not correlate well with the data. At the downstream stations, the predicted temperature field is within first order accuracy.

The last three test cases have demonstrated that the leading row of jets clearly dominate the jet mixing characteristics. In these test cases, the leading row also contains the larger diameter jets. At constant momentum flux ratio, the larger diameter holes will dominate the mixing characteristics. In order to delineate the effects of hole diameter and the axial staging, the following two test cases were performed by reversing the order of the dissimilar rows of jets in Plate M-5. This orifice plate is designated as M-6. In orifice Plate M-6, the lead row has 12 circular holes with  $D = 1.27$  cm,  $S/D = 2$  and  $H_0/D = 8$ , while the trailing row contains 6 circular holes with  $D = 1.83$  cm,  $S/D = 2.83$  and  $H_0/D = 5.66$ . The two test cases performed using orifice Plate M-6 had unbalanced momentum flux ratios.

Test No. 16 was performed using orifice Plate M-6, with  $J = 106.8$  for the leading row and  $J = 6.46$  for the larger trailing row of jets. The equilibrium theta values for this test case was 0.3939. The measured temperature distributions for Test No. 16 are presented in Figure 38. At  $X/H_0 = 0.25$ , the leading row of jets with  $J = 106.8$  penetrate to the middle of the duct, while



the trailing jets with  $J = 6.46$  penetrate to about 30 percent of the duct height. These penetrations were also obtained for the corresponding single row of jets based upon Phase I and Phase II test data. This implies little suppression of jet penetration at this location. However, at the downstream stations, the center-plane penetration of the trailing row of jets is suppressed by the vortex field produced by the lead row of jets. The temperature distributions beyond  $X/H_0 = 0.5$  are very similar to those produced by orifice Plate 01/02/08 (Figure 22, Reference 6). These profiles are quite different from those shown for Plate M-5 (Figure 34) for comparable mass and momentum flux ratios. Thus, the mixing characteristics in Test No. 16 are dominated by the leading row of jets, even though they have smaller diameters.

The temperature distributions calculated from the empirical model for Test No. 16 are shown in Figure 39. In the empirical model, the temperature distributions are obtained by super-imposing the temperature field due to each individual row of jets at the appropriate momentum flux ratio and transverse plane. As observed in the earlier tests cases, the superposition scheme correctly predicts the jet penetrations in regions close to the injection plane. However, beyond  $X/H = 0.5$ , the empirical model predicts the temperature field within first order accuracy.

Test No. 17 was performed using orifice Plate M-6 with  $J = 106.8$  for the lead row of jets and  $J = 26.49$  for the trailing row. Note that the momentum flux ratios of the lead and the trailing rows are optimum for each of the two individual rows. The discharge coefficients for these two rows in this test case were, 0.685 and 0.695, respectively. The measured theta distributions for this case are shown in Figure 40. These distributions are very similar to those observed in Test No. 16 (Figure 38). In the case where the leading and trailing rows are reversed (Test NO. 15), the measured temperature profiles (Figure 36) were significantly different. This test case, once again,

demonstrates the dominance of the lead row regardless of the jet diameters.

The empirical model predictions for Test No. 17 are shown in Figure 41. In this test case, the suppression of jet penetration is not significant since both leading and trailing rows of jets penetrate to the middle of the duct. The centerplane profiles shown in Figures 39 and 41 correspond to the centerplanes of the larger, downstream holes. This was done primarily to compare with the results for Plate M-5. The empirical model slightly underestimates the peak theta values at  $X/H_0 = 0.25$ , but gives first order agreement with the data at the downstream stations. The empirical model also predicts the dominance of the lead row of jets regardless of the size of the jets.

The following three test cases were performed using 45-degree slanted slots, Plate M-7 (see Figure 4). The tests performed with streamlined and bluff slots showed temperature distributions that are very similar to those of equivalent circular holes. The vortex pair generated by the streamlined and bluff slots are symmetric with respect to the mainstream direction. In the case of angled slots, the vortex pair need not be symmetric. Furthermore, the angled slots could produce characteristics very similar to axially-staged offset jet arrangement, when the axial separation distance is small. Considering all these aspects, it was decided to investigate the mixing characteristics of the 45-degree slots as a part of the Series 10 test program.

The 45-degree slots have the same geometric area as the streamlined or bluff slots with the ratio of total jet area to mainstream area of 0.098. For the 45-degree slot, the streamwise length and the frontal width are equal, hence, the aspect ratio is 1.0.

Test No. 18 was performed using orifice Plate M-7 (45-degree slot) with  $J = 6.64$ . The equilibrium theta value for this test case was 0.2116. The measured temperature field for this test case is presented in Figure 42. The data clearly shows that for the 45-degree slot, the centerplane location also shifts in the transverse direction. The theta contours also show rotation about the slot centerline, as is evident in the rotated kidney-shaped theta isopleths. This rotation suggests that the vortex closer to the upper wall (which originated from the trailing edge of the 45-degree slot) is stronger than the lower vortex. These characteristics are dominant only at  $X/H_0 = 0.25$  and  $0.5$ . Beyond that station, the temperature field for 45-degree slot is very similar to those of streamlined slots at the low-momentum flux ratio.

The temperature distributions calculated from the empirical model for Test No. 18 are presented in Figure 43. The empirical model accounts for the centerplane shift with downstream distance, but, it does not account for the rotation of the theta contours caused by the differences in the strengths of the vortex pair associated with each slot. The centerplane shift is a function of the slot angle, momentum flux ratio, and the downstream distance. The empirical correlation was modified to account for these effects. Details of these modifications are provided in Section 6.1. The predicted centerplane temperature profiles and the jet penetrations are in good agreement with the data. The empirical model slightly underestimates the transverse mixing rate.

Figure 44 shows the measured temperature distributions for Test No. 19 using orifice Plate M-7 (45-degree slot) with  $J = 27.13$ . The equilibrium theta value for this test case was 0.3336. For this test case, the centerplane shift is faster than that at lower-momentum flux ratio. This illustrates the effect of a momentum flux ratio on the lateral shift. However, the

amount of rotation of the contours is nearly the same. This rotation is primarily due to the differential vortex strength originating from the leading and trailing edges, which is a function only of the slot length and the angle. The jet penetration and mixing rates at this momentum flux ratio are less than those of streamlined or bluff slots. This suggests that there is no inherent advantage in using this orifice configuration.

The temperature distributions obtained from the empirical model for Test No. 19 are presented in Figure 45. The empirical model correctly predicts the jet penetration and the centerplane shift. The model, however, overestimates the mixing in the transverse direction and underestimates the mixing in the vertical direction. The overall accuracy of the model is within engineering needs.

Figure 46 presents the measured temperature field for Test No. 20, using orifice Plate M-7 with  $J = 106.18$ . The equilibrium theta value for this case was 0.4865. At the first measurement station ( $X/H_0 = 0.25$ ), the centerplane shifts very close to the midplane. Because of the presence of the test section end walls, and the cyclic symmetry requirements, the centerplanes cannot shift past the midplane. The jet penetration in this case is significantly less than that for bluff slots or equivalent area circular holes (Figures 14 and 48). The mixing in the transverse direction with 45-degree slots is slower than other equivalent dilution jet configurations.

The temperature field calculated from the empirical model for Test No. 20 is shown in Figure 47. Although the empirical model correctly predicts the centerplane shift, the jet penetration and mixing in the transverse direction are overestimated. The jet mixing in the vertical direction is underpredicted by the model. The overall agreement between the data and model predictions for this case is poor.

The last three test cases demonstrate that the performance of the 45-degree slot is inferior to the equivalent circular holes, streamlined, or bluff slots. The 45-degree slot can be considered equivalent to closely spaced, axially-staged rows of jets, with a small lateral offset. Thus, the data for 45-degree slots and other double row configurations studied in this Phase, show that when the axial separation between rows is too small, the mixing is inhibited due to the asymmetry in the vortex strengths generated by each jet.

At the end of Series 9 test, it was recognized that it would be beneficial to obtain data for orifice plate 01/02/04 (Plate A) at moderate and high-momentum flux ratios to provide a baseline comparison for the discrete and continuous slots with a comparable geometric area. The last two tests in this program area were made using orifice plate 01/02/04 (Plate A) with orifice diameter of 2.54 cm,  $S/D = 2.0$  and  $H_0/D = 4.0$ .

Test No. 21 was performed using Plate A with  $J = 103.2$ . The equilibrium theta value in this test was 0.5322. The measured temperature distributions for Test No. 21 are presented in Figure 48. At  $X/H_0 = 0.25$ , the jets penetrate to about 80 percent of the duct height. At  $X/H_0 = 0.5$ , they penetrate to the bottom wall followed by rapid mixing in the transverse direction. Because of the overpenetration of jets, the entrainment of the mainstream is slower near the injection wall (top wall) than near the jet centerline. Consequently, the temperatures in the wake region of the jets are higher (lower theta value) than near the bottom wall. At  $X/H_0 = 2.0$ , the theta values approach equilibrium theta.

The empirical model predictions for Test No. 21 are presented in Figure 49. The model accurately predicts the jet penetration and the transverse mixing, but slightly underestimates

the mixing in the vertical direction. The overall correlation between the data and the empirical model predictions is good.

As pointed out earlier, the circular holes have very similar mixing characteristics as the bluff slots at the high-momentum flux ratios. The mixing rates with these orifices are faster than those with 45-degree slots. The circular jets in Test No. 20 also have characteristics similar to those observed with double rows of jets (Figures 20 and 30).

While evaluating the Phase I and Phase II tests, it was discovered that the values of the momentum flux ratios quoted for some of these tests are incorrect. In particular, the momentum flux ratio for Test No. 2 in Phase I, using Plate A was 18.5 instead of 21.6 as reported. The correct values of momentum flux ratios for all these test cases are provided in Appendix A. Since several of the tests conducted in this program were compared with the data for orifice plate 01/02/04 at  $J = 26.4$  it was deemed essential to obtain accurate data at this test condition. Test No. 22 was performed to collect data at this condition.

Figure 50 provides the measured temperature distributions for Test No. 22, using orifice plate A at  $J = 26.24$ . The equilibrium theta value for this test case was 0.3626. This means that the ratio of jet to total mass flow rate was 0.3626. At  $X/H_0 = 0.25$ , the jet penetration is about 60 percent of the duct height. At the downstream stations, the jets penetrate deeper and reach the bottom wall of the duct at  $X/H_0 = 1.0$ . Beyond that point, the mixing is enhanced in the transverse direction and the jets are in fully mixed conditions at  $X/H_0 = 2.0$ . The jet penetration and mixing characteristics of Plate A are similar to those of streamlined or bluff slots, and other equivalent double row of jets.

Figure 51 shows the empirical model results for Test No. 22. The empirical model slightly underestimates the jet penetration and the mixing in the vertical direction. Both model prediction and data show fully mixed distributions at  $X/H_0 = 2.0$ . The overall accuracy of model predictions is good.

#### 5.2.1 Test Series 10 Conclusions

All the tests in Series 10 were performed in a constant area duct with an isothermal mainstream. A total of 10 tests were performed in this test series. The first 5 tests were performed using double row of dissimilar orifices with mis-matched momentum flux ratios. The next 3 tests were made using 45-degree slots and the final 2 tests were performed to increase the data base on single row of jets (orifice plate 01/02/04). The NASA/Garrett correlations were used to obtain predictions for all these test cases. The following conclusions were made from these efforts:

- o The jet penetrations and mixing characteristics are dominated by the lead row of jets. The size of the trailing row of jets have little influence on the temperature field beyond  $X/H_0 = 0.5$ .
- o The temperature field with orifice plate M-5 ( $S/D = 2.83$ ,  $H_0/D = 5.66$  in the lead row) is very similar to those obtained from single row of equivalent area jets with  $S/H_0 = 0.5$ .
- o The temperature field with orifice plate M-6 ( $S/D = 2.0$ ,  $H_0/D = 8.0$  in the lead row) is very similar to those obtained from orifice plate 01/02/08 ( $S/D = 2$ ,  $H_0/D = 8$ ) at comparable momentum flux ratio.
- o The jet penetration and mixing rates for 45-degree slots are lower than those of streamlined or bluff

slots, or equivalent area single row of circular holes. The 45-degree slot can be considered equivalent to closely spaced axially-staged row of jets with a small lateral offset. Thus, the jet penetrations with offset double row of holes are reduced when axial spacing between the rows are reduced.

- o The skewed vortex field generated by the 45-degree slots shifts the jet centerplanes in the direction of the slot and also rotates the temperature contours.
- o The NASA/Garrett empirical model accurately predicted the temperature fields in cases with mis-matched momentum flux ratios. This supports the validity of the superposition scheme adopted in the model.
- o The empirical model accurately predicts the lateral shift of centerplanes for 45-degree slots, but does not account for the rotation of the theta contours. Additional model improvements are needed to account for these effects. Despite these differences, the empirical model is a useful, first order accurate design tool.



## 6.0 JET MIXING CORRELATION DEVELOPMENT

The design of the dilution zone in gas turbine combustors forms only a part of the overall combustion system development. The combustor designer has to ensure the performance and durability of the combustor prior to designing or redesigning the dilution zone. As a result of this, the combustor designer often encounters a situation where, most of the development time is spent on meeting the performance and durability of the system and very little development time is available for dilution zone design. Yet, the dilution zone has a major impact on the durability and performance of the turbine section. To meet the turbine inlet profile quality requirements, the only recourse available to the designer is to modify the dilution zone configuration without impacting the combustor primary zone performance. For such circumstances, it is desirable to have empirical models for characterizing the combustor exit temperature profile quality, as functions of dilution zone geometric and flow parameters.

Motivated by these requirements, empirical models have been developed (References 3, 4, 6, and 7) for applications to combustor dilution zones. These models are limited within the geometrical and flow parameters of the generating experiments and must be used with caution outside the range of their applicability. Among these models, the correlations developed by Holdeman, et al (Reference 4) are useful and powerful tool for designing the dilution zone of practical combustors. The correlations obtained in Reference 4 were applicable to a single-sided row of jets injected into a confined cross flow. These correlations have been used to identify and optimize the major geometrical and flow parameters for single-sided injection of jets into a confined cross flow. A review of the measured effects of momentum flux ratio, mainstream temperature profile, flow area convergence, and configurations of opposed jet injections are provided in Reference 6.

These correlations were extended to the two-sided row of jets injected into a confined cross flow, in Reference 7. These extensions have provided a valuable design methodology applicable to practical combustion systems. These correlations are applicable only to single row of circular jets. However, many practical gas turbine combustion systems employ multiple rows of dilution jets, and non-circular orifices. The empirical correlations available in the literature cannot predict the mixing characteristics of such dilution zone configurations.

The effects of orifice shapes, axial staging, and other complexities can be treated through the use of multi-dimensional Navier-Stokes solutions. Such techniques (References 11, 12) are rapidly improving in accuracy and efficiency due to advances in computational fluid dynamics. These models are in a developmental stage and need extensive validation efforts. The multi-dimensional models are time consuming and are not cost-effective for the combustor designer at present.

In the present program, a data base was generated for multiple rows of jets and for a row of non-circular jets injected into a confined cross flow. Preliminary investigation of the data for multiple rows of jets indicated that superposition of the temperature field, due to each individual row of jets, could predict the temperature field due to multiple rows. This approach was adopted in developing correlations for multiple rows. The empirical relations for non-circular jets were obtained by further modifying the NASA/Garrett correlations developed in Reference 7. The correlations developed in Phase III efforts are described in Paragraph 6.1.

## 6.1 NASA/Garrett Correlations for Mixing Multiple Rows and Non-Circular Jets in a Confined Cross Flow

The correlations developed in this phase use the same nomenclatures as those employed in Reference 7. These empirical expressions are applicable to axially-staged injections or to a row of non-circular jets. Paragraph 6.1.1 describes the empirical model for predicting mixing characteristics of multiple rows of jets. Paragraph 6.1.2 provides a description of the model for non-circular row of jets injected into a confined cross flow. In these correlations, the subscript "F" refers to the front row of jets and the subscript "A" refers to the aft row of jets.

### 6.1.1 Empirical Model for Mixing of Double Row of Dilution Jets in a Confined Cross Flow

The parameter used to describe the temperature distribution is the nondimensional temperature difference, theta ( $\theta$ ), defined as

$$\theta = \frac{T_m - T}{T_m - T_j} \quad (1)$$

where:

- $\theta$  = Theta, nondimensional temperature difference at a point in the flow field
- $T_m$  = Mainstream stagnation temperature
- $T_j$  = jet stagnation temperature
- $T$  = stagnation temperature at a point in the flow field

Theta is a measure of the temperature suppression in the flow field. The value of theta can vary from one, when measured temperature equals the jet temperature, to zero, when the measured temperature equals the main stream temperature. The largest values of theta in any profile correspond to the coolest regions of the flow.

If complete mixing of the jet and mainstream flow occurs, the value of theta will be constant and the temperature will be everywhere equal to the ideal equilibrium temperature between jet and mainstream. Thus,

$$\theta_{EB} = \frac{T_m - T_{EB}}{T_m - T_j} \quad (2)$$

where:

$\theta_{EB}$  is the ideal equilibrium theta.

$$T_{EB} = \frac{\dot{m}_{j_F} T_{j_F} + \dot{m}_{j_A} T_{j_A} + \dot{m}_m T_m}{\dot{m}_{j_F} + \dot{m}_{j_A} + \dot{m}_m} \quad (3)$$

$$\text{Let } \theta_F = \frac{T_m - T_F}{T_m - \bar{T}_j}, \quad \theta_A = \frac{T_m - T_A}{T_m - \bar{T}_j} \quad (4)$$

where  $T_F$  and  $T_A$  are the local temperature due to front or aft injections only.

Assumption: Let  $T$  be the actual local temperature due to both front and aft injections.

Then,

$$\theta = \frac{T_m - T}{T_m - \bar{T}_j} = \left( \frac{\frac{1}{2} \dot{m}_m + \dot{m}_{j_F}}{\dot{m}_m + \dot{m}_{j_F} + \dot{m}_{j_A}} \right) \theta_F + \left( \frac{\frac{1}{2} \dot{m}_m + \dot{m}_{j_A}}{\dot{m}_m + \dot{m}_{j_F} + \dot{m}_{j_A}} \right) \theta_A \quad (5)$$

In this equation,  $\theta_F$  and  $\theta_A$  are obtained from the empirical model by using appropriate equilibrium temperatures. For the front and the aft jets,  $T_{EB}$  is obtained from

$$(T_{EB})_F = \left( \frac{\frac{1}{2} \dot{m}_m T_m + \dot{m}_{j_F} T_{j_F}}{\frac{1}{2} \dot{m}_m + \dot{m}_{j_F}} \right) \quad (6)$$

$$(T_{EB})_A = \left( \frac{\frac{1}{2} \dot{m}_m T_m + \dot{m}_{j_A} T_{j_A}}{\frac{1}{2} \dot{m}_m + \dot{m}_{j_A}} \right) \quad (7)$$

The empirical model for the three-dimensional flow is expressed in nondimensionalized self-similar form as:

$$\theta = \theta_{\min}^{\pm} + (\theta_c - \theta_{\min}^{\pm}) \exp \left[ \left( -\ln 2 \right) \left( \frac{y - y_c}{w_{1/2}^{\pm}} \right)^2 \right] \quad (8)$$

This expression is applicable to both front and aft injections. In this equation,  $\theta_c$ ,  $\theta_{\min}^{\pm}$ ,  $y_c$ , and  $w_{1/2}^{\pm}$  are scaling parameters as shown in Figure 52.  $\theta_c$  is the maximum temperature difference ratio in the radial (vertical) profile, and  $y_c$  represents the position of minimum temperature (or maximum theta). Here,  $\theta_{\min}^{+}$  and  $\theta_{\min}^{-}$  are the minimum dimensionless temperature difference beyond and before the jet centerline, respectively.

The correlations describe the scaling parameters as functions of independent variables  $J$ ,  $S/D$ ,  $H_{eq}/D$ ,  $X/H_{eq}$ , and  $Z/S$ . The scaling parameters are nondimensionalized by using the effective jet diameter,  $D_j = D \sqrt{C_d}$ . Here,  $H_{eq}$  is the equivalent duct height at the jet injection plane. For double row of jets, the jet injection plane is the plane midway between the two rows.

### Correlations for Predicting Centerplane Temperature Profiles:

#### (A) Jet Centerline Trajectory

$$\left(\frac{Y_{c,o}}{D_j}\right) = \alpha_1 J^{0.25} \left(\frac{S}{D_j}\right)^{0.14} \left(\frac{H_{eq}}{D_j}\right)^{0.38} \left(\frac{X}{D_j}\right)^{0.17} e^{-b} \quad (9)$$

where,

$$b = 0.091 \left(\frac{X}{H_{eq}}\right)^2 \left(\frac{H_{eq}}{S} - \frac{\sqrt{J}}{3.5}\right)$$

$$\alpha_1 = \text{Min} \left[ 0.3575 \left(1 + \frac{S}{H_{eq}}\right), 0.715 \right]$$

#### (B) Centerline Temperature Difference Ratio:

$$\theta_{c,o} = \theta_{EB} + (1 - \theta_{EB}) \left[ \alpha_2 J^{-0.35} \left(\frac{X}{D_j}\right)^{-1} \right]^f \quad (10)$$

where,

$$f = 1.15 \sqrt{\frac{S}{H_{eq}}} / \left(1 + \frac{S}{H_{eq}}\right) \quad (11)$$

$$\alpha_2 = 1 + S/H_{eq}$$

$$\text{Here, } \theta_{EB} = \left(\frac{T_m - T_{EB}}{T_m - T_j}\right) ; T_{EB} = \left[ \frac{\dot{m}_m T_m + \dot{m}_{j_F} T_{j_F} + \dot{m}_{j_A} T_{j_A}}{\dot{m}_m + \dot{m}_{j_F} + \dot{m}_{j_A}} \right] \quad (12)$$

(C) Centerplane Half Width

$$\frac{W_{1/2}^+}{D_j} = 0.1623 \left( \frac{S}{D_j} \right)^{-0.25} \left( \frac{H_0}{D_j} \right)^{0.5} \left( \frac{X}{D_j} \right)^{0.5} J^{0.18} \quad (13)$$

$$\frac{W_{1/2}^-}{D_j} = 0.20 \left( \frac{S}{D_j} \right)^{0.27} \left( \frac{H_0}{D_j} \right)^{0.5} \left( \frac{X}{D_j} \right)^{0.12} J^{0.15} \quad (14)$$

Note  $W_{1/2}$  is doubled for opposed in-line injections.

(D) Minimum Centerplane Temperature Difference Ratio

$$\frac{\theta_{\min}^+}{\theta_{c,o}} = 1 - e^{-c^+} \quad (15)$$

where,

$$c^+ = \alpha_3 J^{1.62} \left( \frac{S}{D_j} \right)^{1.5} \left( \frac{X}{D_j} \right)^{1.1} \left( \frac{H_{eq}}{D_j} \right)^{-3.67} \quad (16)$$

$$\alpha_3 = 0.038 \quad \text{if} \quad \left( \frac{Y_{c,o}}{D_j} + \frac{W_{1/2}^+}{D_j} \right) \leq \frac{H_{eq}}{D_j} \quad (17)$$

$$\alpha_3 = 0.038 \left( \frac{H_0}{H_{eq}} \right)^{3.67} \quad \text{if} \quad \left( \frac{Y_{c,o}}{D_j} + \frac{W_{1/2}^+}{D_j} \right) > \frac{H_{eq}}{D_j}$$

The above modification ensures that when the jets penetrate close to  $H_{eq}$ , the Gaussian curve for the positive part of the theta profile (Figure 52) approaches a nearly flat profile. Furthermore, when the jets penetrate close to  $H_{eq}$ , the test data shows that the value of  $\theta_{\min}^-$  also approaches the value of  $\theta_{c,o}$ . This characteristic is modeled by the following expression:

$$\frac{\theta_{\min}^-}{\theta_{c,o}} = 1 - e^{-c^-} \quad (18)$$

where,

$$c^- = c_o \quad \text{if} \quad \left( \frac{y_{c,o}}{D_j} + \frac{w_{1/2}^+}{D_j} \right) \leq \frac{H_{eq}}{D_j} \quad (19)$$

$$c^- = c_o Q \quad \text{if} \quad \left( \frac{y_{c,o}}{D_j} + \frac{w_{1/2}^+}{D_j} \right) > \frac{H_{eq}}{D_j}$$

$$c_o = 1.57 J^{-0.3} \left( \frac{S}{D_j} \right)^{-1.4} \left( \frac{X}{D_j} \right)^{0.9} \quad (20)$$

$$Q = \exp \left[ 0.22 \left( \frac{X}{H_{eq}} \right)^2 \left( \frac{\sqrt{J}}{5} - \frac{S}{H_{eq}} \right) \right]$$

(E) Off-Centerplane Penetration

$$\frac{y_{c,z}}{y_{c,o}} = 1 - \left( \frac{z}{S/2} \right)^2 e^{-g} \quad (21)$$

where,

$$g = \alpha_4 J^{0.67} \left( \frac{S}{D_j} \right)^{-1} \left( \frac{X}{D_j} \right)^{0.54} \quad (22)$$

$$\alpha_4 = 0.227$$

(F) Off-Centerplane Maximum Temperature Difference Ratio

$$\frac{\theta_{c,z}}{\theta_{c,o}} = 1 - \left( \frac{z}{S/2} \right)^2 e^{-d} \quad (23)$$

where,

$$d = \alpha_5 J^{0.53} \left( \frac{S}{D_j} \right)^{-1.53} \left( \frac{X}{D_j} \right)^{0.83} \quad (24)$$

$$\alpha_5 = 0.452$$



$$\text{Furthermore, } \frac{\theta_{\min,Z}^{\pm}}{\theta_{c,Z}} = \frac{\theta_{\min,o}^{\pm}}{\theta_{c,o}} \quad (25)$$

For obtaining  $\theta_F$  or  $\theta_A$  in equation (5), the appropriate values of  $J_F$  or  $J_A$  are used in the equations (9) through (24). From these values of  $\theta_F$  and  $\theta_A$  the actual non-dimensional temperature field due to the double row of jets can be obtained from Equation 5. This approach was used in predicting the temperature fields presented earlier in this report.

#### 6.1.2 Empirical Model For Mixing of a Row of Non-Circular Jets in a Confined Cross Flow

One of the orifice configurations frequently employed in gas turbine combustion systems is discrete slots. These slots can be streamlined, bluff, or angled with respect to the cross flow. An important parameter characterizing such slots is the aspect ratio, AR, which is defined as the ratio of frontal width to streamwise length of the slot. In this phase of the program, the aspect ratios of the streamlined and bluff slots used were 0.355 and 2.818, respectively. For the 45-degree-angled slots, the frontal width and the streamwise length were equal, giving AR = 1.0. By the same logic, the aspect ratio for circular holes is 1.0.

A preliminary review of the test data for discrete slots indicated that when compared with equivalent area circular holes, the jet penetration was deeper for streamlined slots, and less for bluff slots. Another parameter that was influenced by the orifice shape was the peak centerplane theta value. The rest of the scaling parameters used to define the non-dimensionalized temperature field are not significantly influenced by the orifice shape. Based upon these observations, the empirical model described in paragraph 6.1.1 was modified only to change the jet penetration (equation 9) and the centerplane temperature differ-

ence ratio (equation 10). The influence of orifice shape was achieved by changing the empirical constants  $\alpha_1$  and  $\alpha_2$  by the following expressions.

$$\alpha_1 = \text{MIN} \left[ 0.3575 \left( 1 + \frac{S}{H_{eq}} \right), 0.715 \right] / (AR)^{0.5} \quad (26)$$

and

$$\alpha_2 = \left( 1 + \frac{S}{H_{eq}} \right) (AR) \quad (27)$$

These modifications have been adequate for describing the temperature distributions for streamlined slots. For bluff slots, these changes were adequate for predicting only the centerplane temperature profiles. The empirical model requires major modifications for predicting the distributions in the transverse direction. Simple modifications of the existing expressions were not sufficient to characterize the temperature field. Development of new correlations for this orifice geometry was deemed beyond the scope of the program.

For angled slots, the test data shows that the jet centerplane at downstream stations, shift along the direction of the slot centerline. This shift cannot be larger than half the orifice spacing due to the presence of end walls and symmetry considerations. The centerplane shift is a function of momentum flux ratio and the downstream distance. The centerplane shift,  $\Delta Z$ , has been correlated by the following equation:

$$\frac{\Delta Z}{S} = \text{Sin} (\pi \alpha) / s \quad (28)$$

where,

$$\alpha = \text{Min} (0.5, \beta) \quad (29)$$

$$\beta = 0.5 \left( \frac{X}{H_{eq}} \right) \left( \frac{J}{26.4} \right)^{0.25} \quad (30)$$

and  $S$  is the orifice spacing.

From the known centerplane shift, the theta distributions are obtained by shifting the distributions obtained from the NASA/Garrett correlations (Equation 8) by the same amount. This is illustrated in the sketch in Figure 53.

This procedure describes, within first order accuracy, the temperature field for angled slots. The test data for angled slots also indicate a rotation of the theta contours. This rotation is caused by the differences in the strengths of the staggered pair of vortices originating from the leading and the trailing edges of the slots. This interaction is difficult to analyze, and developing correlations to describe this interaction is beyond the scope of this program.



## 7.0 CONCLUSIONS AND RECOMMENDATIONS

Phase III of the NASA Dilution Jet Mixing Program was directed towards understanding and characterizing the mixing processes with double row of circular jets and single row of non-circular jets. The tests performed in Phase III program provide a valuable data base for developing and validating analytical models. Based upon these test data, empirical models have been developed to predict the temperature fields due to double row of circular jets and single row of non-circular jets, when injected into a confined heated cross flow. The following conclusions are drawn from these tests:

- o The jet penetrations of streamlined slots are slightly deeper than the equivalent circular jets in the region near the injection plane ( $X/H_0 < 1$ ). At the downstream stations, the temperature field for streamlined slots are very similar to those of equivalent circular holes at constant momentum flux ratio. Equivalent circular holes have the same geometric area and  $S/H_0$  value as the slots.
- o The jet penetrations for bluff slots are slightly less than the equivalent circular holes or streamlined slots. For  $X/H_0 < 1$ , the bluff slots produce more two-dimensional temperature field than streamlined slots. At downstream locations, streamlined and bluff slot configurations and equivalent circular holes produce very similar temperature distributions.
- o The temperature distribution for a double row of in-line jets is very similar to those of single row of jets with the same  $S/H_0$  and geometric area. The development of the temperature profile shape is dominated by the lead row. But, the interactions of the vortices

generated by the two rows of jets, tend to suppress the jet penetrations in the lead row.

- o For double row of staggered jets, the lead row has a dominant influence on the temperature profile development. In this case, the jet penetrations in the trailing row is suppressed by the vortex field generated by the lead row. These effects are predominant in the near field ( $X/H_0 < 1$ ). At the downstream stations, the temperature fields produced by double row of staggered jets are similar to those of double row of in-line jets.
- o For double row of dissimilar jets (Plates M-5 and M-6), the lead row has a dominant influence on the temperature profile development. In this case, at constant momentum flux ratio, the jet penetrations of the leading and trailing rows are different. This creates a vortex field which tends to enhance mixing in the vertical direction. These characteristics are significant only in the regions near the jet injection plane ( $X/H_0 < 1$ ). Since the temperature distributions are dominated by the lead row of jets, if the lead row has  $S/H_0$  value of 0.5 (Plate M-5), the temperature field is similar to equivalent single row of holes with  $S/H_0 = 0.5$  at the same momentum flux ratio. If the lead row has  $S/H_0$  value of 0.25 (Plate M-6), the temperature distributions are similar to those with single row of jets with  $S/H_0 = 0.25$  at the same momentum flux ratio.
- o The jet penetration and mixing rates for 45-degree slots are lower than those of equivalent area circular holes, streamlined, or bluff slots. The 45-degree slots can be viewed as off-set double row of holes with very small axial spacing between the rows.

- o The 45-degree slots generate a skewed vortex field, which shifts the jet centerplanes in the direction of the slot. In addition, the vortex field rotates the temperature contours about the axis of the slot.
- o The NASA/Garrett empirical model (Reference 7) was modified to include the effects of aspect ratio of discrete slots for predicting the mixing characteristics. The modified model predicts the temperature field due to streamlined slots within first order accuracy. For bluff slots, this empirical model gives an inferior agreement with the data. Additional work is needed to improve the empirical model predictions.
- o The empirical model predictions for double row of jets are obtained by superimposing the temperature field due to each individual row of jets. This superposition scheme gives good correlations with the data, especially in the regions beyond  $X/H_0 = 0.5$ . In the regions closer to the jet injection plane, the data shows non-Gaussian profiles, which are not predicted by the empirical model when the jet penetrations of each row are comparable.
- o The empirical model accurately predicts the lateral shift of centerplanes for 45-degree slots, but does not account for the rotation of the temperature contours.
- o The modified empirical model provides a very valuable, first order tool for designing gas turbine combustor dilution zones. This model can be applied to single-sided or two sided jets, single or double rows of jets, as well as circular and non-circular orifice configurations. They are applicable over a wide range of geometric and flow conditions observed in gas turbine combustion systems.





## REFERENCES

1. Walker, R.E., and Kors, D.L., "Multiple Jet Study Final Report," NASA CR-121217, 1973.
2. Holdeman, J.D., Walker, R.E., and Kors, D.L., "Mixing of Multiple Dilution Jets with a Hot Primary Airstream for Gas Turbine Combustors," AIAA Paper 73-1249, Las Vegas, Nevada 1973 (also NASA TM X-71426).
3. Walker, R.E. and Eberhardt, R.G., "Multiple Jet Study Data Correlations," NASA CR-134795, 1975.
4. Holdeman, J.D., and Walker, R.E., "Mixing of a Row of Jets with a Confined Crossflow," AIAA Journal, Vol. 15, No. 2, Feb. 1977, pp. 243-249 (also AIAA-76-48 and NASA TM X-71787).
5. Holdeman, J.D., "Perspectives on the Mixing of a Row of Jets with a Confined Crossflow," AIAA-83-1200, 1983 (also NASA TM 83457).
6. Srinivasan, R., Berenfeld, A., and Mongia, H.C., "Dilution Jet Mixing Program - Phase I Report," NASA CR-168031, 1982.
7. Srinivasan, R., Coleman, E., and Johnson, K., "Dilution Jet Mixing Program - Phase II Report," NASA CR-174624, 1984.
8. Holdeman, J.D., Srinivasan, R., and Berenfeld, A., "Experiments in Dilution Jet Mixing," AIAA Journal, Vol. 22, No. 10, October 1984, pp. 1436-1443 (also AIAA-83-1201 and NASA TM 83434).
9. Wittig, S.L.K., Elbahar, O.M.F., and Noll, B.E., "Temperature Profile Development in Turbulent Mixing of Coolant Jets with a Confined Hot Cross-Flow," ASME Paper No. 83-GT-39, March 1983.
10. Holdeman, J.D., and Srinivasan, R., "On Modeling Dilution Jet Flowfields," AIAA-84-1379, 1984 (also NASA TM 83708).
11. Claus, R.W., "Analytical Calculation of a Single Jet in Crossflow and Comparison with Experiment," AIAA Paper 83-0238, January 1983 (NASA TM 83027).
12. Srinivasan, R., et al., "Aerothermal Modeling Program: Phase I Final Report," Garrett Turbine Engine Company, Phoenix, Arizona, Garrett 21-4742, August 1983 (NASA CR-168243).



## LIST OF SYMBOLS

A	Test section cross-sectional area at survey plane
AR	Aspect Ratio (frontal width/streamwise length)
D	Geometric orifice diameter
$D_j$	Effective orifice diameter
$H_0$	Duct height at the jet injection plane
H	Local duct height at the survey plane
$H_{EQ}$	Local equivalent channel height
J	Momentum flux ratio $\rho_j V_j^2 / \rho_m V_m^2$
$P_t$	Stagnation pressure
$P_s$	Static pressure
S	Orifice spacing
$S_x$	Axial spacing between two rows of jets
T	Temperature
V	Velocity
$W_{\frac{1}{2}}$	Jet Half Width
X	x direction, parallel to duct axis
Y	y direction, parallel to orifice centerline (radial direction)
Z	z direction, normal to duct axis (transverse direction)

### Greek

$\theta$	Temperature difference ratio
$\rho$	Density

### Subscripts

av	average
EB	Equilibrium value
j	Jet property
max	Maximum

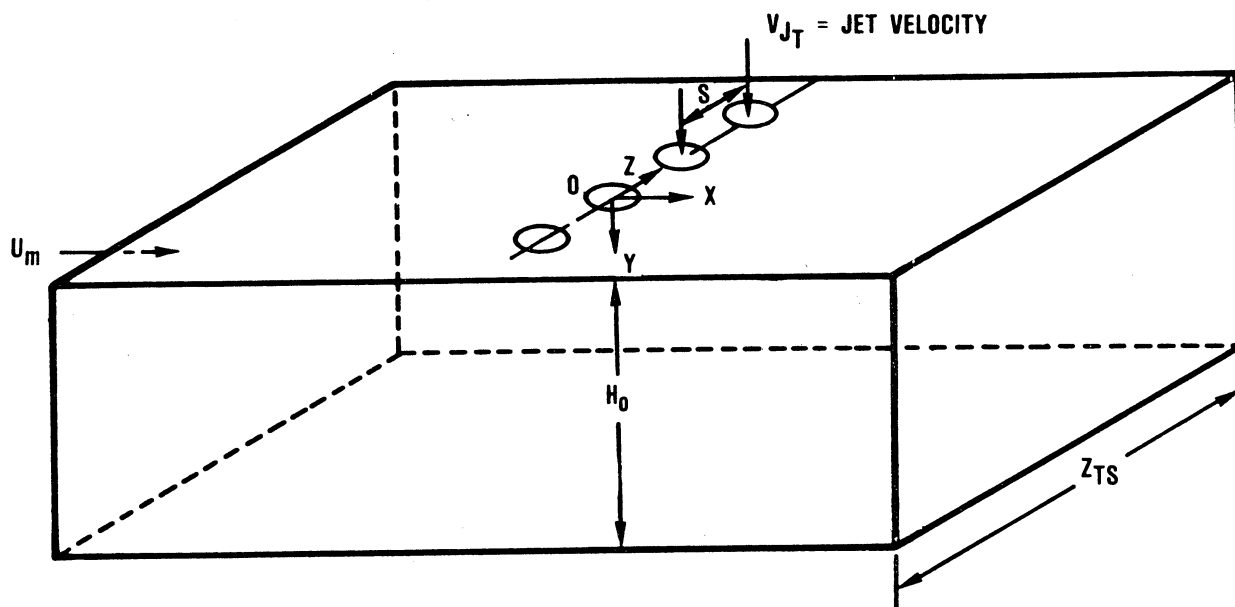
## LIST OF SYMBOLS

### Subscripts (contd)

- m Cross-flow property, average value
- F First or lead row of dilution jets
- A Aft row of dilution jets

### Superscripts

- + Beyond the jet centerline
- Before the jet centerline (towards jet injection wall)



COORDINATE ORIGIN IS LOCATED AT CENTER OF ORIFICE

$U_m, \rho_m, T_m$  = MAINSTREAM VELOCITY, DENSITY, AND TEMPERATURE

$V_j, \rho_j, T_j$  = INITIAL JET VELOCITY, DENSITY, AND TEMPERATURE

$H_0$  = TEST-SECTION HEIGHT AT INJECTION PLANE

$H$  = TEST-SECTION HEIGHT AT ANY X-Y PLANE

$S$  = ORIFICE SPACING ALONG Z (TRANSVERSE) DIRECTION

$D$  = ORIFICE DIAMETER

$D_j$  =  $\sqrt{C_D} D$

$z_{TS}$  = TEST-SECTION TRANSVERSE DIMENSION = 305mm

Figure 1. Multiple Jet Study Coordinate System and Important Nomenclature.

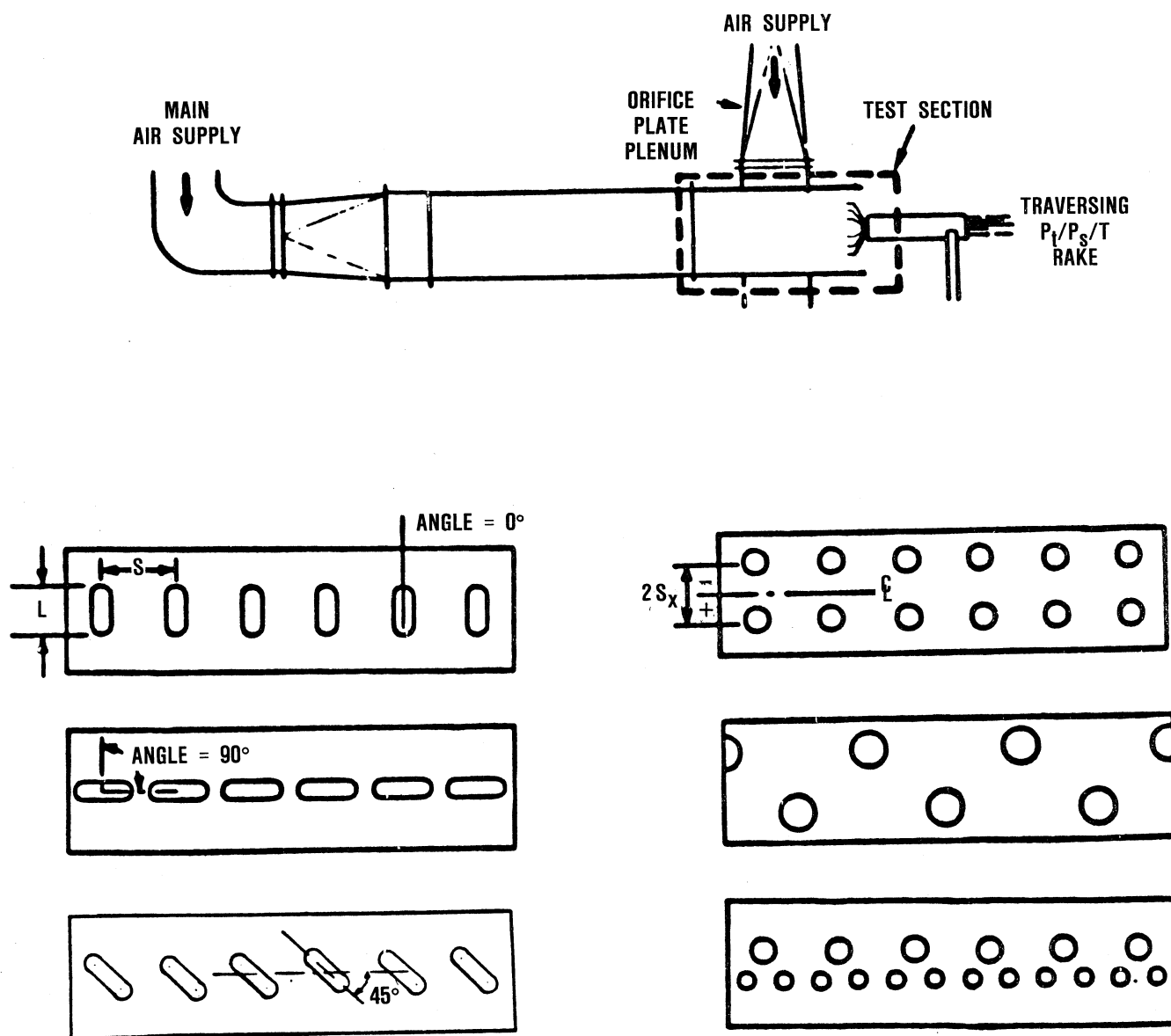


Figure 2. Dilution Jet Mixing Rig Schematic and Orifice Plates.

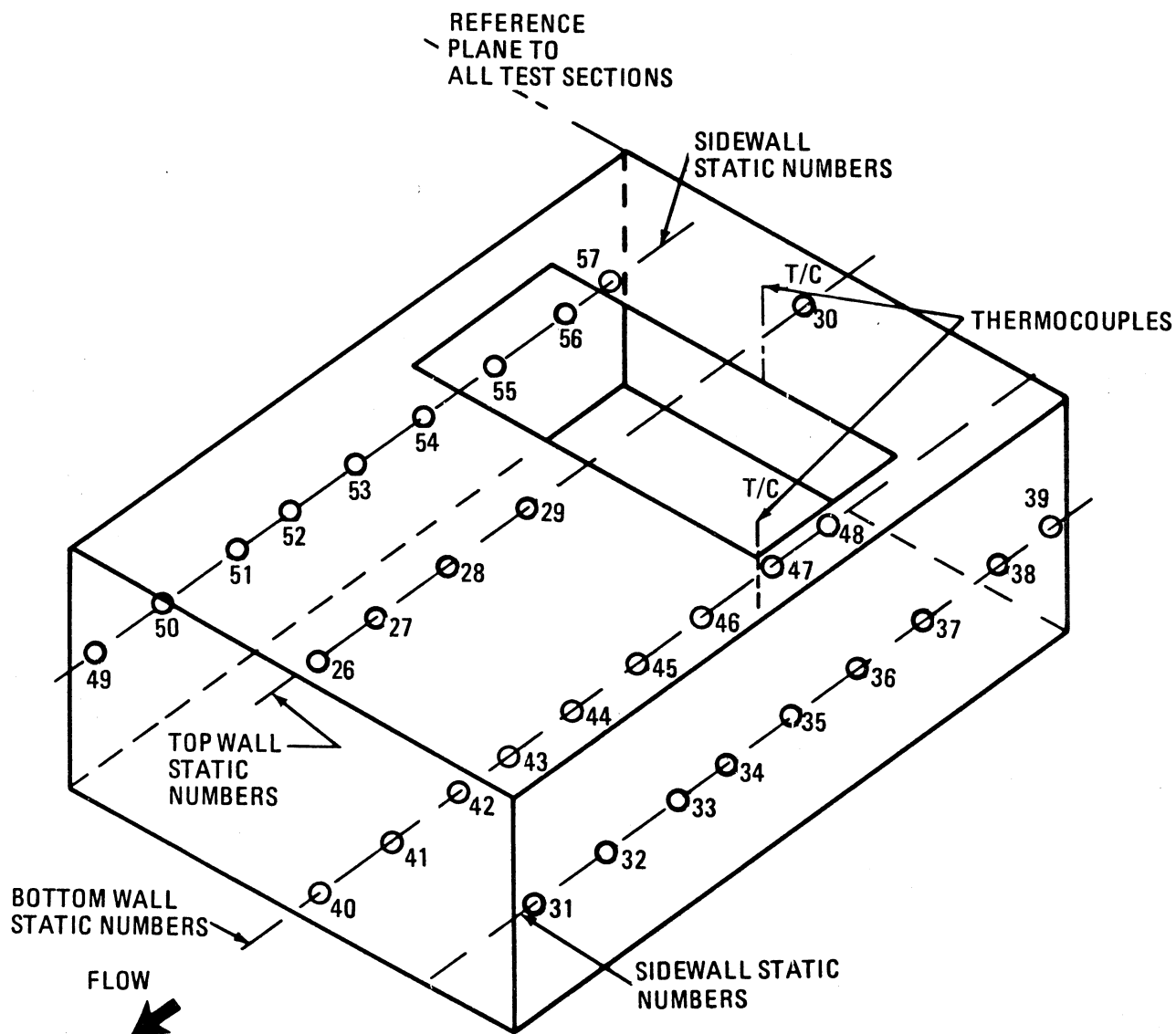


Figure 3. Wall Statics and Thermocouples in the Test Section.

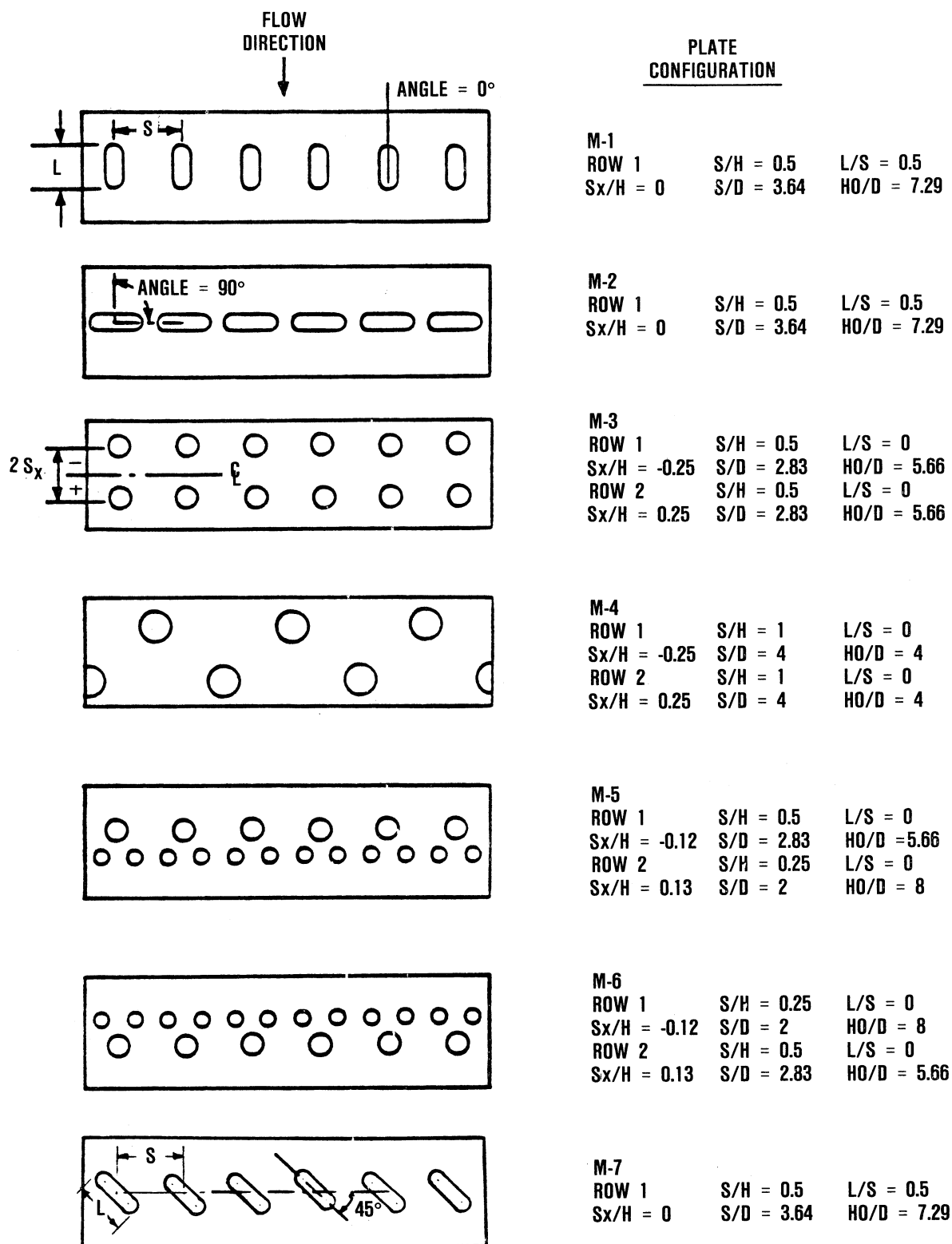


Figure 4. Dilution Orifice Plate Configurations.



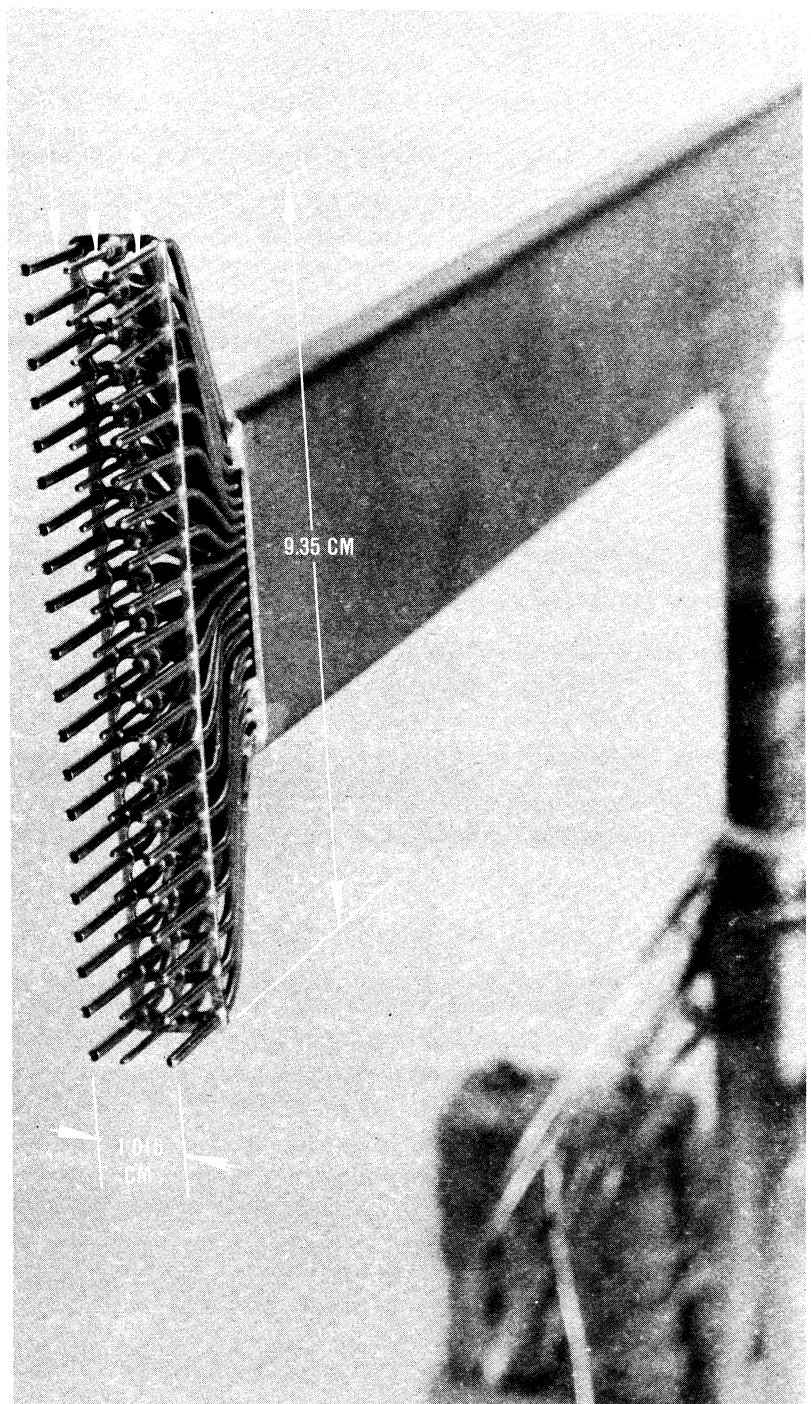
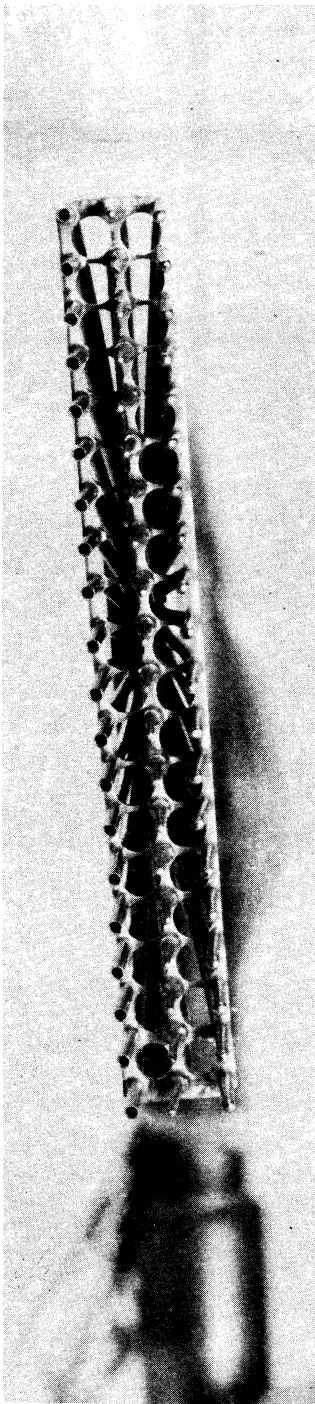


Figure 5. Total Pressure, Thermocouple, and Static Pressure Rake.

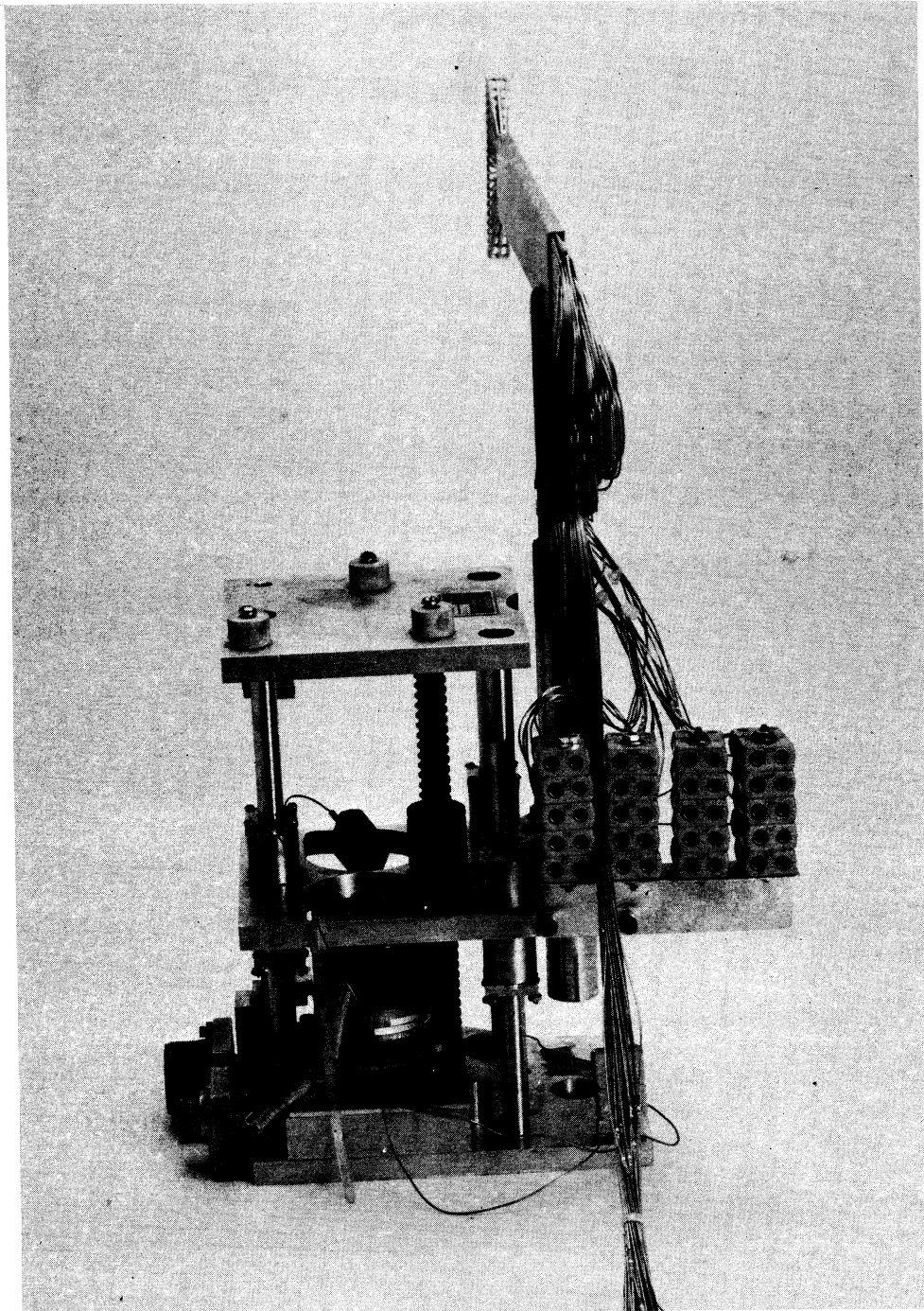


Figure 6. X-Y-Z Actuator with the Rake Mounted Thereon.

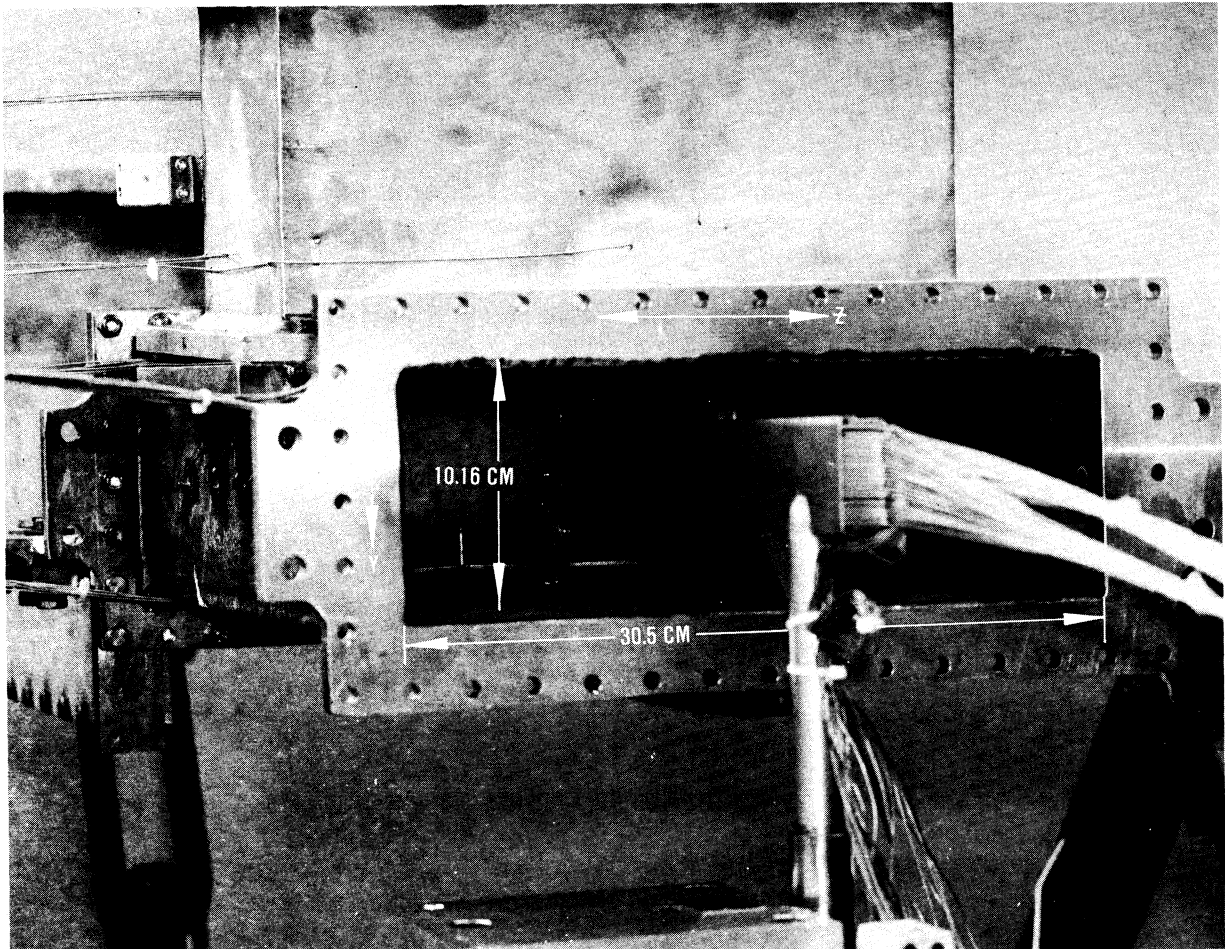


Figure 7. Jet Mixing Rig as Viewed from Rig Discharge End.



S = 0.0508 METERS S/DJ = 2.288 HO/DJ = 4.576 VMAIN = 17.8 M/SEC VJET = 30.9 M/SEC TMAIN = 690.1 K TJET = 317.1 K THEB = 0.2216 BLORAT= 3.795 DENRATIO= 2.181 TRATIO=0.460

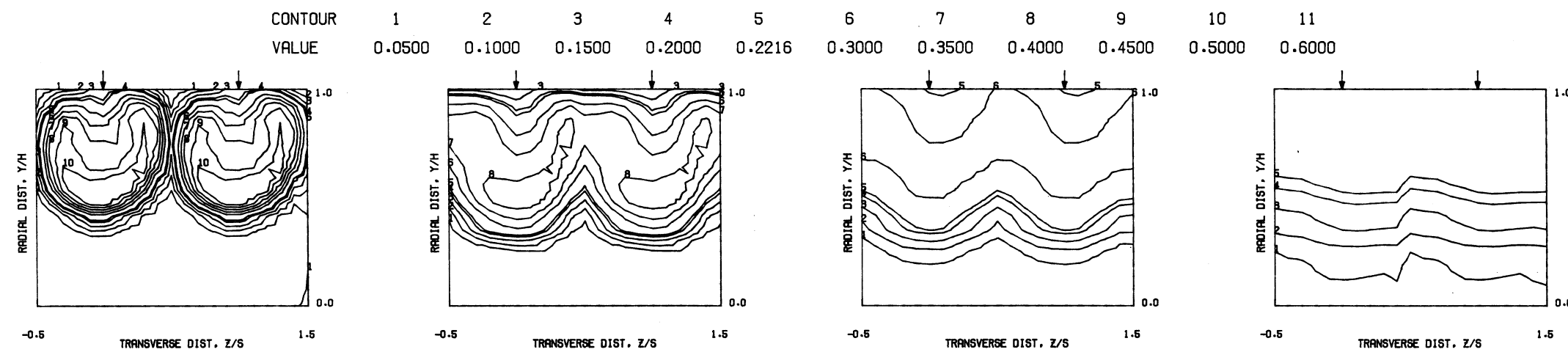
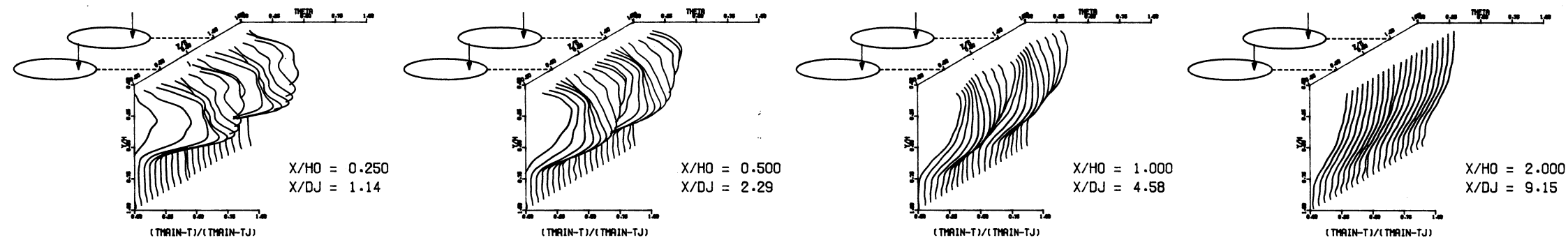
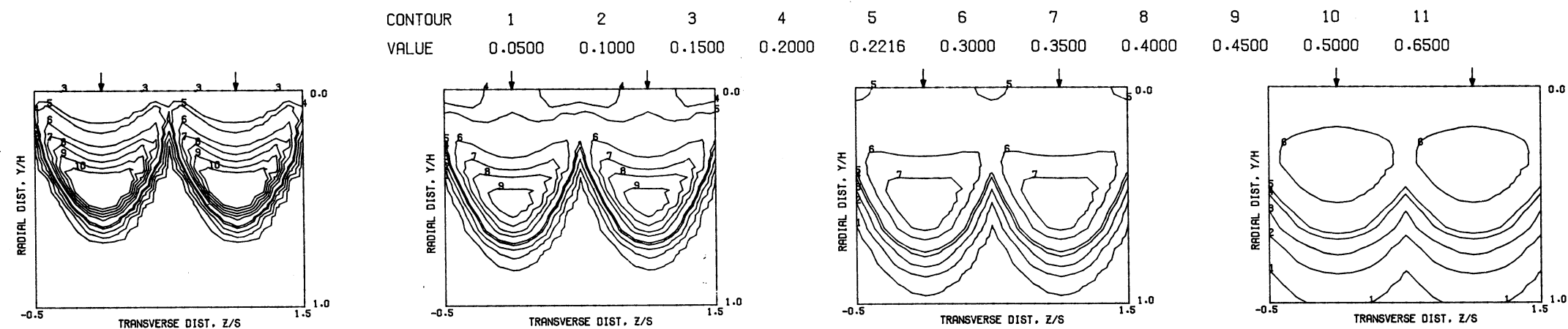
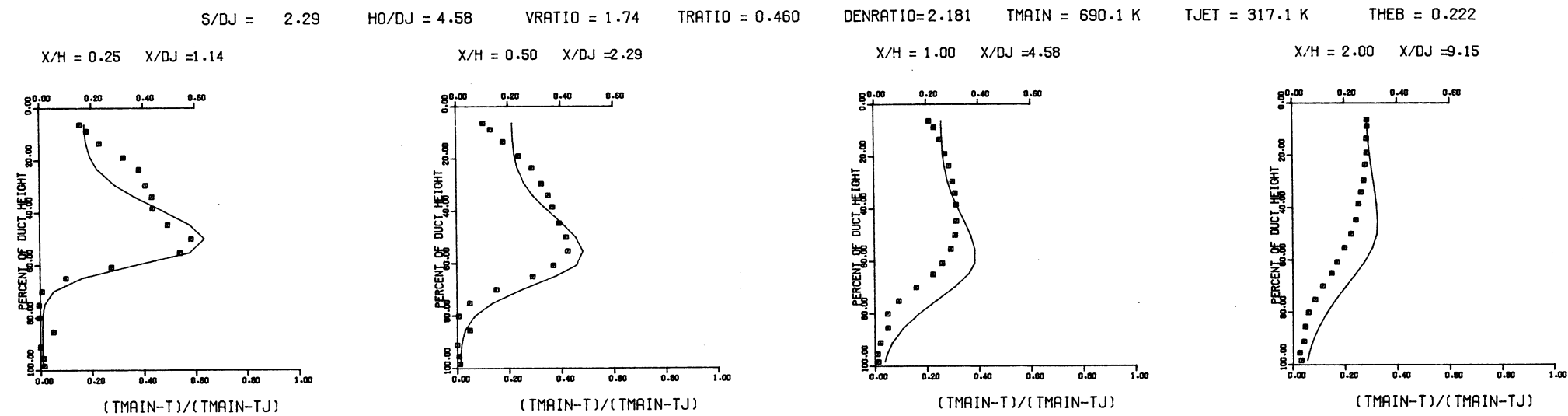


Figure 8. Measured Theta Distribution for Test No. 1.



PREDICTED THETA CONTOURS FOR TEST NO. 1, S.L.SLOT,  $J=6.60$ ,  $S/D=2.00$ ,  $H/D=4.00$



COMPARISON BETWEEN DATA AND CORRELATIONS FOR TEST NO. 1, TEST SECTION I.S.L. SLOT,  $J = 6.60$ ,  $S/D = 2.00$ ,  $H/D = 4.00$

Figure 9. Predicted Theta Distributions for Test No. 1.

S = 0.0508 METERS S/DJ = 2.379 HO/DJ = 4.758 VMAIN = 16.7 M/SEC VJET = 58.5 M/SEC TMAIN = 661.0 K TJET = 307.3 K THEB = 0.3447 BLORAT= 7.581 DENRATIO= 2.171 TRATIO= 0.465

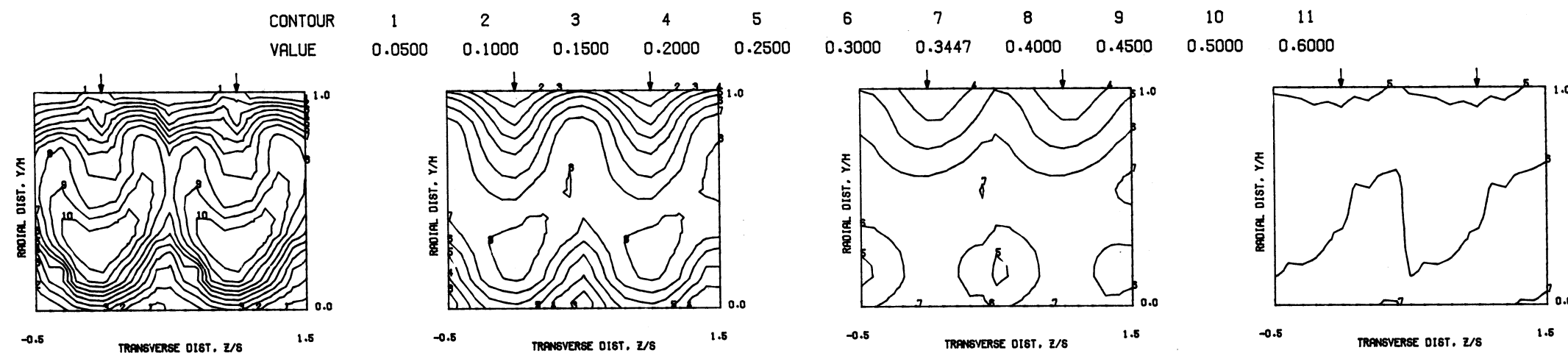
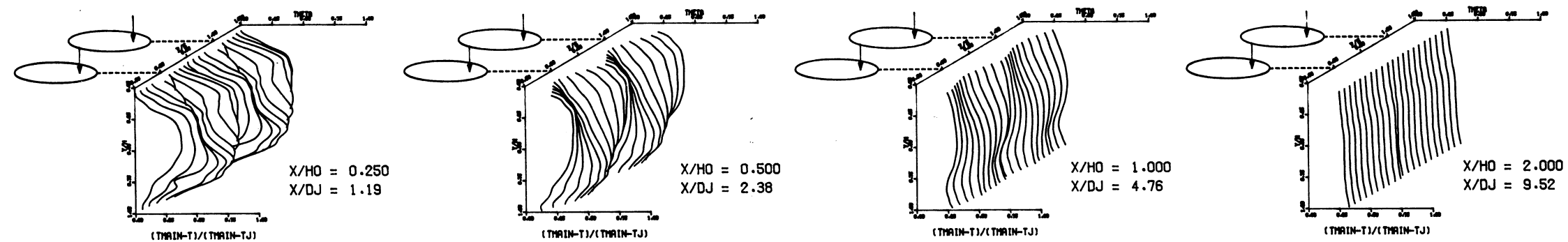
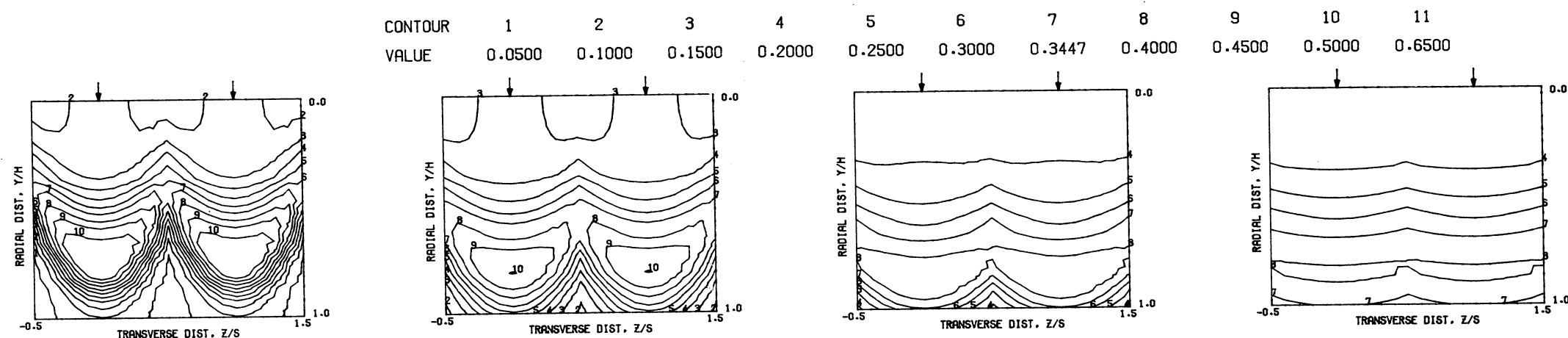
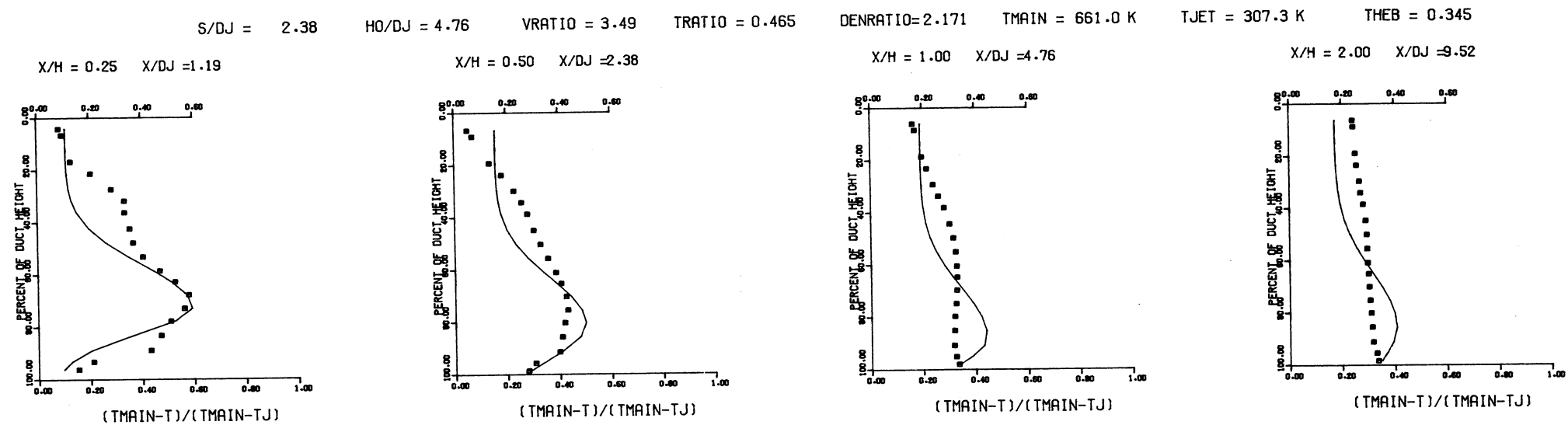


Figure 10. Measured Theta Distributions for Test No. 2.





PREDICTED THETA CONTOURS FOR TEST NO. 2, S.L.SLOT,  $J=26.47$ ,  $S/D=2.00$ ,  $H/D=4.00$



COMPARISON BETWEEN DATA AND CORRELATIONS FOR TEST NO. 2, TEST SECTION I, S.L. SLOT,

$J = 26.47$  ,  $S/D = 2.00$  ,  $H/D = 4.00$

Figure 11. Predicted Theta Distributions for Test No. 2.



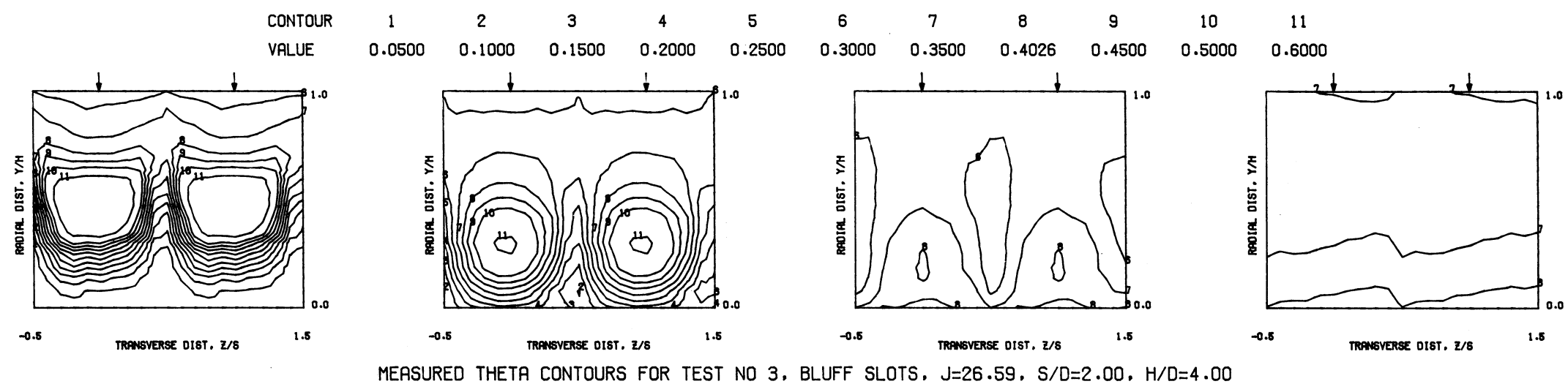
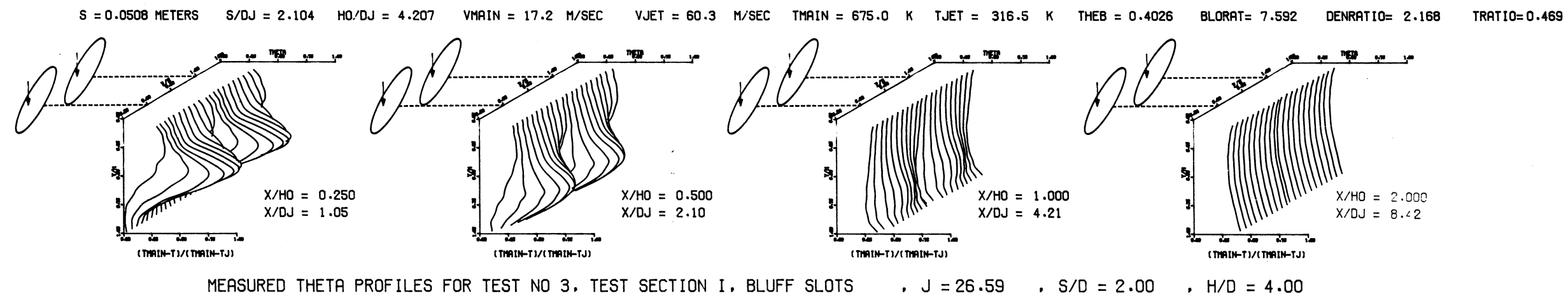
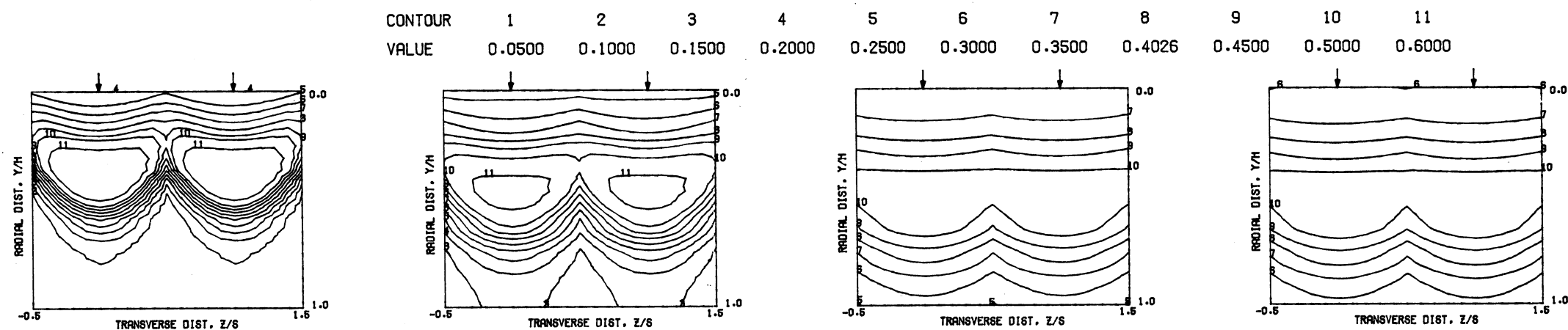
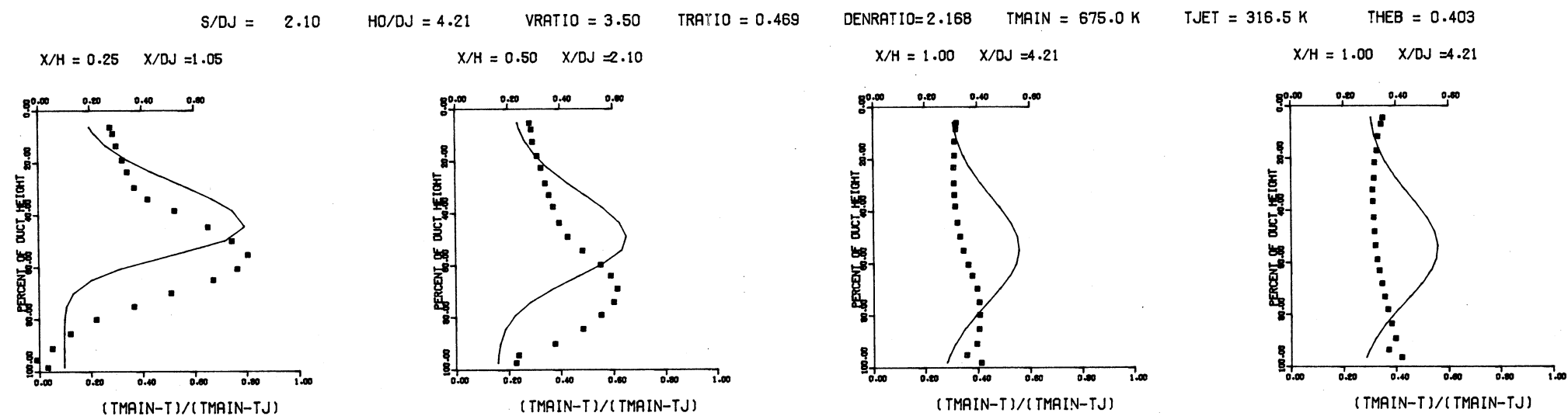


Figure 12. Measured Theta Distributions for Test No. 3.



PREDICTED THETA CONTOURS FOR TEST NO. 3, BLUFF SLOT,  $J=26.59$ ,  $S/D=2.00$ ,  $H/D=4.00$

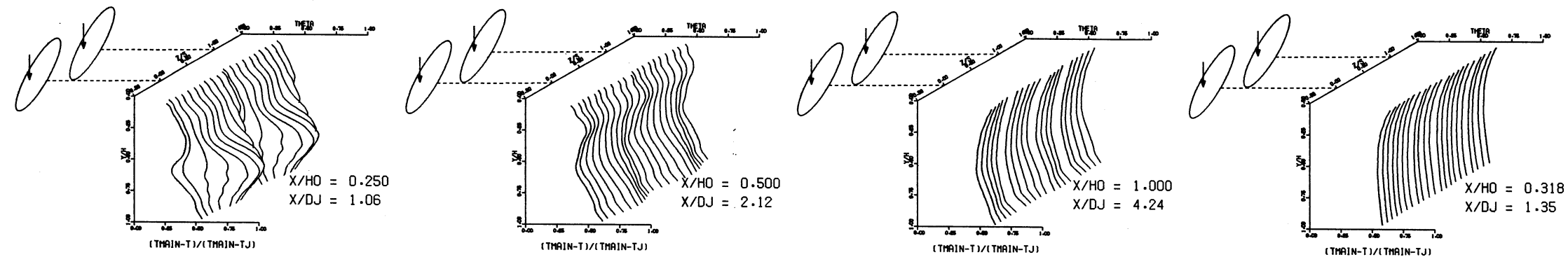


COMPARISON BETWEEN DATA AND CORRELATIONS FOR TEST NO. 3, TEST SECTION I, BLUFF SLOT,

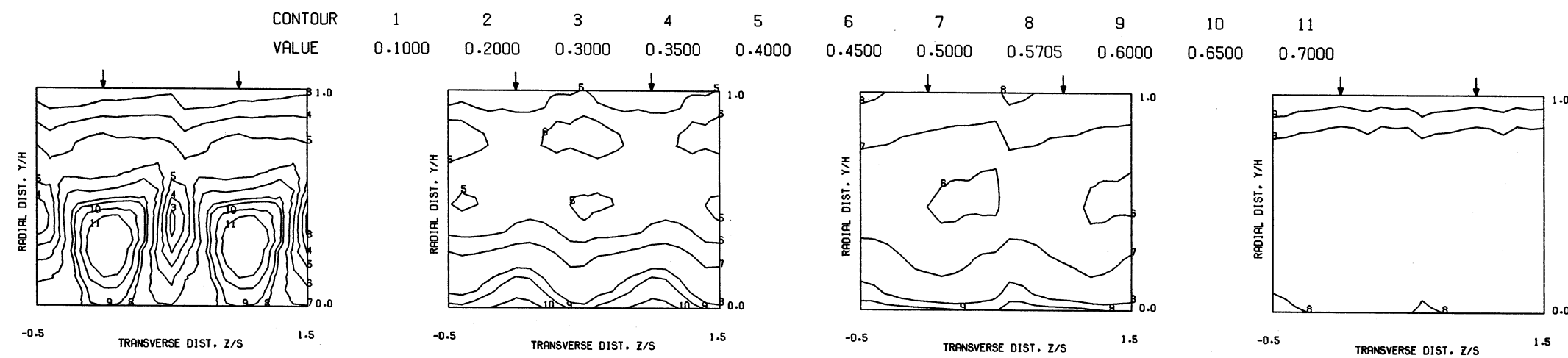
$J = 26.59$ ,  $S/D = 2.00$ ,  $H/D = 4.00$

Figure 13. Predicted Theta Distributions for Test No. 3.

S = 0.0508 METERS   S/DJ = 2.118   HO/DJ = 4.237   VMAIN = 12.6 M/SEC   VJET = 88.8 M/SEC   TMAIN = 655.3 K   TJET = 315.0 K   THEB = 0.5705   BLORAT= 15.183   DENRATIO= 2.161   TRATIO=0.481

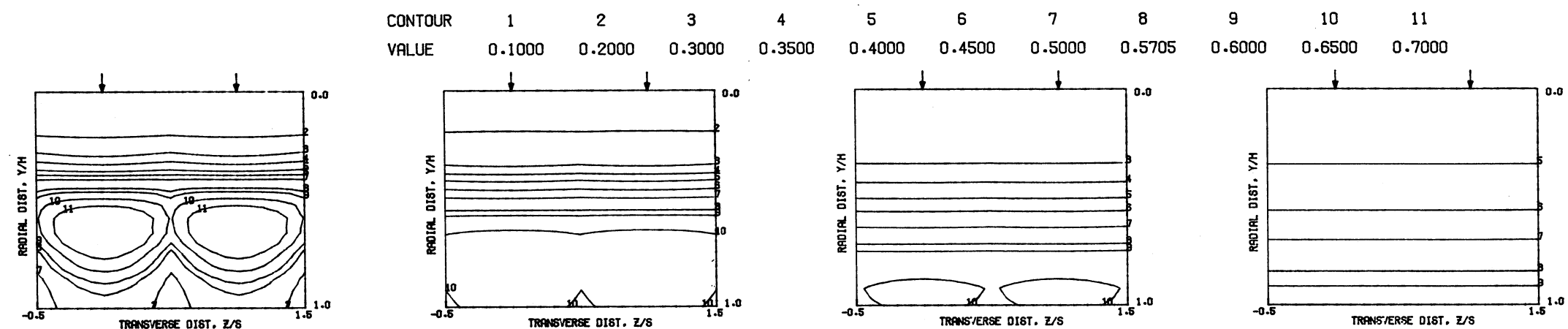


MEASURED THETA PROFILES FOR TEST NO 4, TEST SECTION I, BLUFF SLOTS , J = 106.69 , S/D = 2.00 , H/D = 4.00

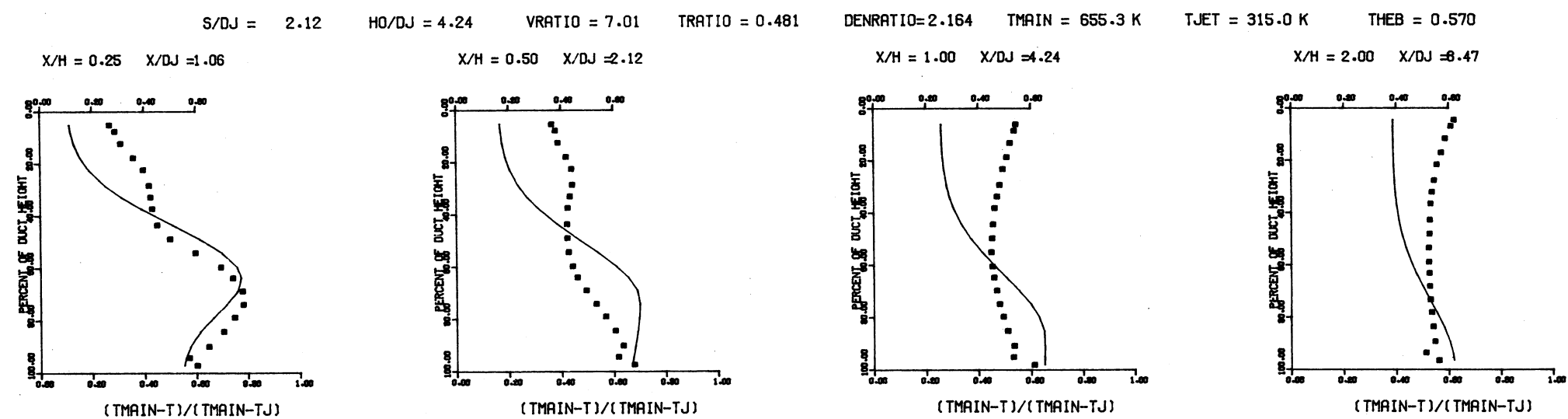


MEASURED THETA CONTOURS FOR TEST NO 4, BLUFF SLOTS, J=106.5, S/D=2.00, H/D=4.00

Figure 14. Measured Theta Distributions for Test No. 4.



PREDICTED THETA CONTOURS FOR TEST NO. 4, BLUFF SLOT,  $J=106.5$ ,  $S/D=2.00$ ,  $H/D=4.00$



COMPARISON BETWEEN DATA AND CORRELATIONS FOR TEST NO. 4, TEST SECTION I, BLUFF SLOT,

$J = 106.46$ ,  $S/D = 2.00$ ,  $H/D = 4.00$

Figure 15. Predicted Theta Distributions for Test No. 4.

S = 0.0508 METERS    S/DJ = 3.476    HO/DJ = 6.952    VMAIN = 17.7 M/SEC    VJET = 30.9 M/SEC    TMAIN = 690.3 K    TJET = 319.2 K    THEB = 0.1978    BLORAT= 3.800    DENRATIO= 2.172    TRATIO=0.462

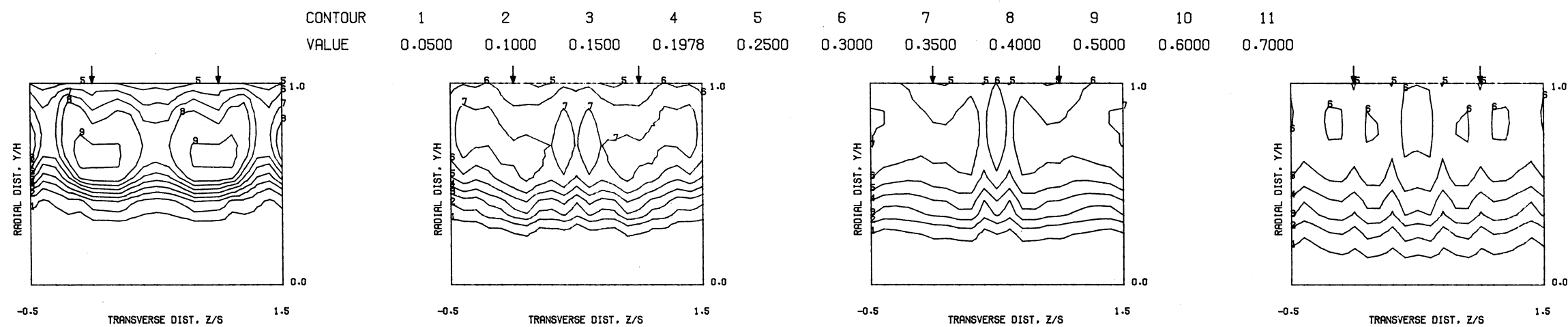
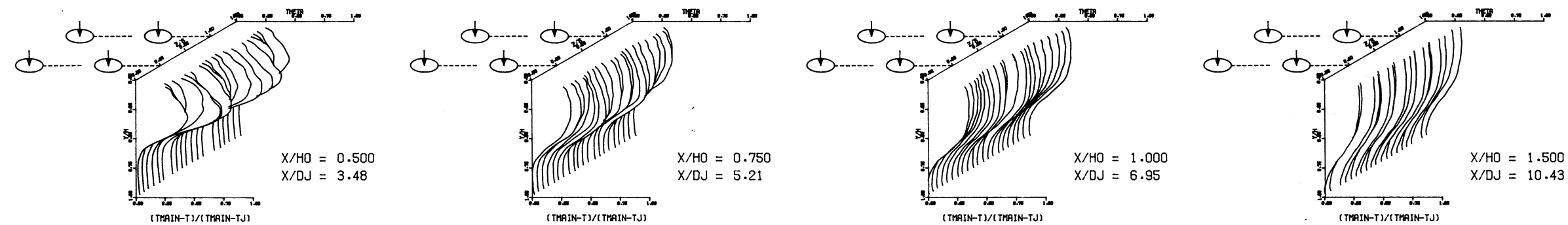
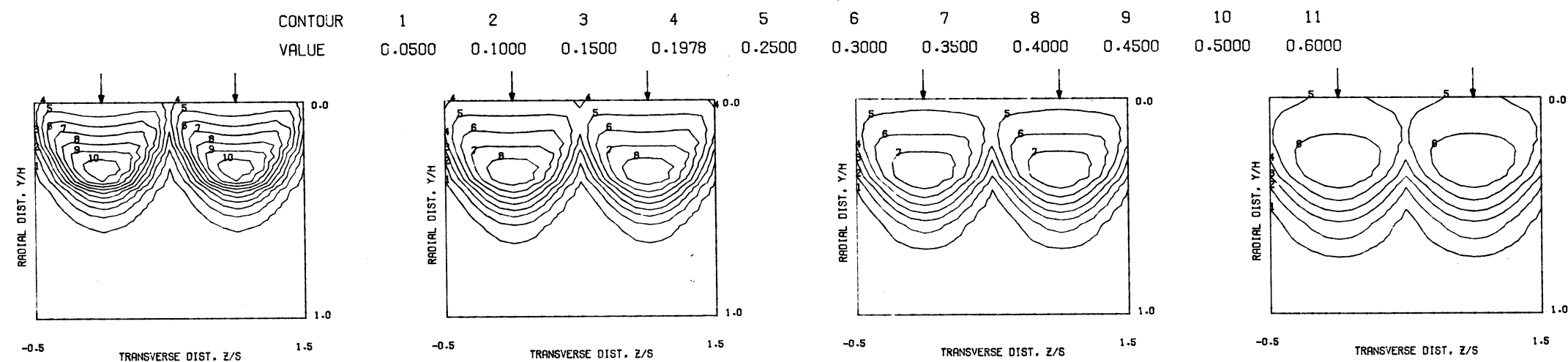
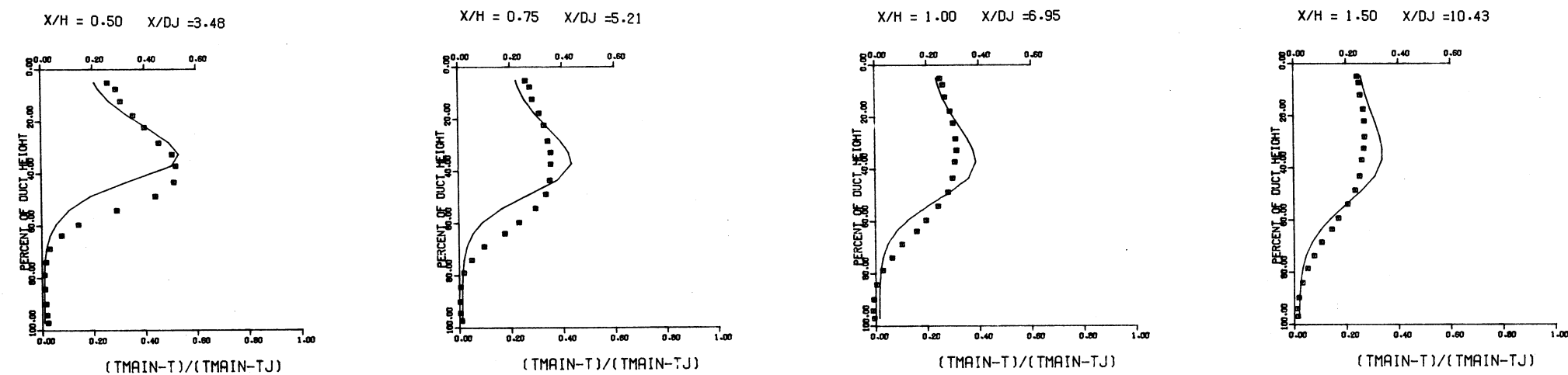


Figure 16. Measured Theta Distributions for Test No. 5.



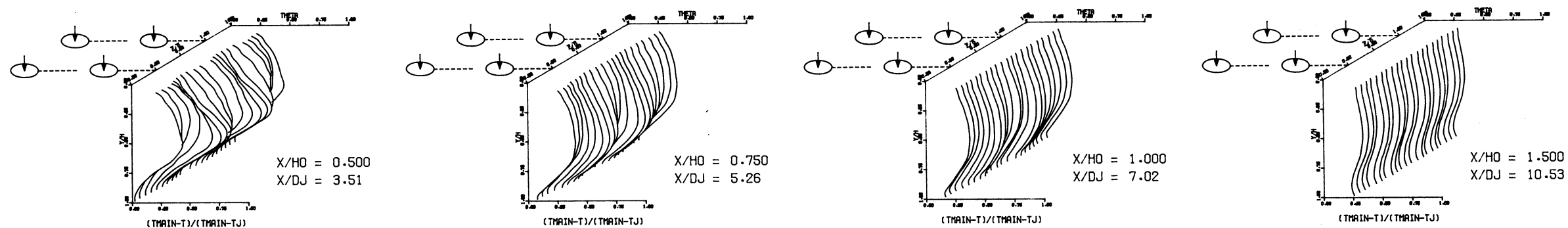
$S/DJ = 3.48$     $HO/DJ = 6.95$     $VRATIO = 1.75$     $TRATIO = 0.462$     $DENRATIO=2.172$     $TMAIN = 690.3 \text{ K}$     $TJET = 319.2 \text{ K}$     $THEB = 0.197$



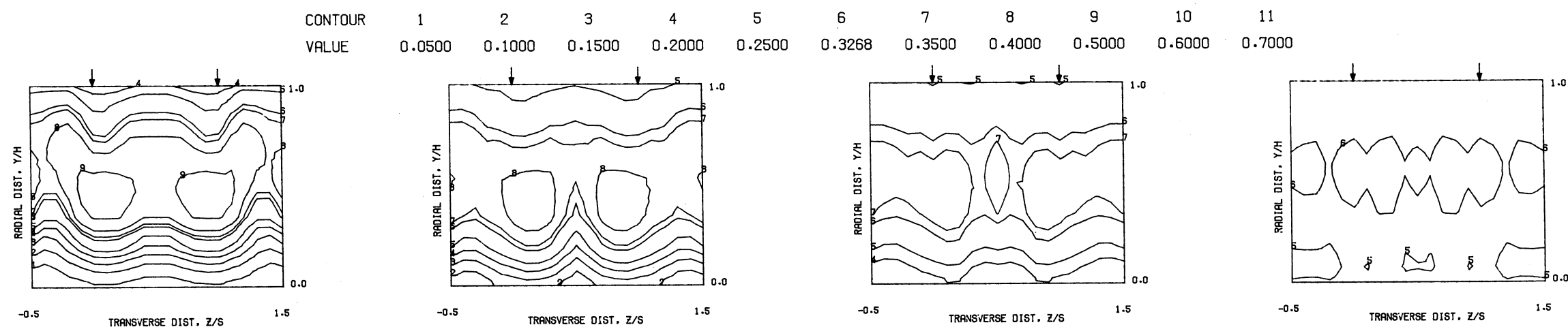
COMPARISON BETWEEN DATA AND CORRELATIONS FOR TEST NO 5, TEST SECTION I, PLATE M3(INL),  $J = 6.65$  ,  $S/D = 2.83$  ,  $H/D = 5.66$

Figure 17. Predicted Theta Distributions for Test No. 5.

S = 0.0508 METERS S/DJ = 3.510 HO/DJ = 7.020 VMAIN = 17.1 M/SEC VJET = 59.2 M/SEC TMAIN = 665.9 K TJET = 310.4 K THEB = 0.3268 BLORAT= 7.574 DENRATIO= 2.184 TRATIO=0.466

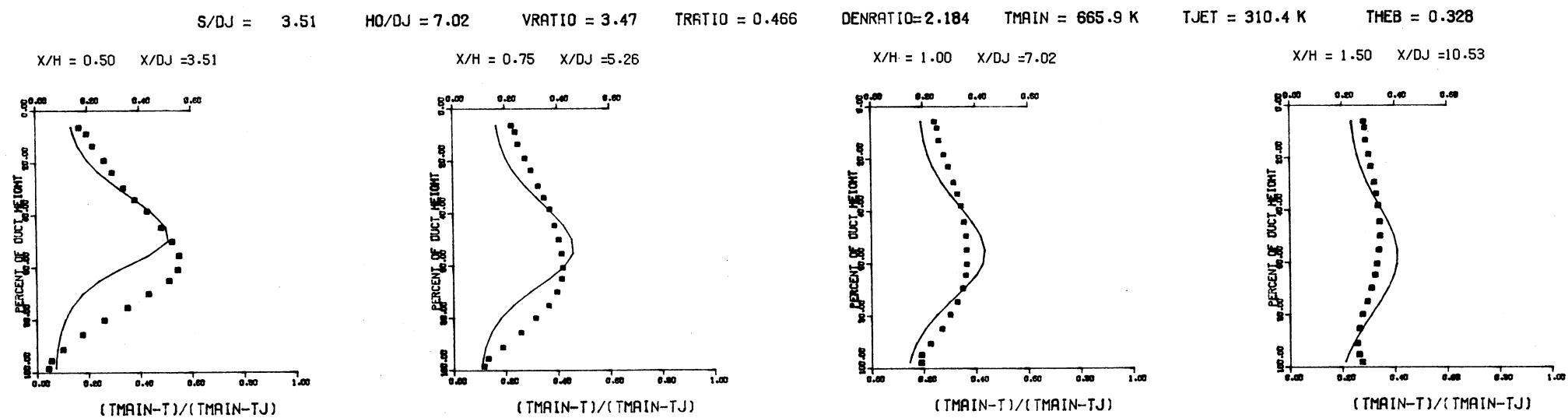
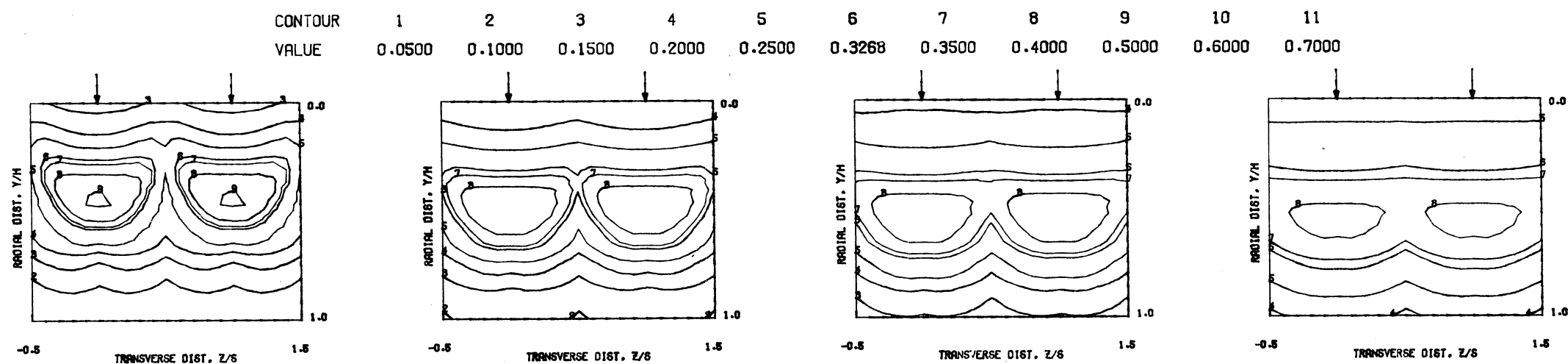


MEASURED THETA PROFILES FOR TEST NO. 6, TEST SECTION I, PLATE M3 (INL), J = 26.27, S/D = 2.83, H/D = 5.66



MEASURED THETA CONTOURS FOR TEST NO 6, PLATE M3, J=26.27, S/D=2.83, H/D=5.66

Figure 18. Measured Theta Distributions for Test No. 6.



COMPARISON BETWEEN DATA AND CORRELATIONS FOR TEST NO 6, TEST SECTION I, PLATE M3(INL), J = 26.27 , S/D =2.83 , H/D =5.66

Figure 19. Predicted Theta Distributions for Test No. 6.



S = 0.0508 METERS S/DJ = 3.618 HO/DJ = 7.236 VMAIN = 16.3 M/SEC VJET = 113.9 M/SEC TMAIN = 636.7 K TJET = 309.6 K THEB = 0.4780 BLORAT= 15.307 DENRATIO= 2.186 TRATIO=0.486

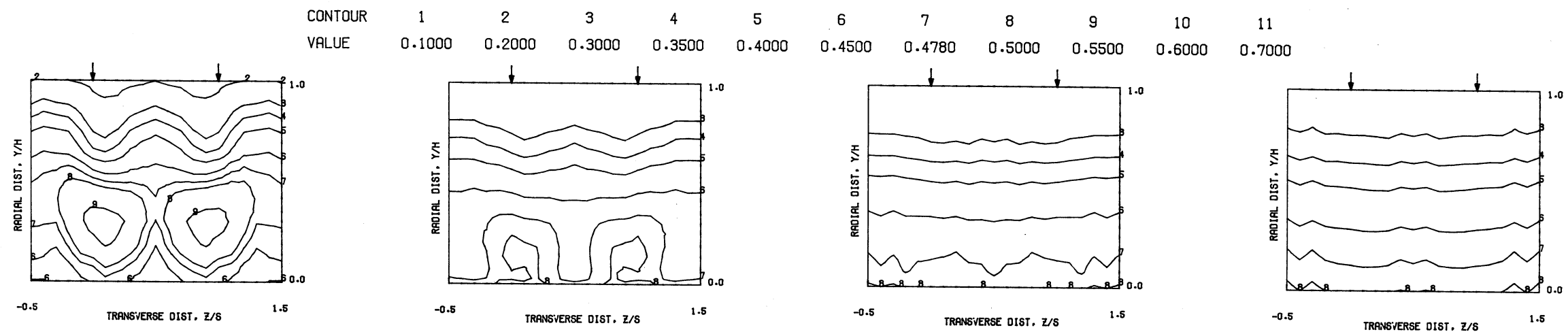
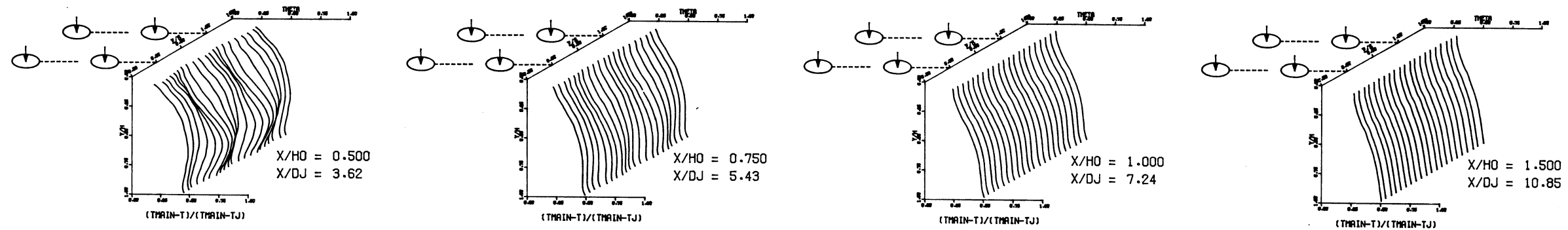
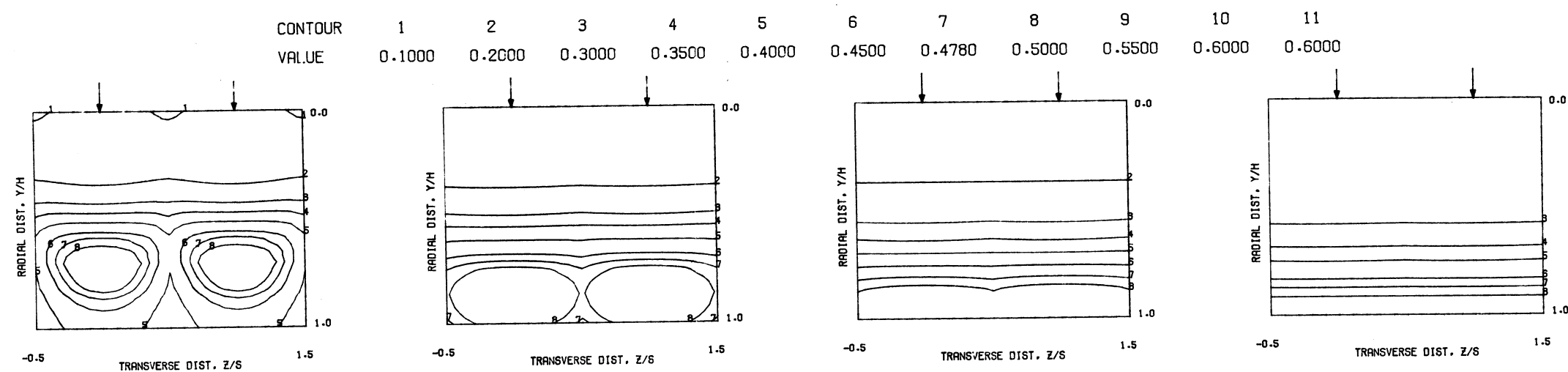
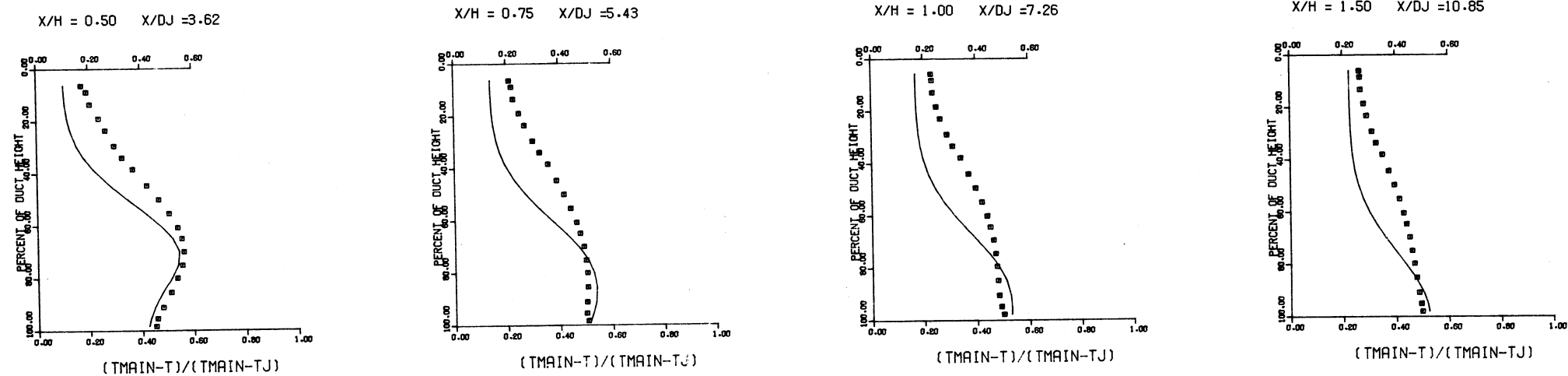


Figure 20. Measured Theta Distributions for Test No. 7.



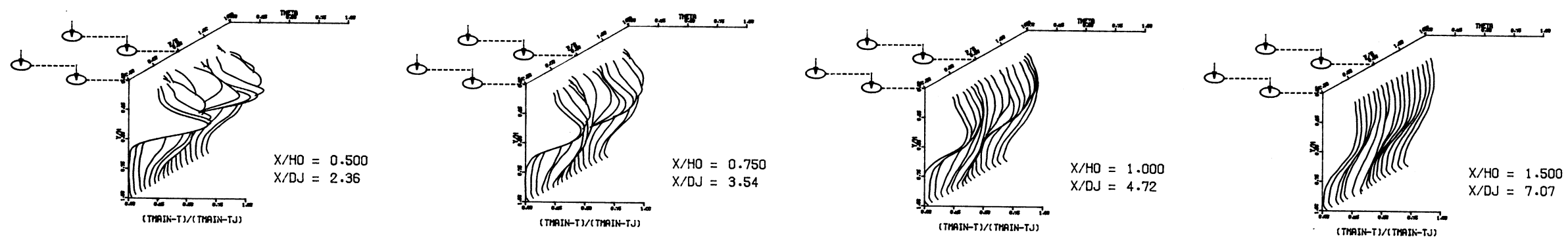
$S/DJ = 3.62$     $HO/DJ = 7.24$     $VRATIO = 7.00$     $TRATIO = 0.486$     $DENRATIO=2.186$     $TMAIN = 636.7 \text{ K}$     $TJET = 309.6 \text{ K}$     $THEB = 0.477$



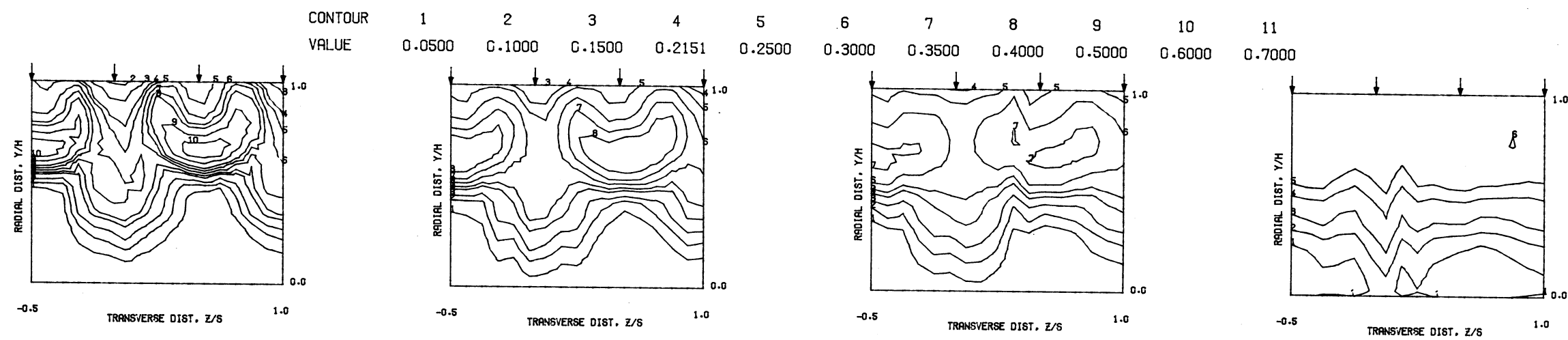
COMPARISON BETWEEN DATA AND CORRELATIONS FOR TEST NO 7, TEST SECTION I, PLATE M3(INL),  $J = 107.18$ ,  $S/D = 2.83$ ,  $H/D = 5.66$

Figure 21. Predicted Theta Distributions for Test No. 7.

S = 0.1016 METERS S/DJ = 4.716 HO/DJ = 4.716 VMAIN = 17.4 M/SEC VJET = 30.4 M/SEC TMAIN = 682.0 K TJET = 314.0 K THEB = 0.2151 BLORAT= 3.817 DENRATIO= 2.183 TRATIO= 0.460

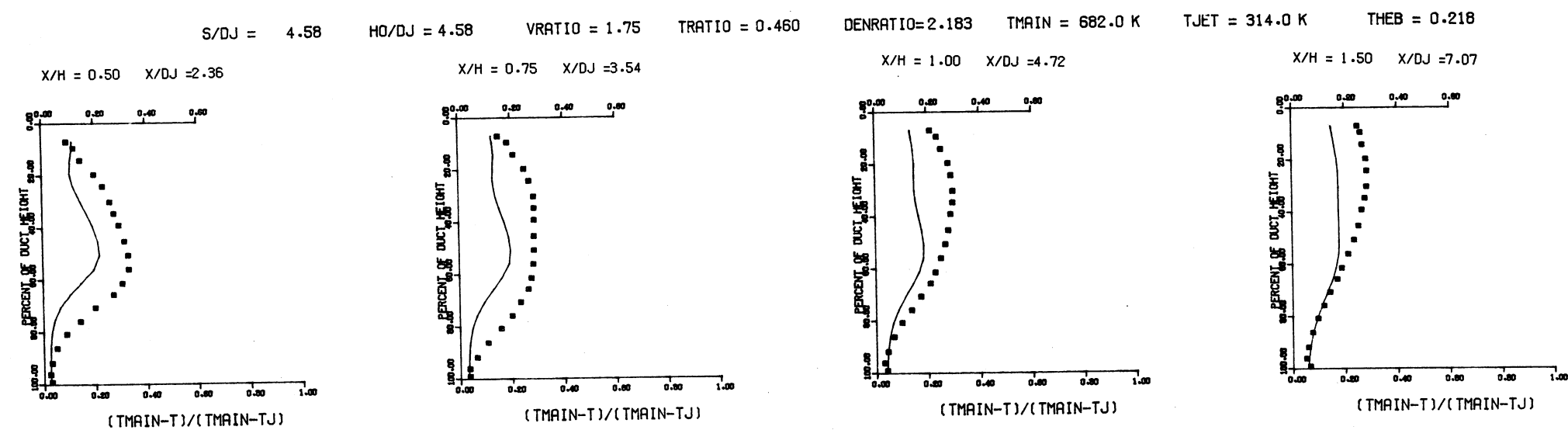
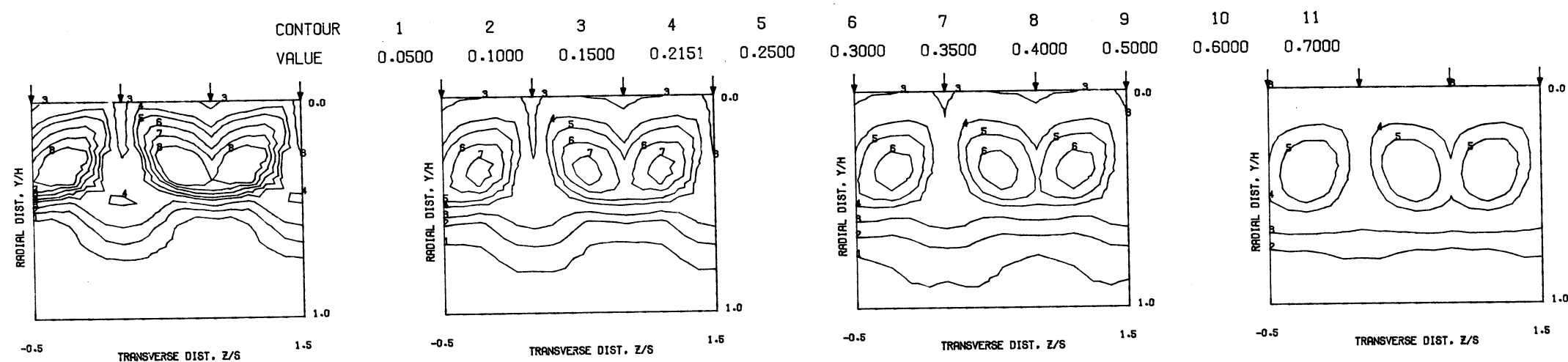


MEASURED THETA PROFILES FOR TEST NO. 8, TEST SECTION I, PLATE M4 (STG), J = 6.67, S/D = 4.00, H/D = 4.00



MEASURED THETA CONTOURS FOR TEST NO 8, PLATE M4, J=6.67, S/D=4.00, H/D=4.00

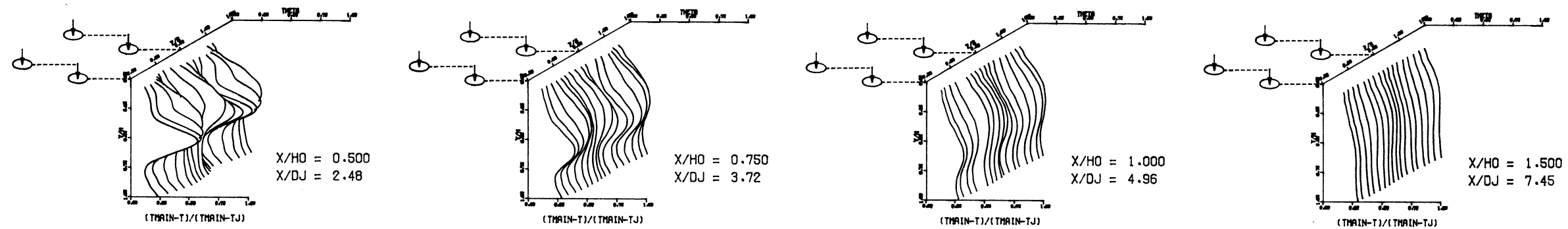
Figure 22. Measured Theta Distributions for Test No. 8.



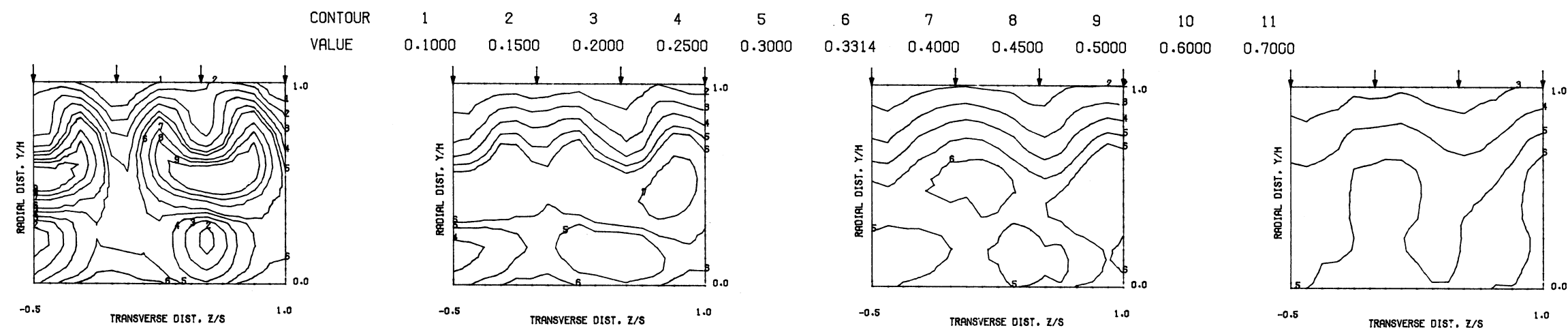
COMPARISON BETWEEN DATA AND CORRELATIONS FOR TEST NO 8, TEST SECTION I, PLATE M4(STG), J = 6.67, S/D = 4.00, H/D = 4.00

Figure 23. Predicted Theta Distributions for Test No. 8.

S = 0.1016 METERS S/DJ = 4.964 HO/DJ = 4.964 VMAIN = 17.3 M/SEC VJET = 60.7 M/SEC TMAIN = 671.6 K TJET = 313.5 K THEB = 0.3314 BLORAT= 7.649 DENRATIO= 2.185 TRATIO=0.467

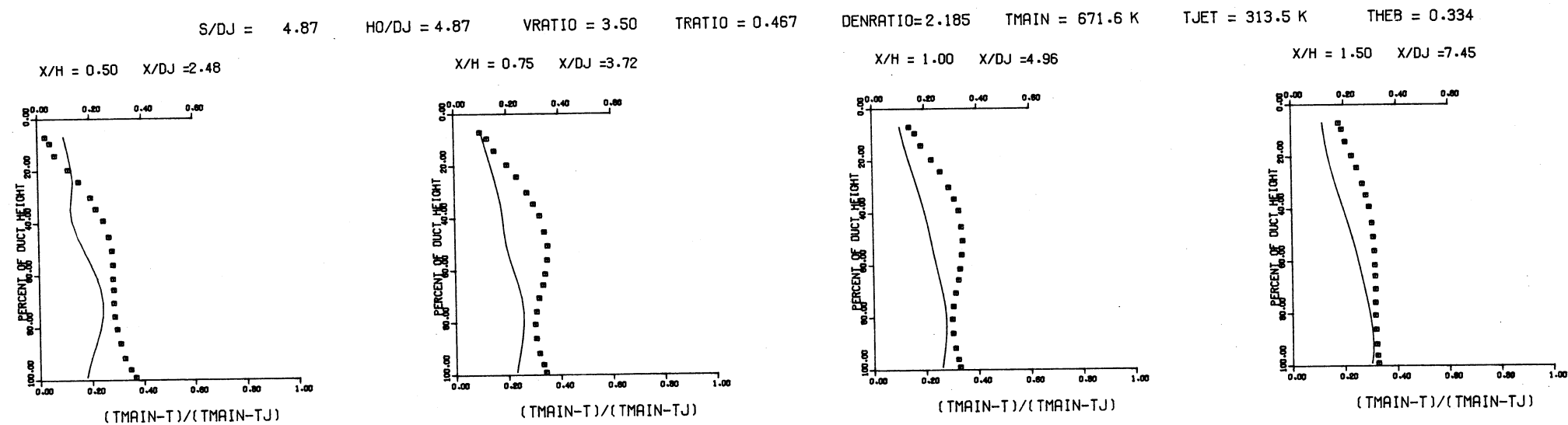
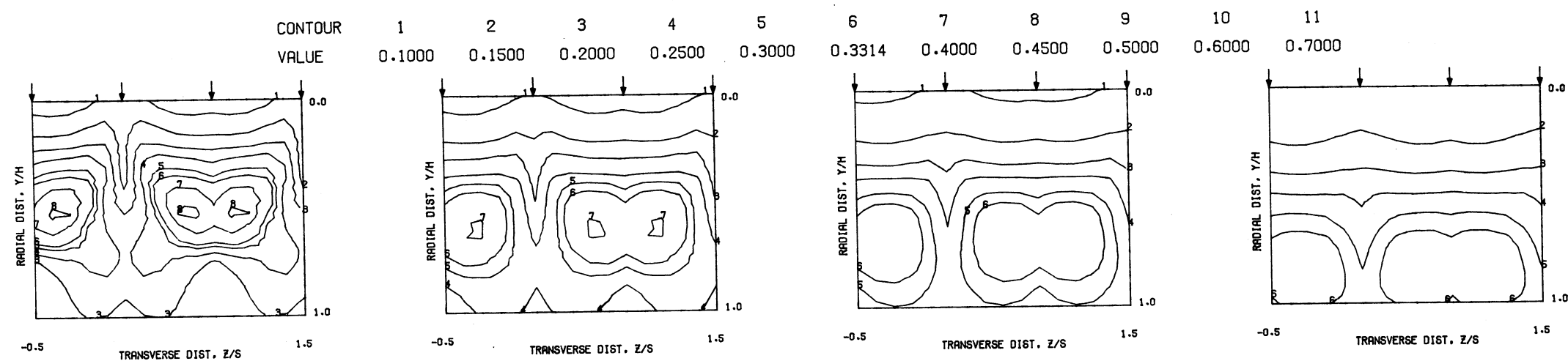


MEASURED THETA PROFILES FOR TEST NO. 9, TEST SECTION I, PLATE M4(STG) , J = 26.77 , S/D = 4.00 , H/D = 4.00



MEASURED THETA CONTOURS FOR TEST NO 9, PLATE M4 , J=26.77, S/D=4.00, H/D=4.00

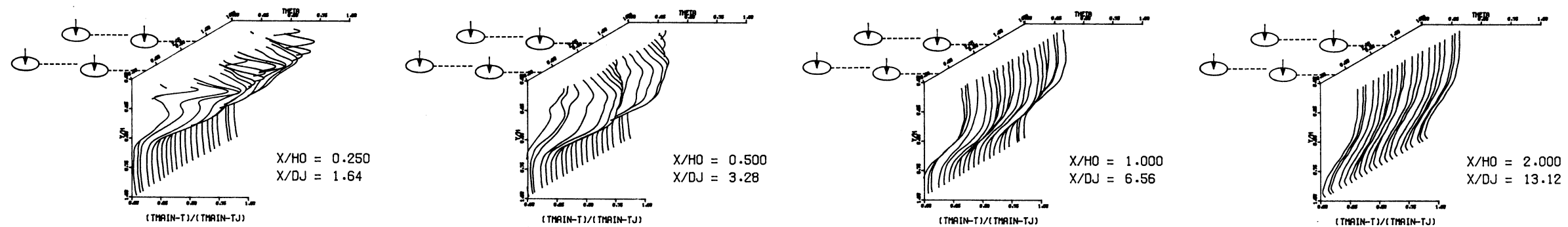
Figure 24. Measured Theta Distributions for Test No. 9.



COMPARISON BETWEEN DATA AND CORRELATIONS FOR TEST NO 9, TEST SECTION I, PLATE M4(STG), J = 26.77, S/D = 4.00, H/D = 4.00

Figure 25. Predicted Theta Distributions for Test No. 9.

S = 0.0508 METERS S/DJ = 3.280 HO/DJ = 6.560 VMAIN = 17.8 M/SEC VJET = 31.2 M/SEC TMAIN = 695.5 K TJET = 321.1 K THEB = 0.2194 BLORAT= 3.825 DENRATIO= 2.178 TRATIO=0.462



MEASURED THETA PROFILES FOR TEST NO. 10, TEST SECTION I, PLATE M5 , J = 6.72 , S/D = 2.83 , H/D = 5.66

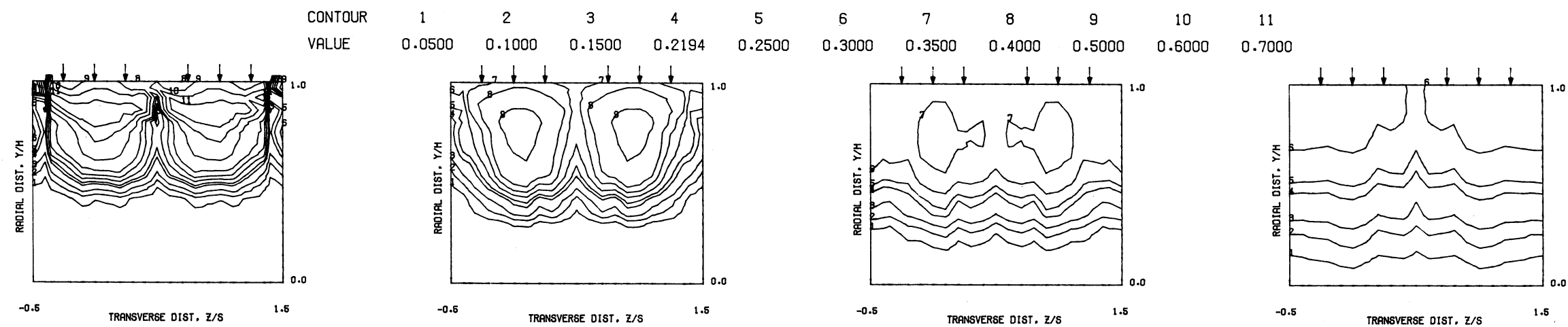
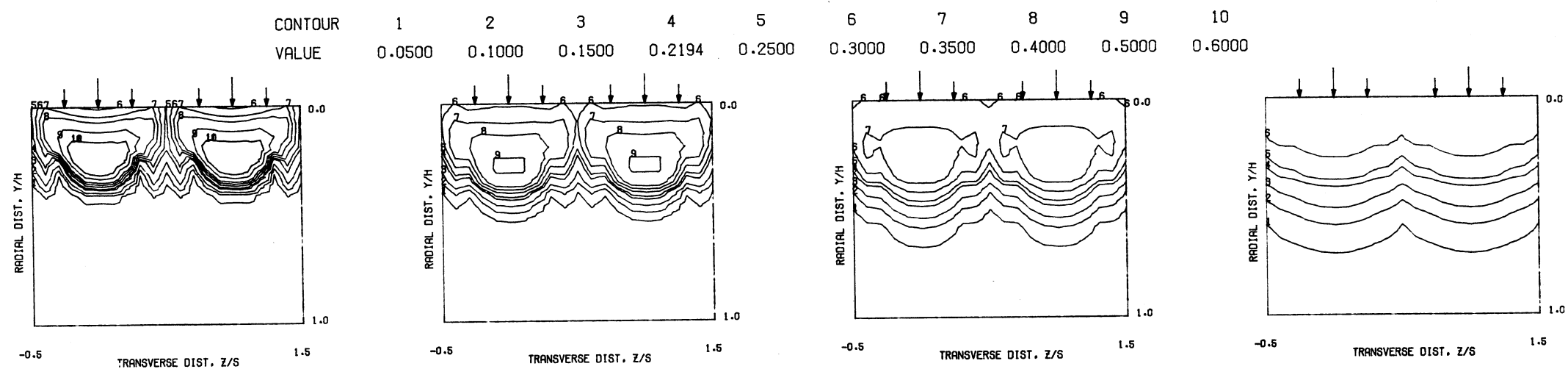
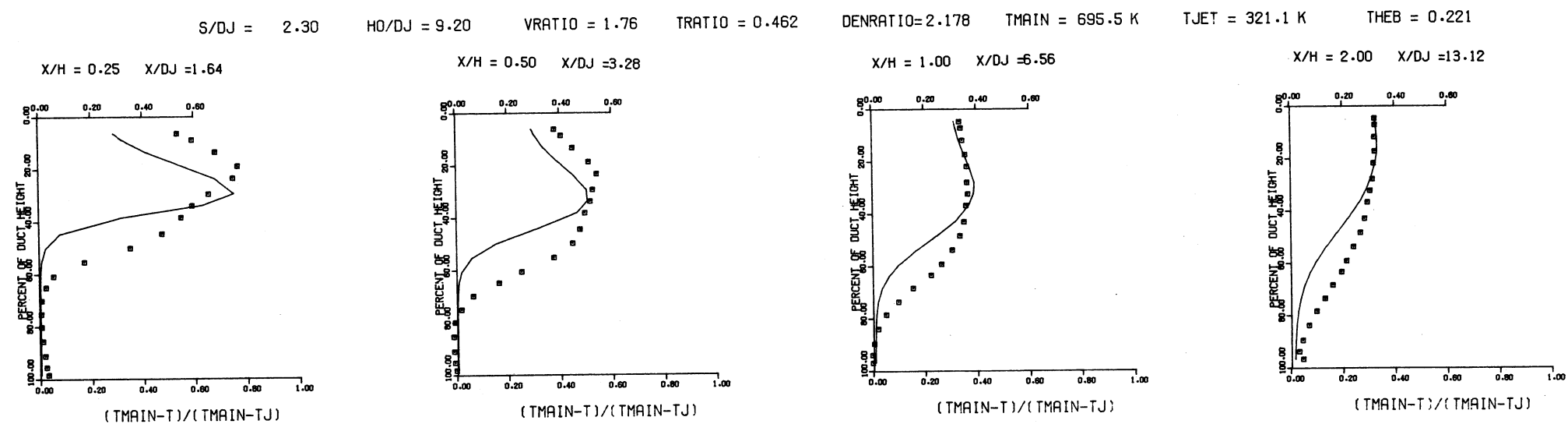


Figure 26. Measured Theta Distributions for Test No. 10.



PREDICTED THETA CONTOURS FOR TEST NO. 10, PLATE M5,  $J=6.72$ ,  $S/D=2.83$ ,  $H/D=5.66$

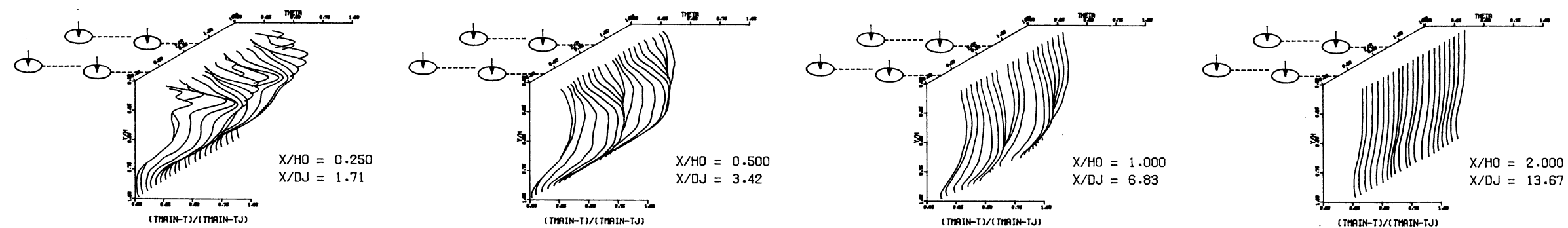


COMPARISON BETWEEN DATA AND CORRELATIONS FOR TEST NO 10, TEST SECTION I, PLATE M5    $J = 6.72$     $S/D = 2.83$     $H/D = 5.66$

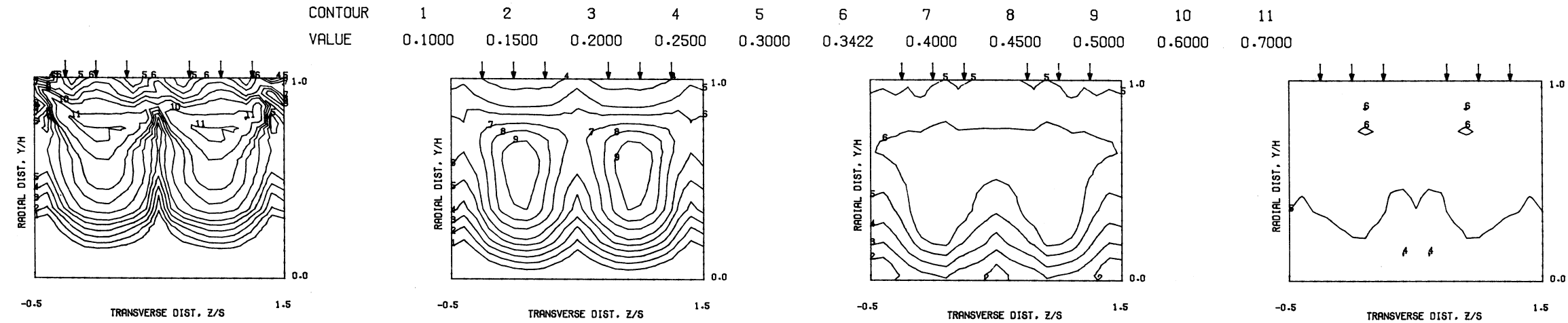
Figure 27. Predicted Theta  
Distributions for Test No. 10.



$S = 0.0508$  METERS     $S/DJ = 3.417$      $H_0/DJ = 6.835$      $V_{MAIN} = 17.3$  M/SEC     $V_{JET} = 60.2$  M/SEC     $T_{MAIN} = 677.2$  K     $T_{JET} = 313.5$  K     $THEB = 0.3422$      $BLORAT = 7.683$      $DENRATIO = 2.203$      $TRATIO = 0.463$

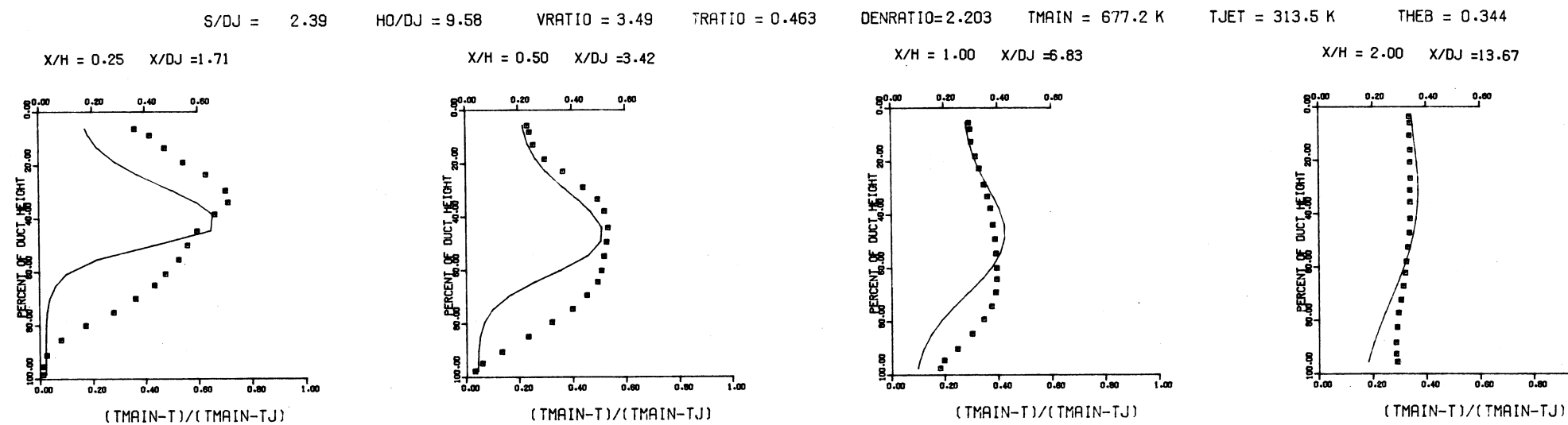
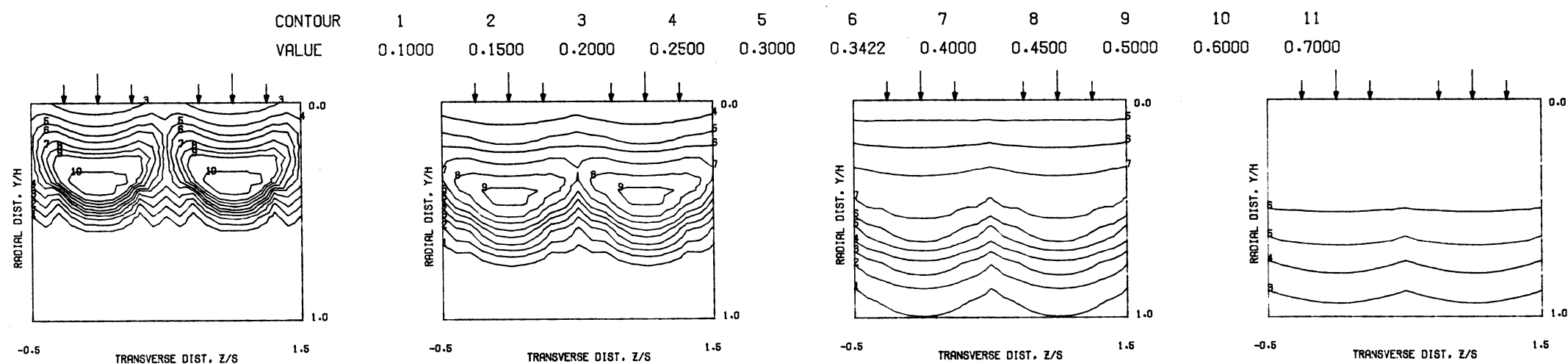


MEASURED THETA PROFILES FOR TEST NO. 11, TEST SECTION I, PLATE M5 ,  $J = 26.79$  ,  $S/D = 2.83$  ,  $H/D = 5.66$



MEASURED THETA CONTOURS FOR TEST NO 11, PLATE M5,  $J=26.79$ ,  $S/D=2.83$ ,  $H/D=5.66$

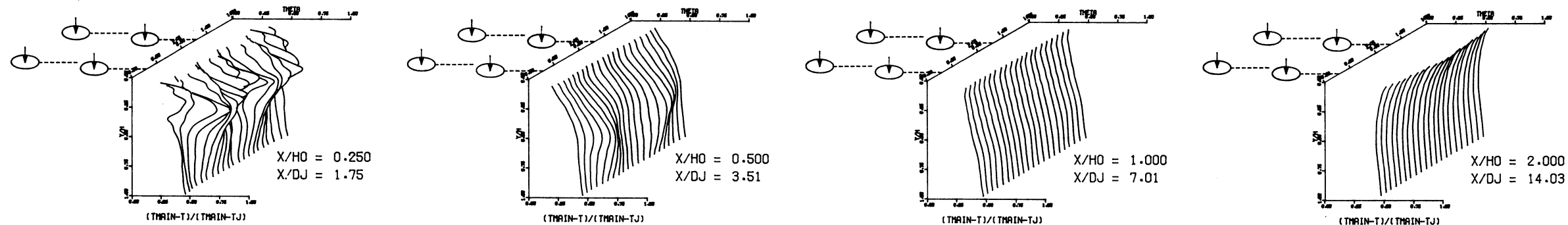
Figure 28. Measured Theta Distributions for Test No. 11.



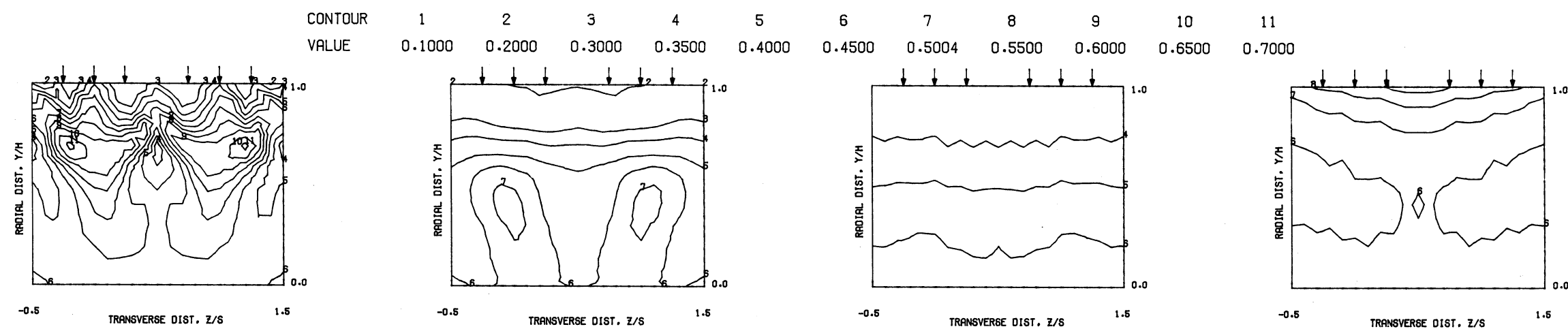
COMPARISON BETWEEN DATA AND CORRELATIONS FOR TEST NO 11, TEST SECTION I, PLATE M5 ,  $J = 26.79$  ,  $S/D = 2.83$  ,  $H/D = 5.66$

Figure 29. Predicted Theta Distributions for Test No. 11.

S = 0.0508 METERS S/DJ = 3.507 HO/DJ = 7.013 VMAIN = 16.4 M/SEC VJET = 113.3 M/SEC TMAIN = 645.0 K TJET = 313.7 K THEB = 0.5004 BLORAT= 15.364 DENRATIO= 2.221 TRATIO=0.486

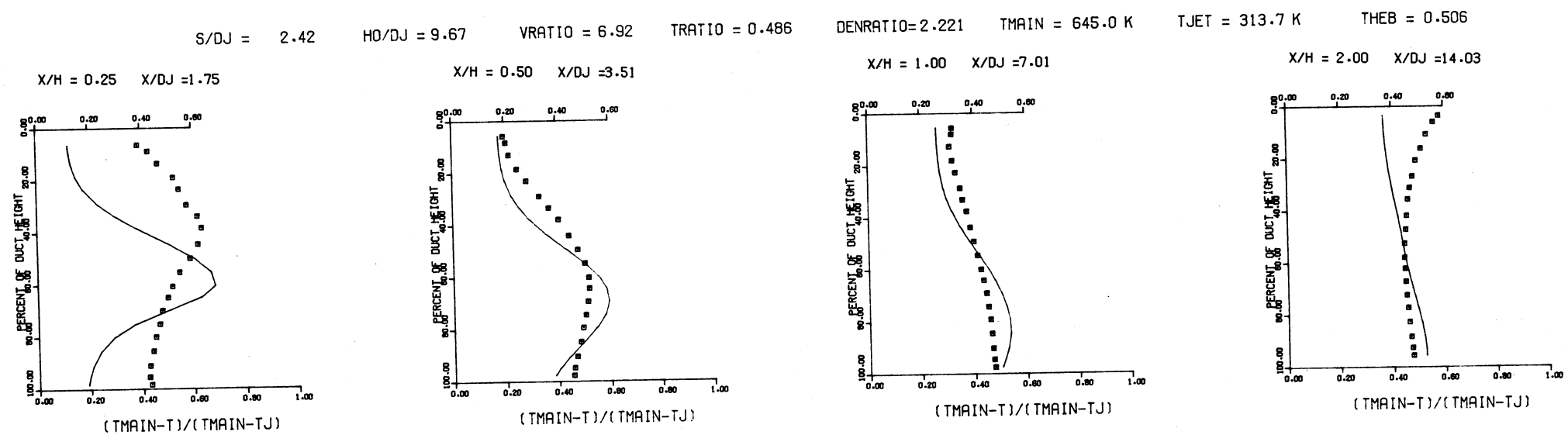
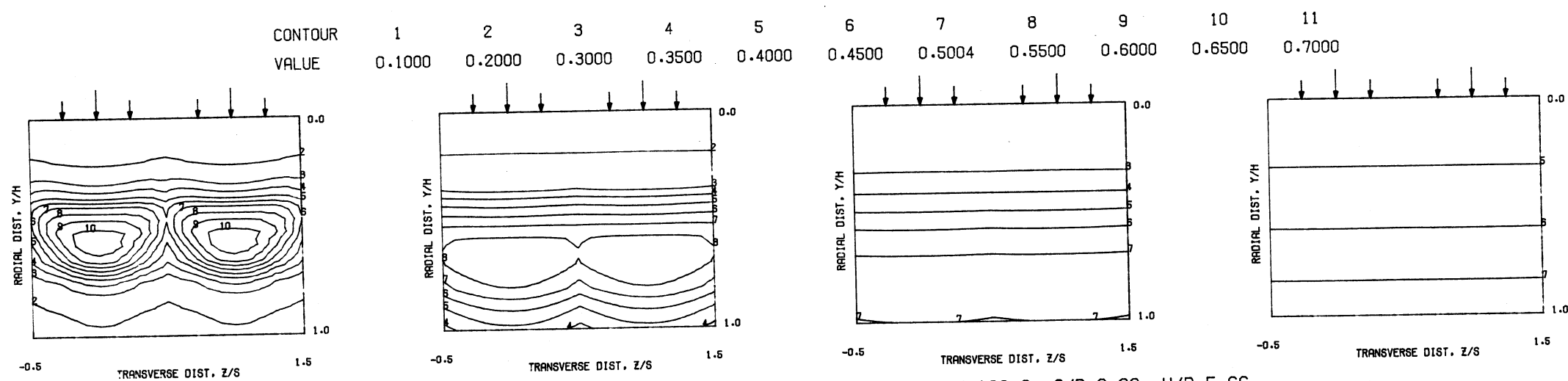


MEASURED THETA PROFILES FOR TEST NO. 12, TEST SECTION I, PLATE M5 , J = 106.27 , S/D = 2.83 , H/D = 5.66



MEASURED THETA CONTOURS FOR TEST NO 12, PLATE M5, J=106.3, S/D=2.83, H/D=5.66

Figure 30. Measured Theta Distributions for Test No. 12.



COMPARISON BETWEEN DATA AND CORRELATIONS FOR TEST NO 12, TEST SECTION I, PLATE M5,  $J = 106.27$ ,  $S/D = 2.83$ ,  $H/D = 5.66$

Figure 31. Predicted Theta Distributions for Test No. 12.

S = 0.0508 METERS S/DJ = 3.424 HO/DJ = 6.848 VMAIN = 17.0 M/SEC VJET = 58.5 M/SEC TMAIN = 672.0 K TJET = 310.1 K THEB = 0.2820 BLORAT= 7.605 DENRATIO= 2.208 TRATIO=0.461

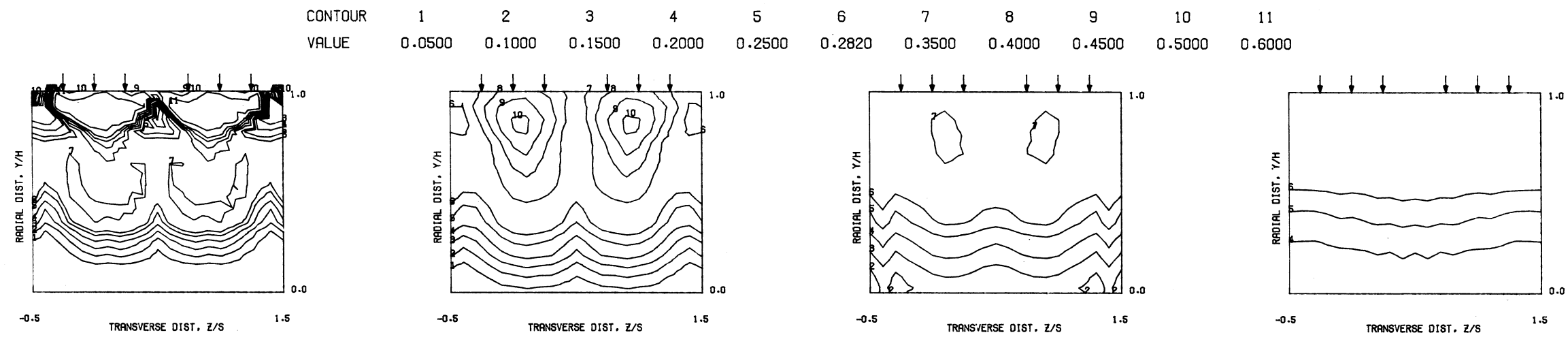
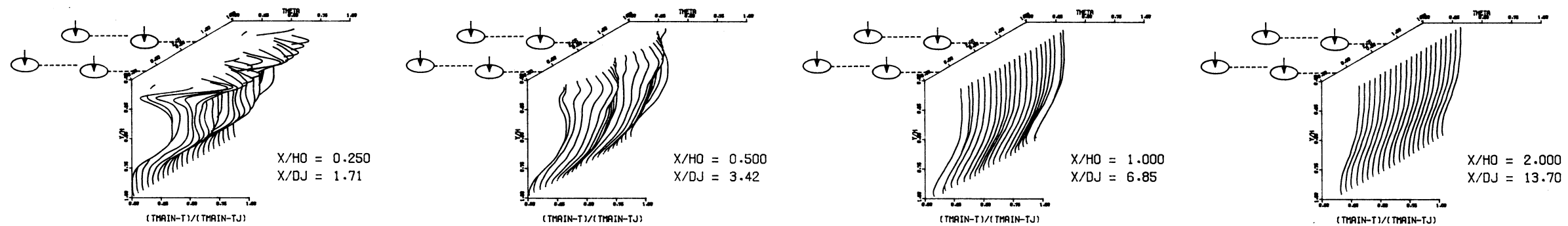
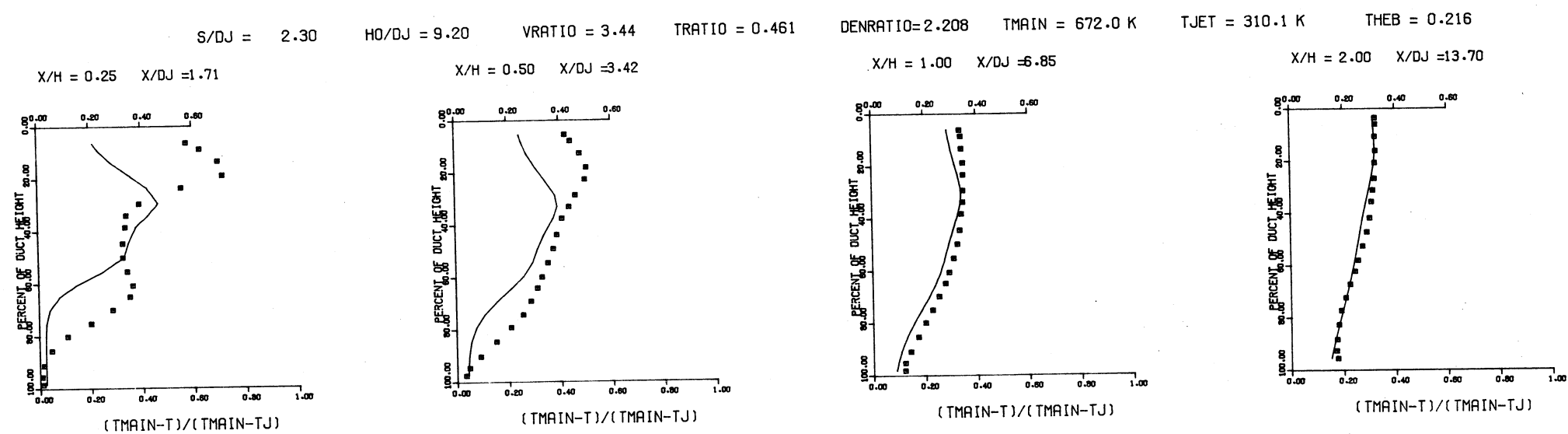
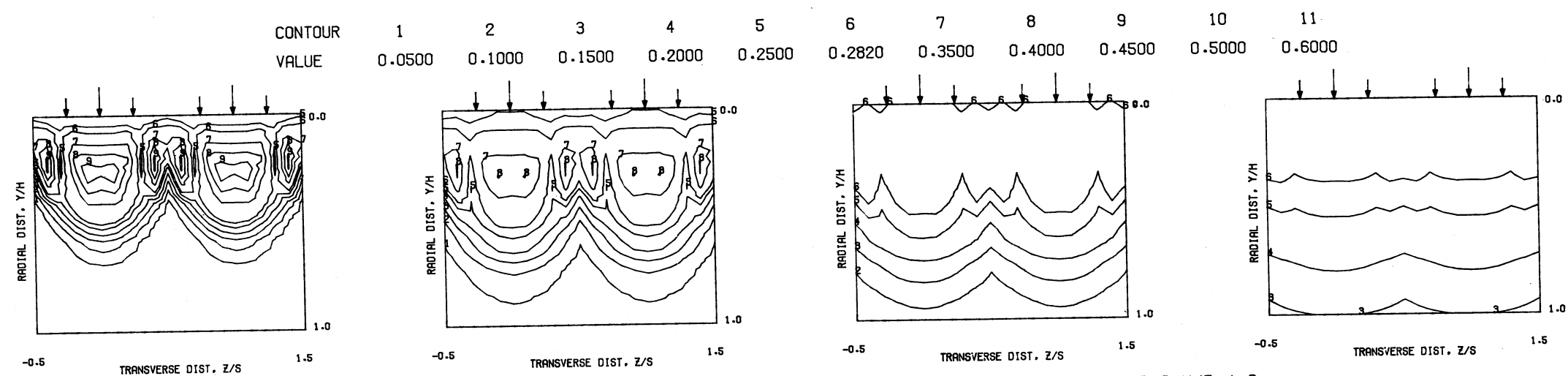


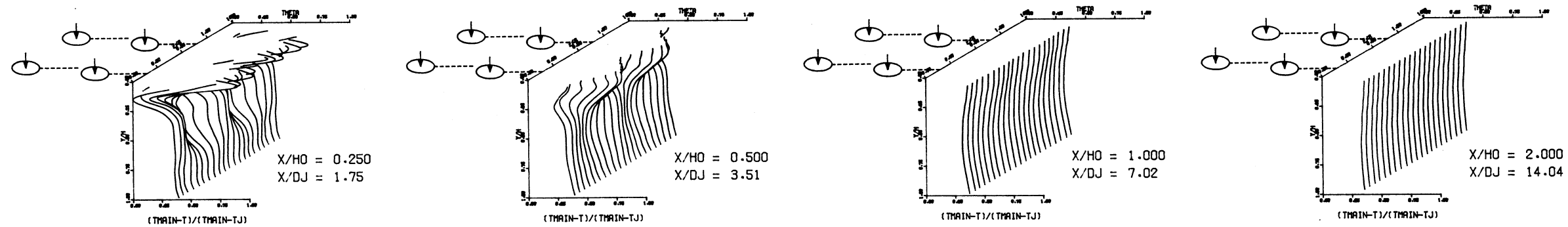
Figure 32. Measured Theta Distributions for Test No. 13.



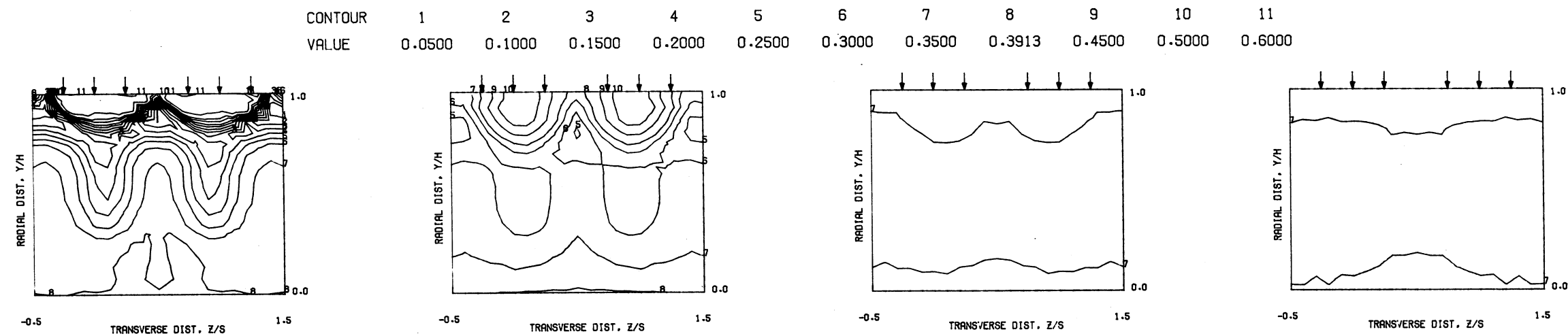
, J = 26.20 , S/D = 2.83 , H/D = 5.66

Figure 33. Predicted Theta Distributions for Test No. 13.

S = 0.0508 METERS S/DJ = 3.510 HO/DJ = 7.020 VMAIN = 16.8 M/SEC VJET = 113.0 M/SEC TMAIN = 666.3 K TJET = 304.5 K THEB = 0.3938 BLORAT= 15.834 DENRATIO= 2.353 TRATIO=0.457

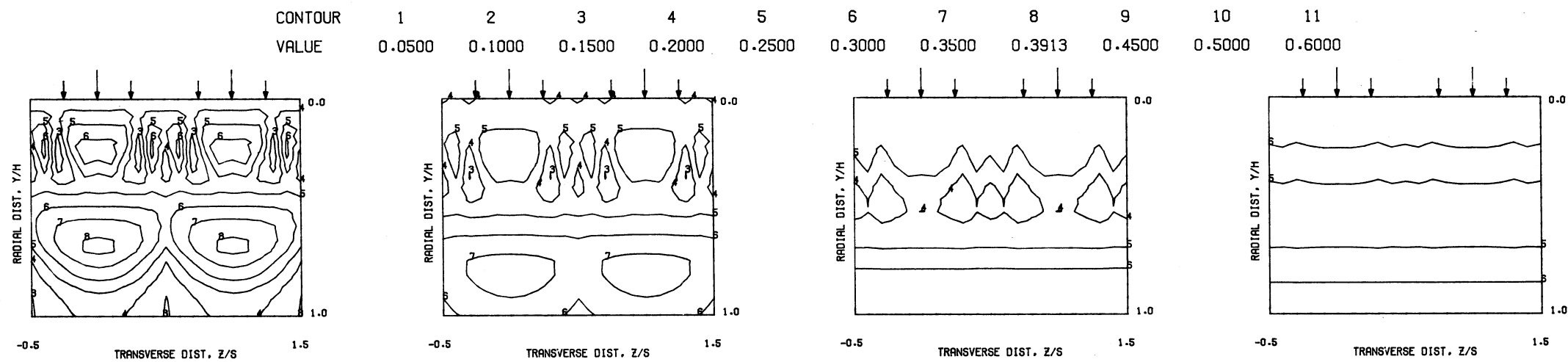


MEASURED THETA PROFILES FOR TEST NO 14, TEST SECTION I, PLATE M5(INL) , J = 106.54 , S/D = 2.83 , H/D = 5.66



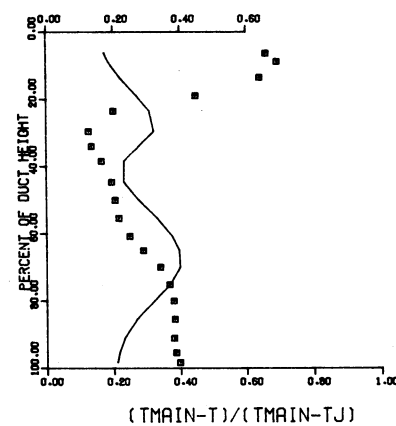
MEASURED THETA CONTOURS FOR TEST NO 14, PLATE M5, J1=106 , J2=6.5, S/D=2.83, H/D=5.66

Figure 34. Measured Theta Distributions for Test No. 14.

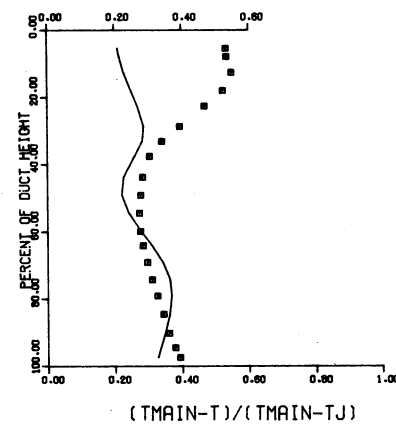


S/DJ = 2.30    HO/DJ = 9.20    VRATIO = 6.73    TRATIO = 0.457    DENRATIO=2.353    TMAIN = 666.3 K    TJET = 304.5 K    THEB = 0.214

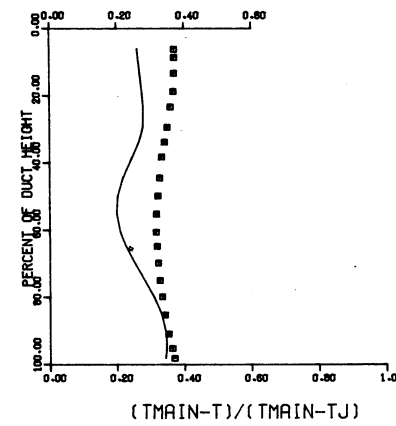
X/H = 0.25    X/DJ = 1.75



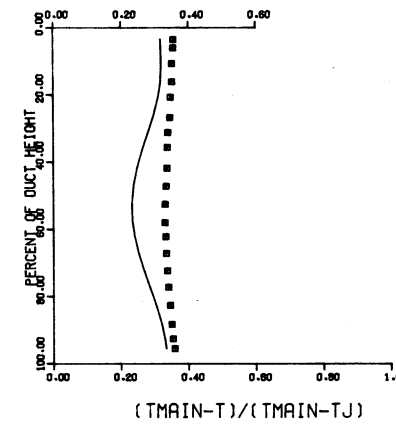
X/H = 0.50    X/DJ = 3.51



X/H = 1.00    X/DJ = 7.02



X/H = 2.00    X/DJ = 14.04



COMPARISON BETWEEN DATA AND CORRELATIONS FOR TEST NO 14, TEST SECTION I, PLATE M5, J = 106.54, S/D = 2.83, H/D = 5.66

Figure 35. Predicted Theta Distributions for Test No. 14.



S = 0.0508 METERS S/DJ = 3.510 HO/DJ = 7.020 VMAIN = 16.7 M/SEC VJET = 112.9 M/SEC TMAIN = 660.0 K TJET = 305.8 K THEB = 0.4318 BLORAT= 15.708 DENRATIO= 2.321 TRATIO=0.463

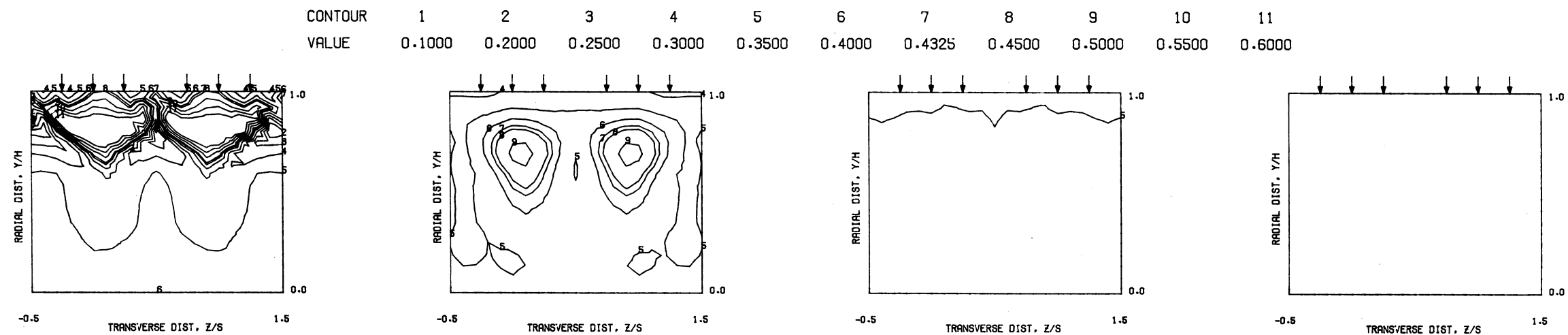
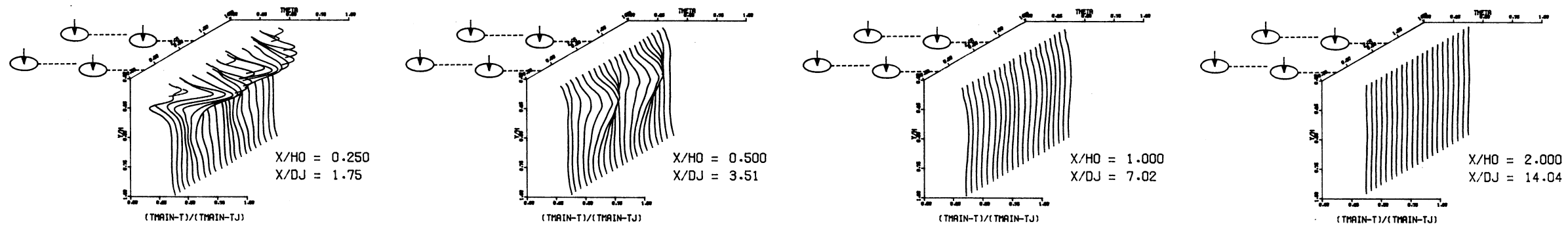
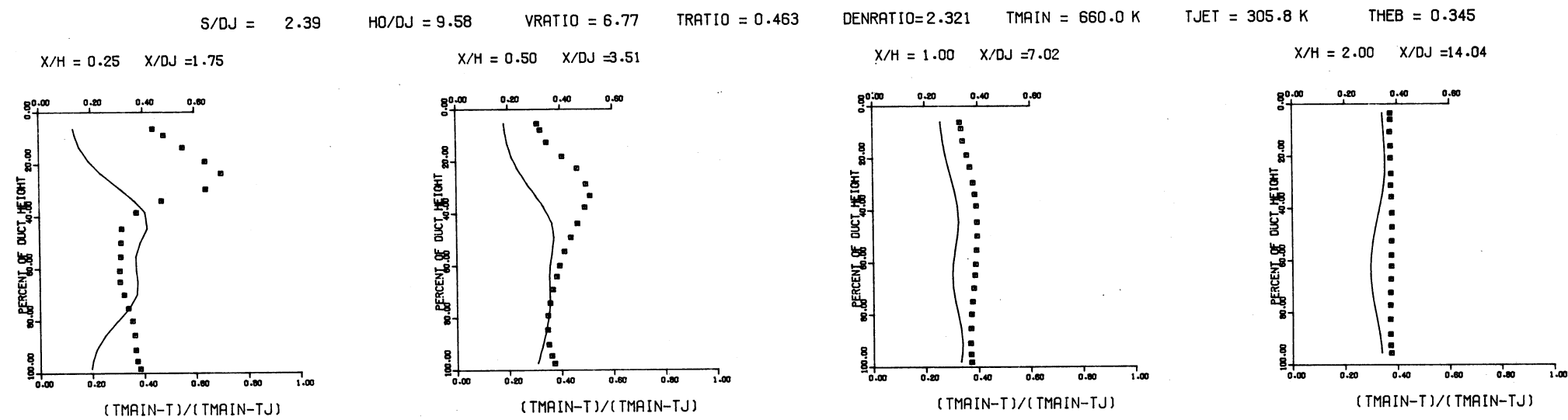
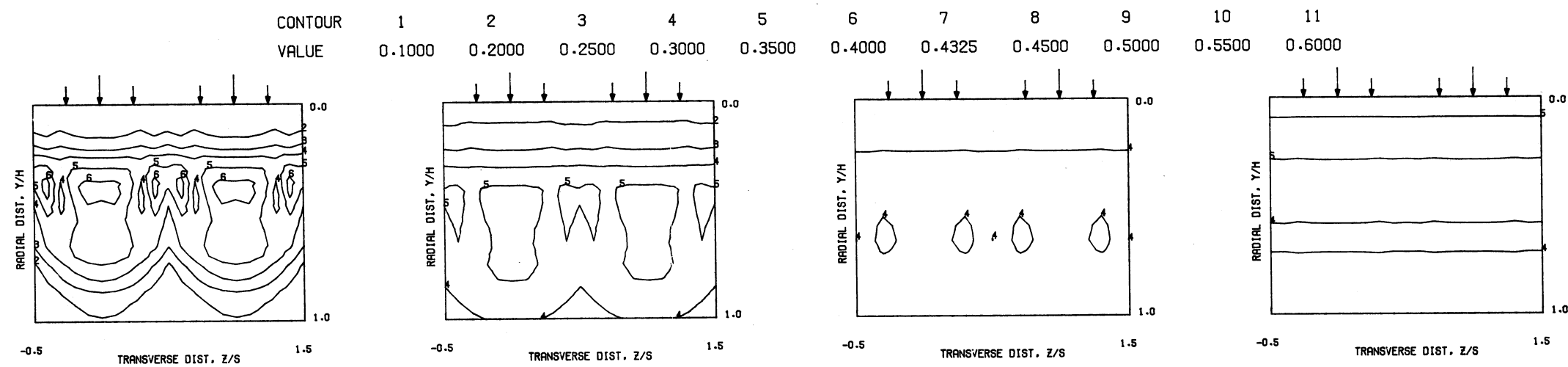


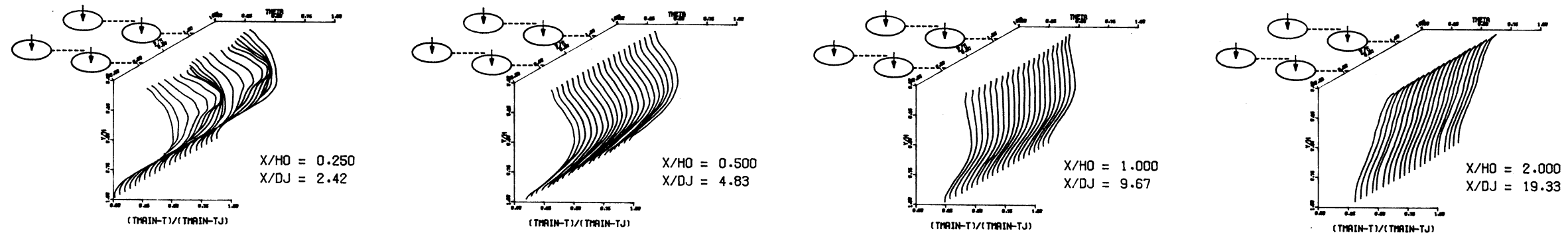
Figure 36. Measured Theta Distributions for Test No. 15.



COMPARISON BETWEEN DATA AND CORRELATIONS FOR TEST NO 15, TEST SECTION I, PLATE M5 , J = 106.29 , S/D = 2.83 , H/D = 5.66

Figure 37. Predicted Theta Distributions for Test No. 15.

S = 0.0254 METERS S/DJ = 2.416 H0/DJ = 9.666 VMAIN = 16.7 M/SEC VJET = 114.4 M/SEC TMAIN = 656.6 K TJET = 306.7 K THEB = 0.3939 BLORAT= 15.602 DENRATIO= 2.280 TRATIO= 0.467



, J = 106.78 , S/D = 2.00 , H/D = 8.00

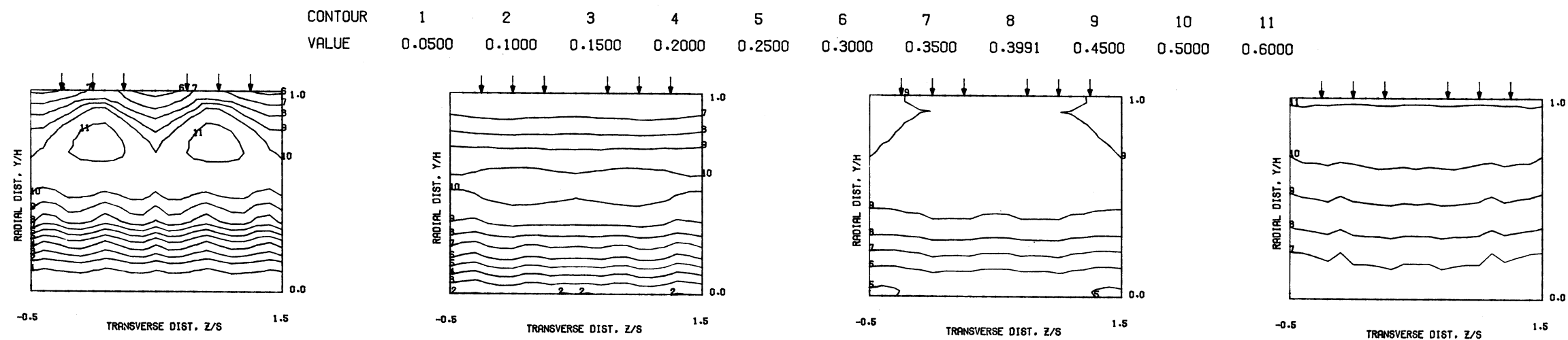
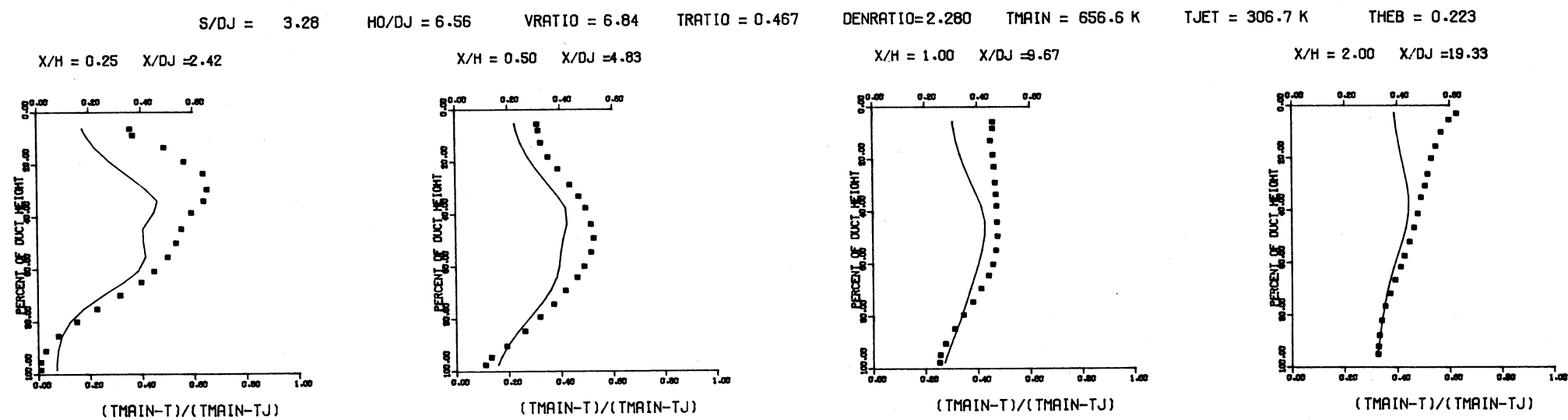
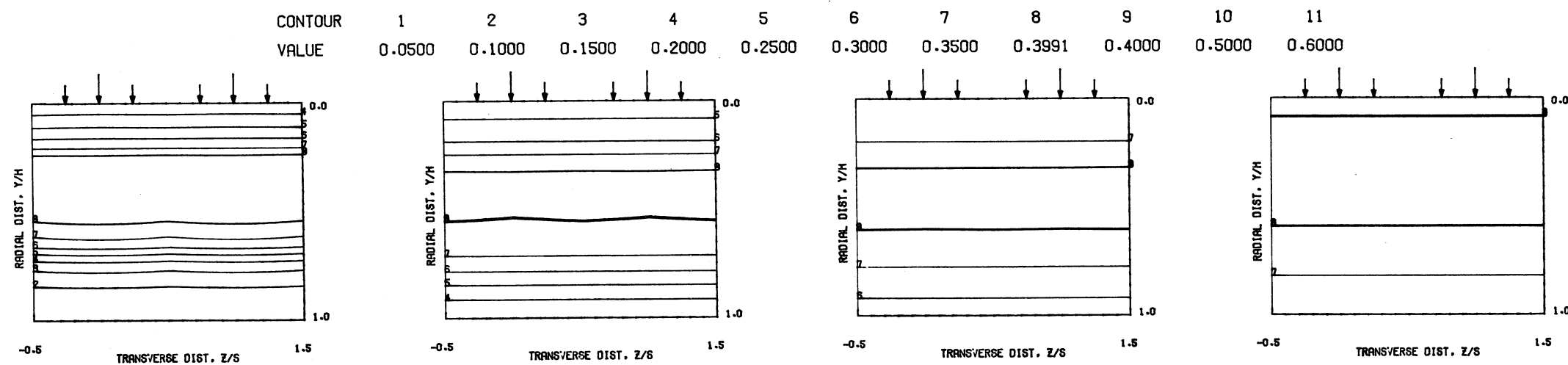


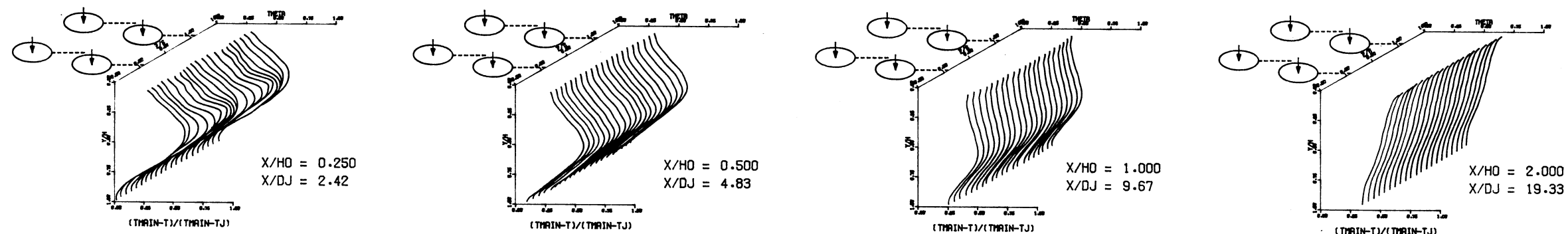
Figure 38. Measured Theta Distributions for Test No. 16.



COMPARISON BETWEEN DATA AND CORRELATIONS FOR TEST NO 16, TEST SECTION I, PLATE M6 , J = 106.78 , S/D =2.00 , H/D =8.00

Figure 39. Predicted Theta Distributions for Test No. 16.

S = 0.0254 METERS S/DJ = 2.416 HO/DJ = 9.666 VMAIN = 16.9 M/SEC VJET = 114.8 M/SEC TMAIN = 663.8 K TJET = 305.1 K THEB = 0.4409 BLORAT= 15.745 DENRATIO= 2.321 TRATIO= 0.460



, J = 106.83 , S/D = 2.00 , H/D = 8.00

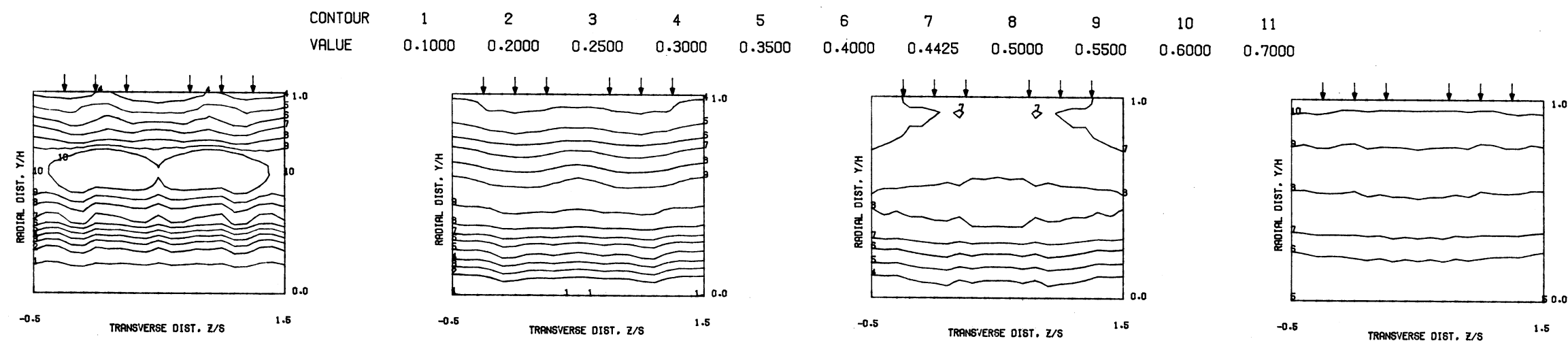
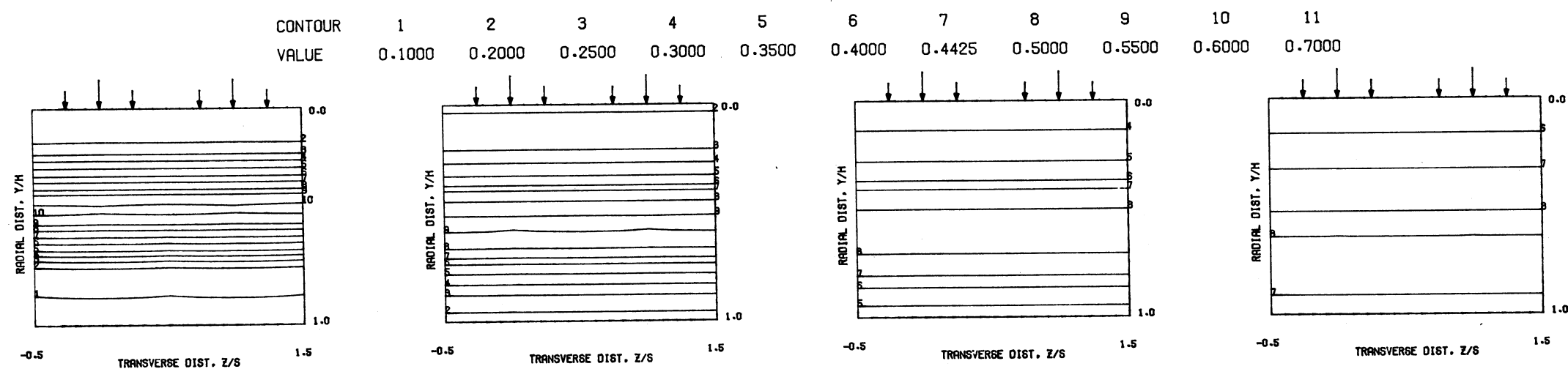
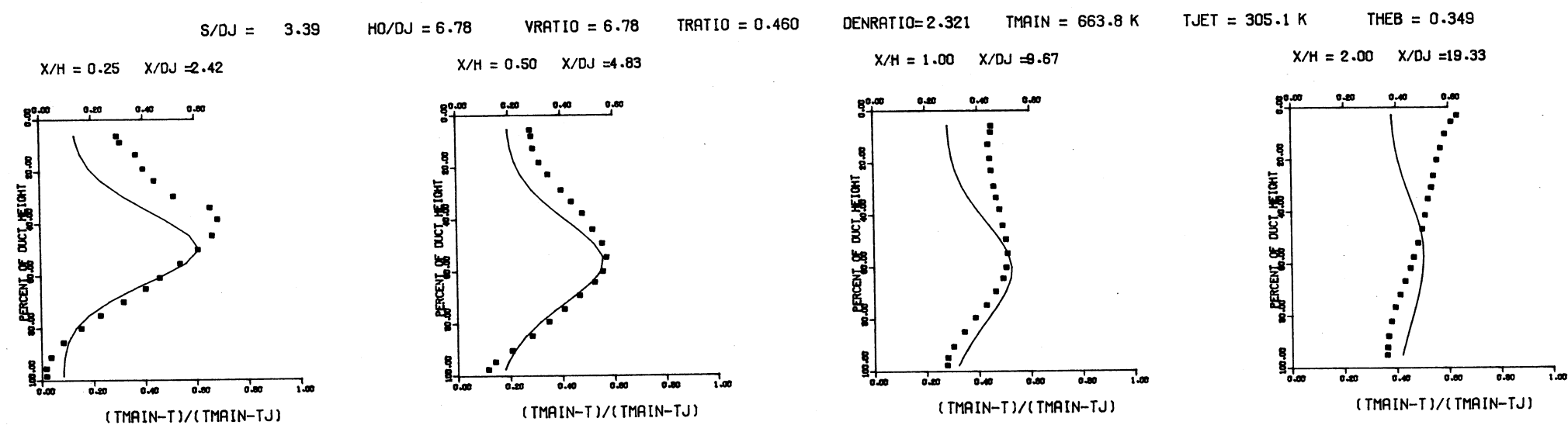


Figure 40. Measured Theta Distributions for Test No. 17.



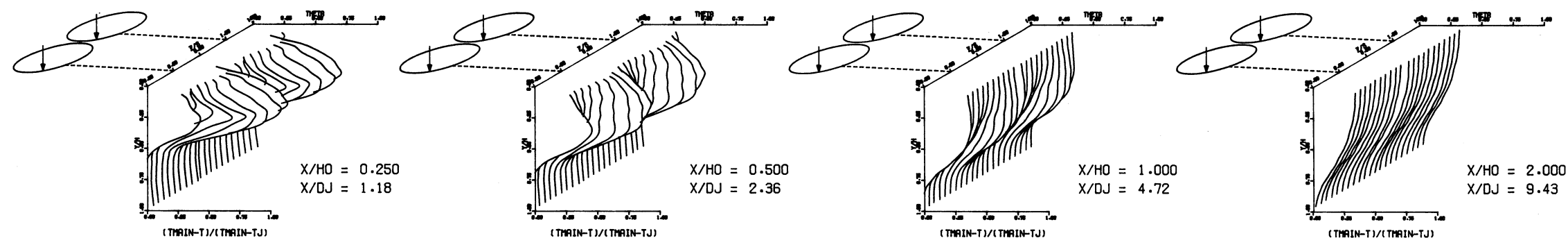
PREDICTED THETA CONTOURS FOR TEST NO 17, PLATE M6. J1=106. J2=26. S/D=2.0. H/D=8.0



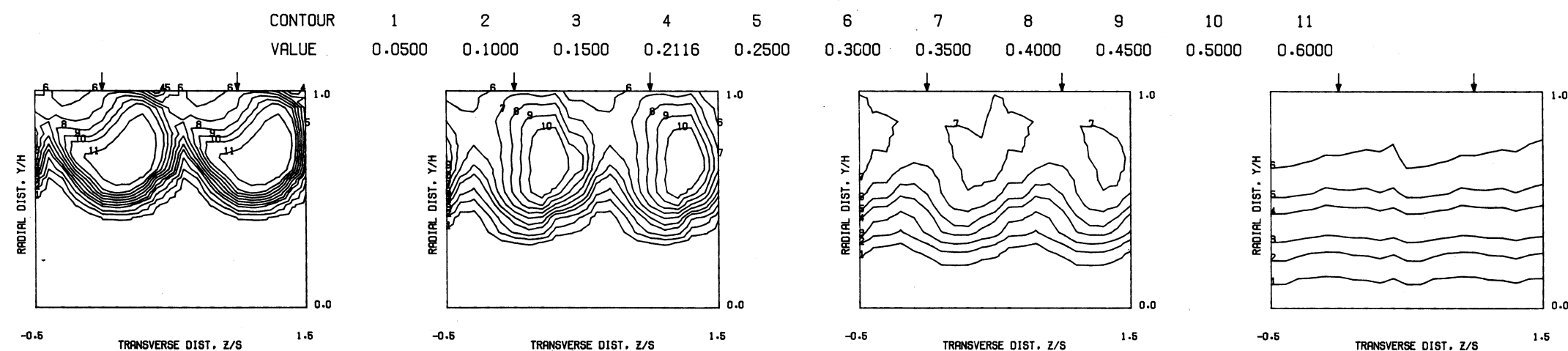
COMPARISON BETWEEN DATA AND CORRELATIONS FOR TEST NO 17, TEST SECTION I, PLATE M6    ,    J = 106.83    , S/D = 2.00    , H/D = 8.00

Figure 41. Predicted Theta Distributions for Test No. 17.

S = 0.0508 METERS S/DJ = 2.358 HO/DJ = 4.716 VMAIN = 17.4 M/SEC VJET = 30.4 M/SEC TMAIN = 684.2 K TJET = 316.3 K THEB = 0.2116 BLORAT= 3.800 DENRATIO= 2.173 TRATIO=0.462

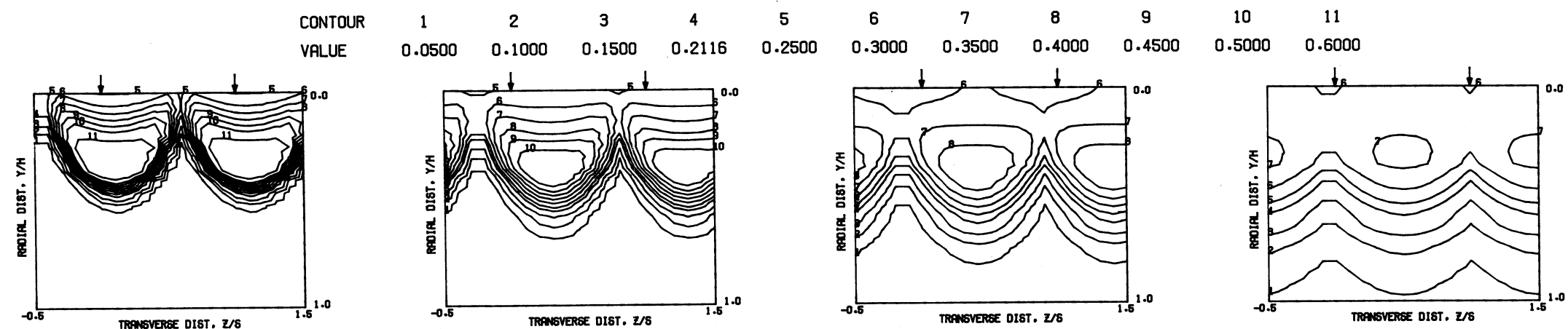


MEASURED THETA PROFILES FOR TEST NO 18, TEST SECTION I, 45-DEG SLOT , J = 6.64 , S/D = 2.00 , H/D = 4.00



MEASURED THETA CONTOURS FOR TEST NO 18, 45-DEG SLOT, J=6.64, S/D=2.00, H/D=4.00

Figure 42. Measured Theta Distributions for Test No. 18.



PREDICTED THETA CONTOURS FOR TEST NO 18, PLATE M-7, J=6.64, S/D=2.00, H/D=4.00

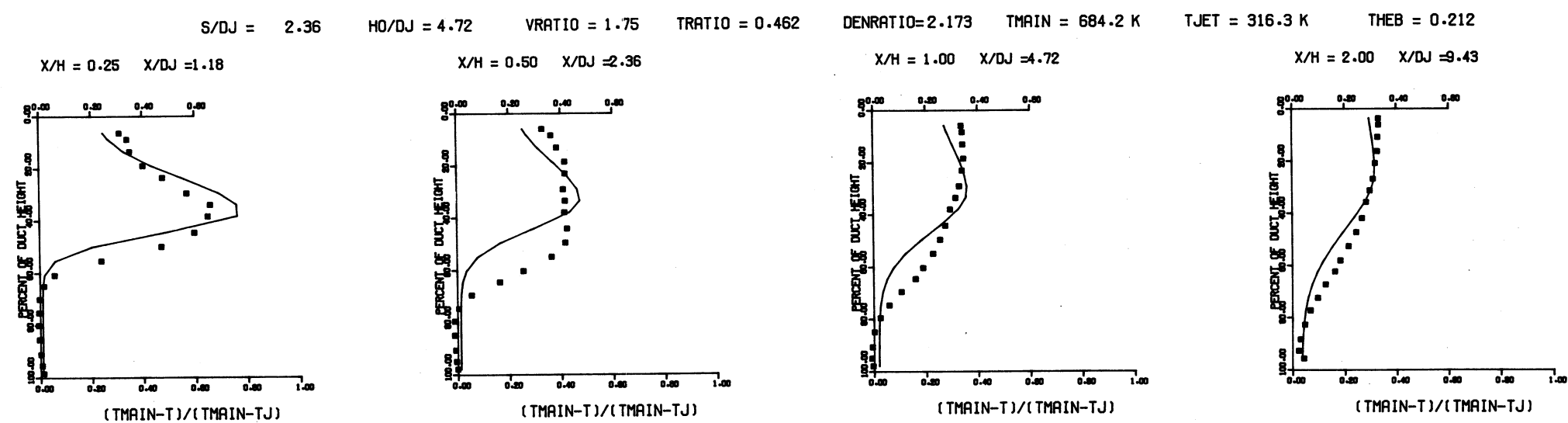
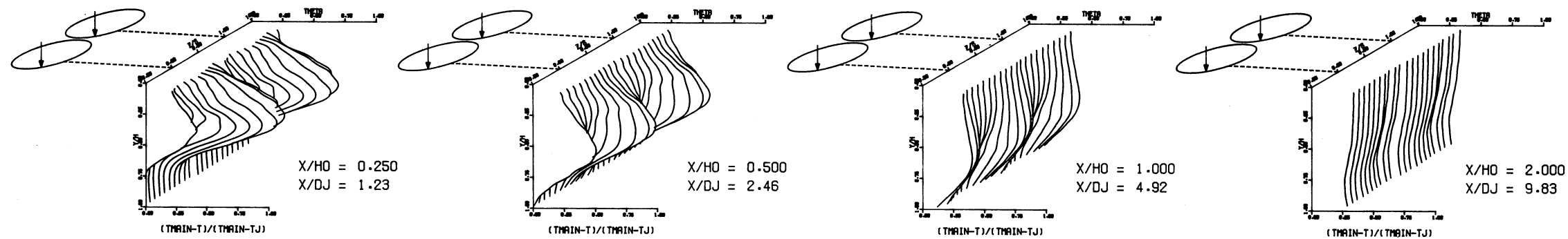


Figure 43. Predicted Theta Distributions for Test No. 18.

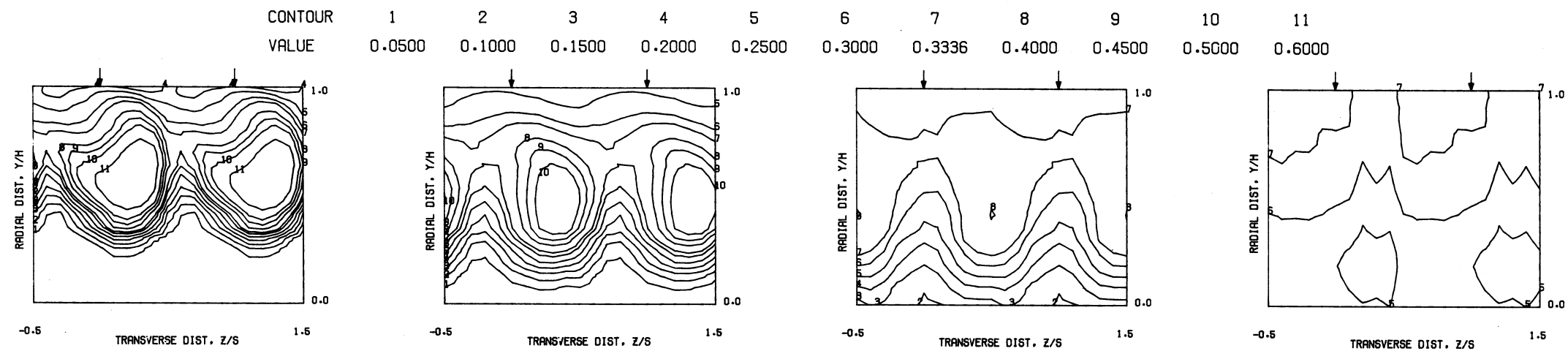
COMPARISON BETWEEN DATA AND CORRELATIONS FOR TEST TEST NO 18, 45 DEG SLOTS, PHASE III J = 6.64 , S/D =2.00 , H/D =4.00 110



S = 0.0508 METERS S/DJ = 2.458 HO/DJ = 4.916 VMAIN = 17.2 M/SEC VJET = 60.5 M/SEC TMAIN = 675.5 K TJET = 314.5 K THEB = 0.3336 BLORAT= 7.702 DENRATIO= 2.186 TRATIO= 0.466

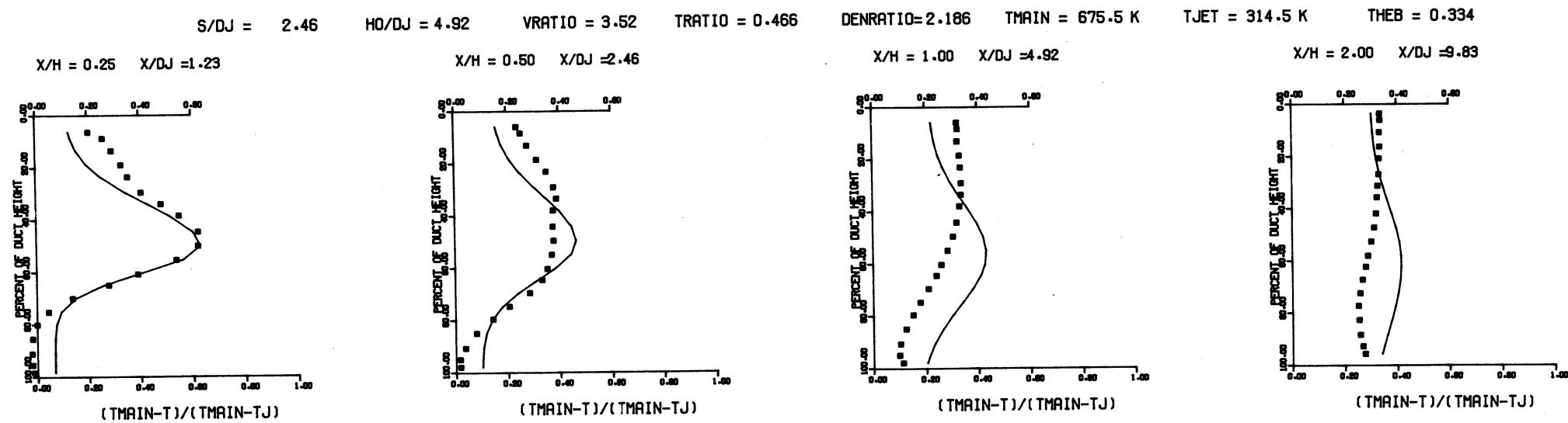
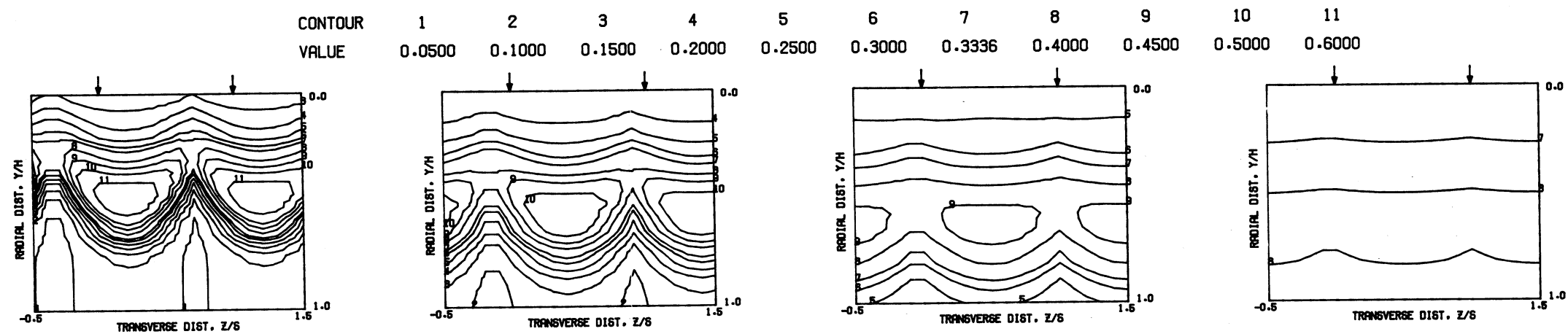


MEASURED THETA PROFILES FOR TEST NO 19, TEST SECTION I, 45-DEG SLOT , J = 27.13 , S/D = 2.00 , H/D = 4.00



MEASURED THETA CONTOURS FOR TEST NO 19, 45-DEG SLOT, J=27.13, S/D=2.00, H/D=4.00

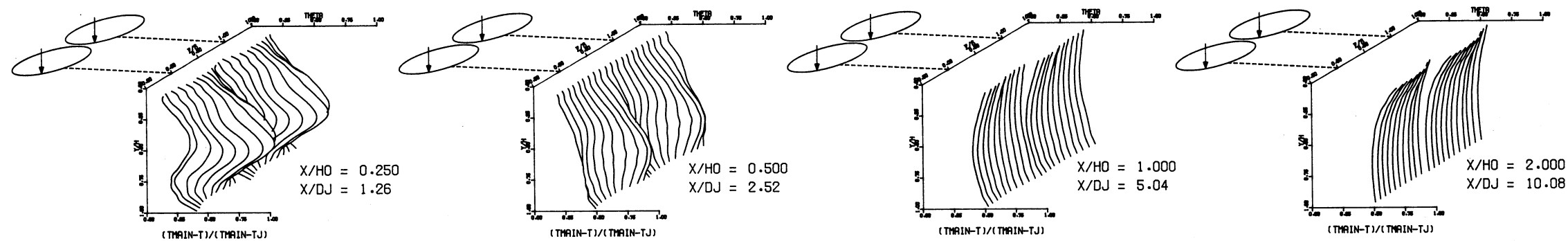
Figure 44. Measured Theta Distributions for Test No. 19.



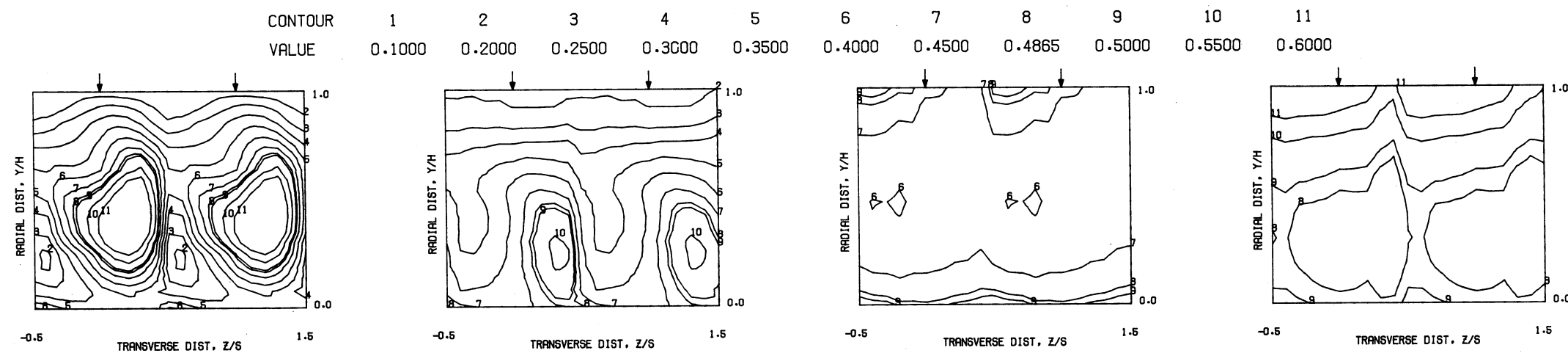
J = 27.13 , S/D = 2.00 , H/D = 4.00

Figure 45. Predicted Theta Distributions for Test No. 19.

S = 0.0508 METERS S/DJ = 2.519 H0/DJ = 5.039 VMAIN = 16.2 M/SEC VJET = 112.0 M/SEC TMAIN = 637.4 K TJET = 307.8 K THEB = 0.4865 BLORAT= 15.314 DENRATIO= 2.209 TRATIO= 0.483

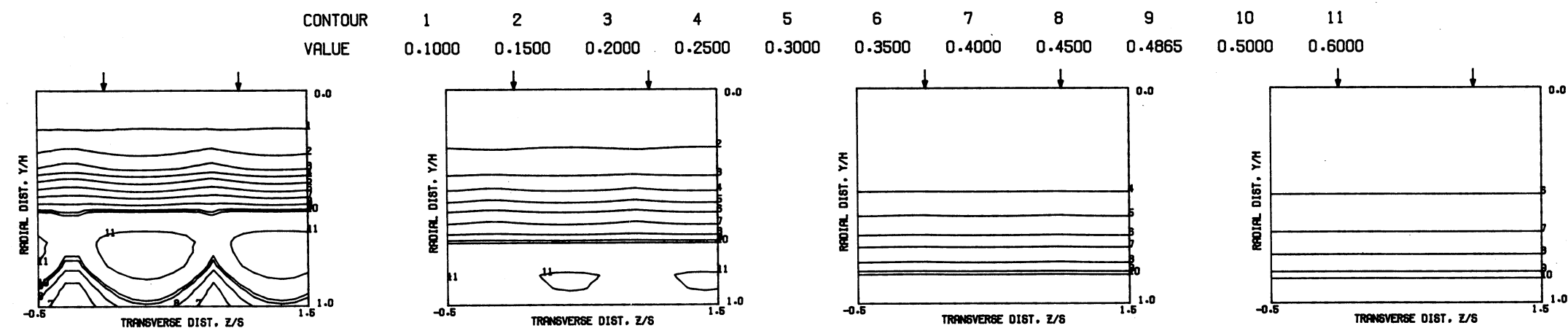


MEASURED THETA PROFILES FOR TEST NO 20, TEST SECTION I, 45-DEG SLOT, J = 106.18, S/D = 2.00, H/D = 4.00

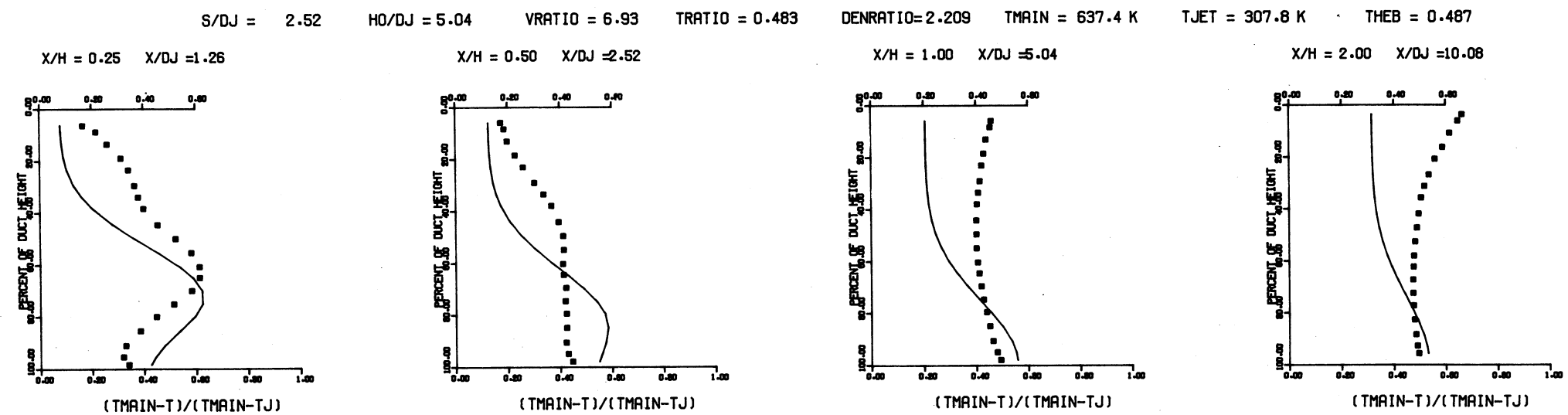


MEASURED THETA CONTOURS FOR TEST NO 20, 45-DEG SLOT, J=106.18, S/D=2.00, H/D=4.00

Figure 46. Measured Theta Distributions for Test No. 20.



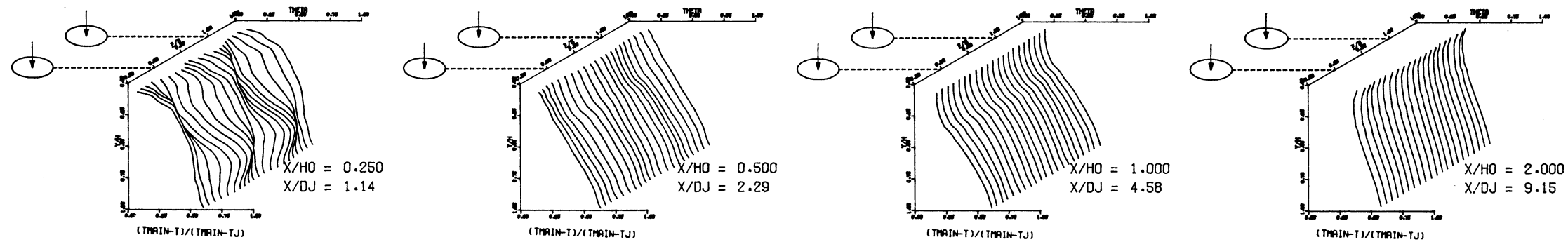
PREDICTED THETA CONTOURS FOR TEST NO 20, PLATE M-7, J=106.18, S/D=2.00, H/D=4.00



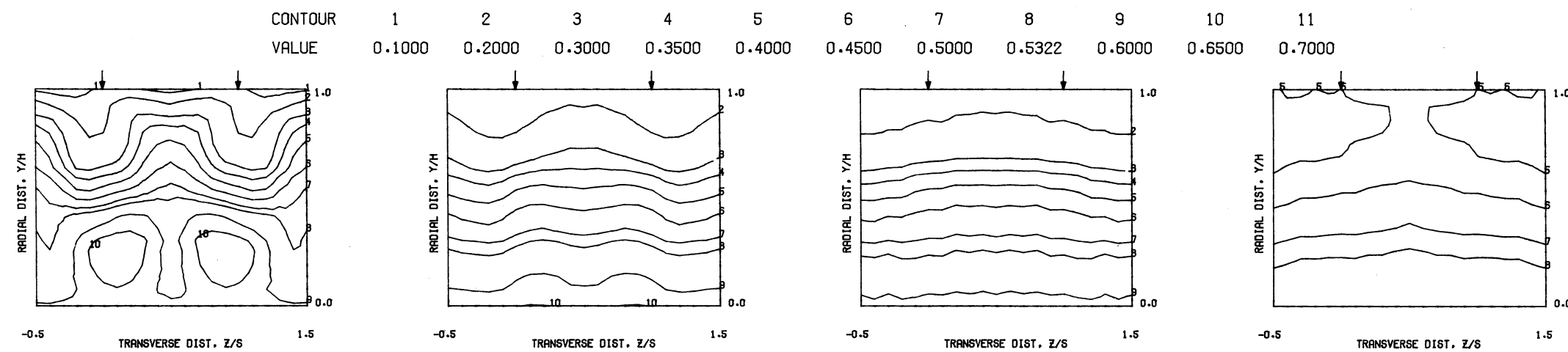
COMPARISON BETWEEN DATA AND CORRELATIONS FOR TEST TEST NO 20, 45 DEG SLOTS, PHASE III    J = 106.18 , S/D =2.00 , H/D =4.00

Figure 47. Predicted Theta Distributions for Test No. 20.

S = 0.0508 METERS S/DJ = 2.288 HO/DJ = 4.576 VMAIN = 15.3 M/SEC VJET = 104.3 M/SEC TMAIN = 629.1 K TJET = 307.0 K THEB = 0.5322 BLORAT= 15.170 DENRATIO= 2.230 TRATIO= 0.488

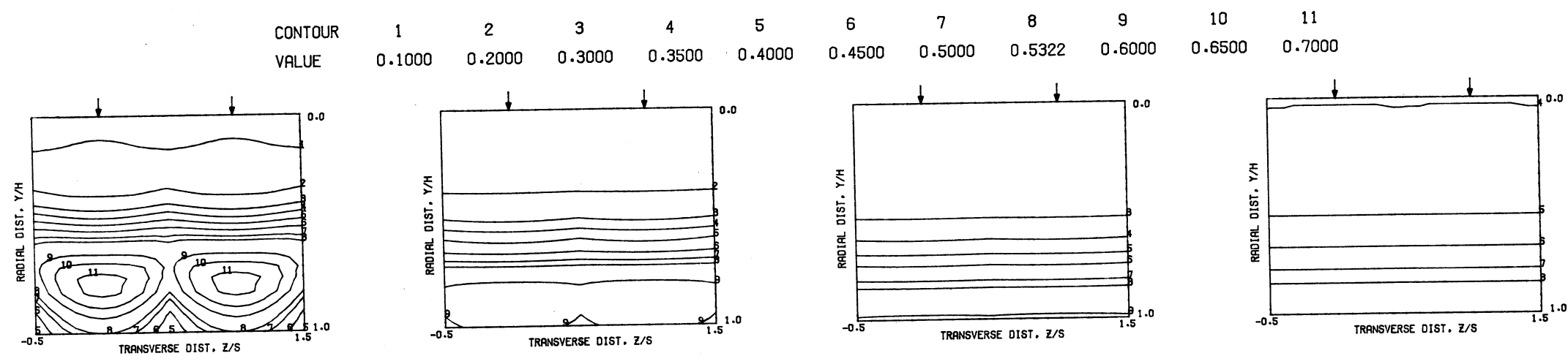


MEASURED THETA PROFILES FOR TEST NO 21, TEST SECTION I, TM=CONST, J = 103.19, S/D = 2.00, H/D = 4.00

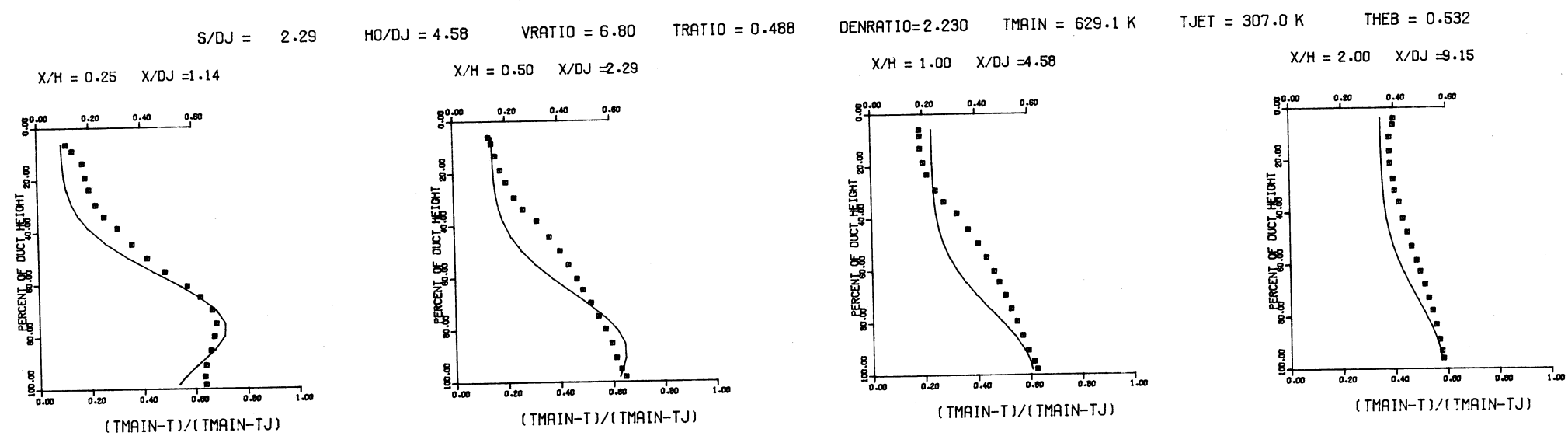


MEASURED THETA CONTOURS FOR TEST NO 21, TM=CONST, J=103.2, S/D=2.00, H/D=4.00

Figure 48. Measured Theta Distributions for Test No. 21.



PREDICTED THETA CONTOURS FOR TEST NO 21,  $T_M=CONST$ ,  $J=103.2$ ,  $S/D=2.00$ ,  $H/D=4.00$

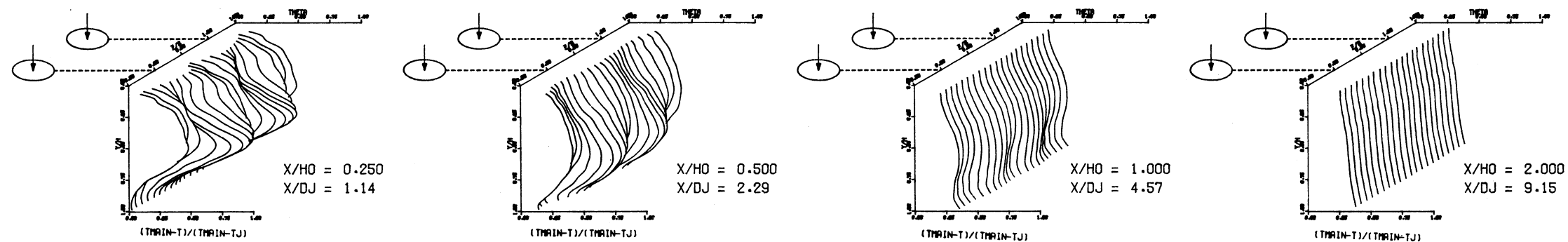


COMPARISON BETWEEN DATA AND CORRELATIONS FOR TEST NO 21, TEST SECTION I,  $T_M=CONST$ .

$J = 103.19$ ,  $S/D = 2.00$ ,  $H/D = 4.00$

Figure 49. Predicted Theta Distributions for Test No. 21.

S = 0.0508 METERS S/DJ = 2.286 HO/DJ = 4.573 VMAIN = 16.9 M/SEC VJET = 58.6 M/SEC TMAIN = 668.5 K TJET = 312.7 K THEB = 0.3626 BLORAT= 7.572 DENRATIO= 2.185 TRATIO= 0.468



, J = 26.24 , S/D = 2.00 , H/D = 4.00

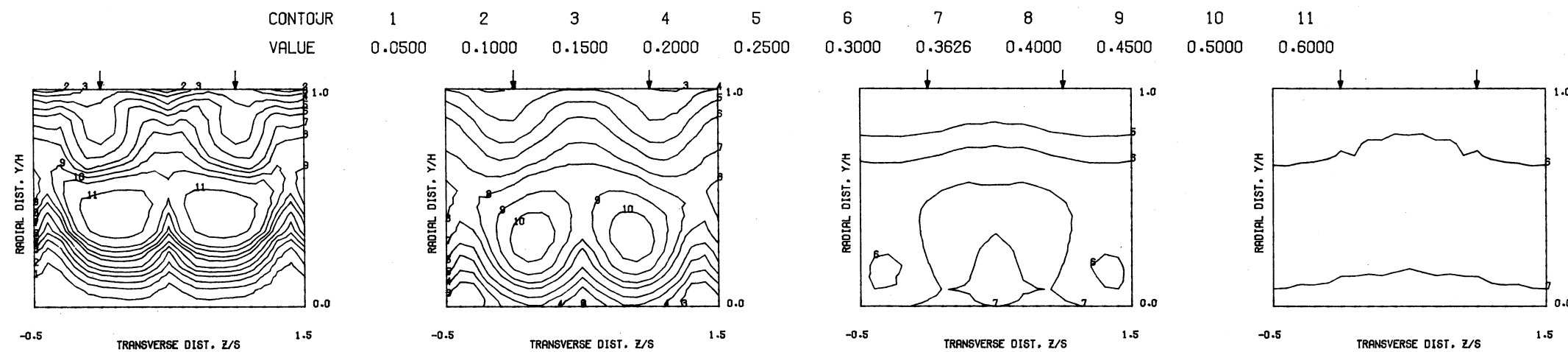
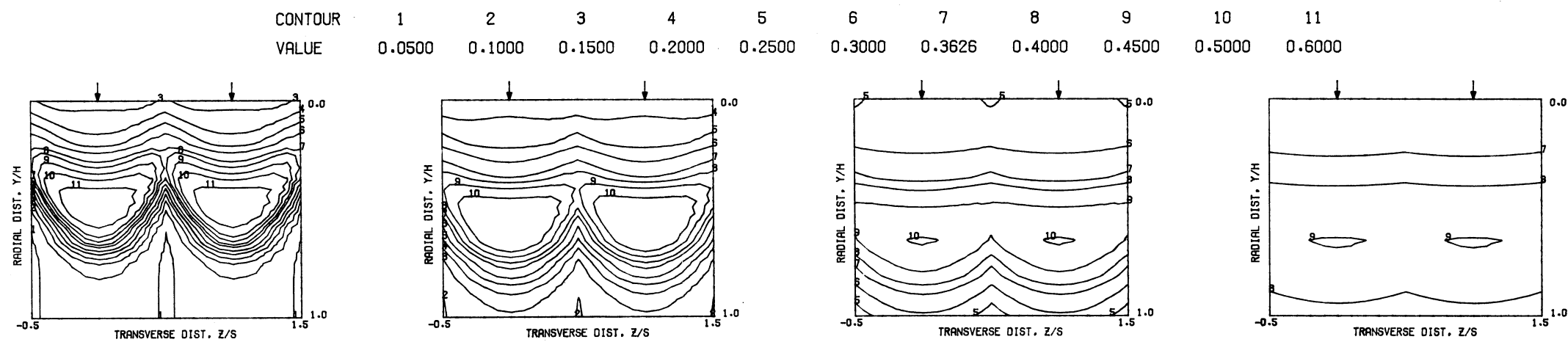
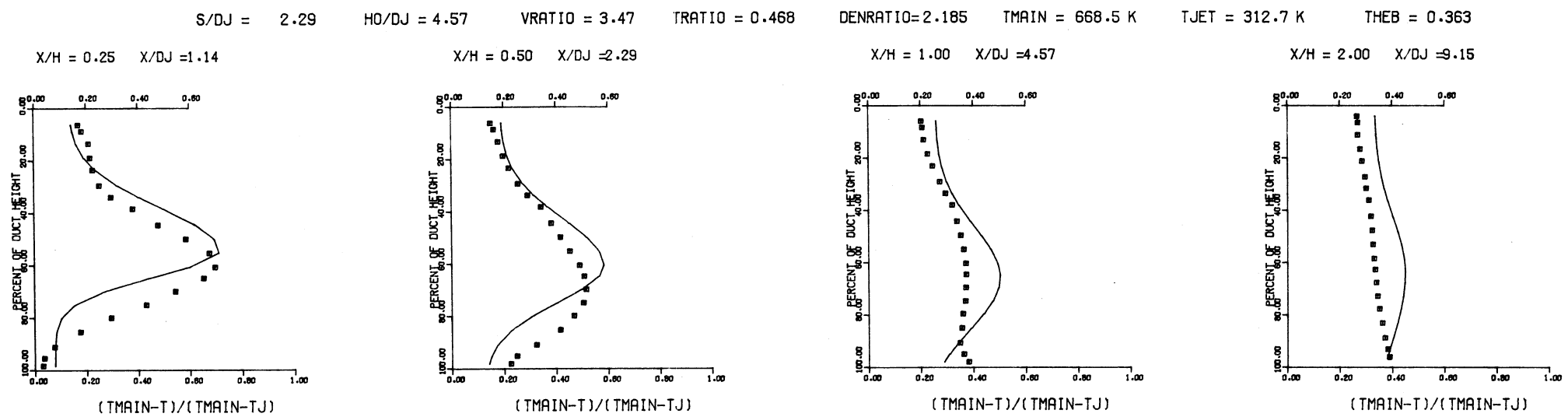


Figure 50. Measured Theta Distributions for Test No. 22.



PREDICTED THETA CONTOURS FOR TEST NO 22,  $T_M=CONST$ ,  $J=26.24$ ,  $S/D=2.00$ ,  $H/D=4.00$



COMPARISON BETWEEN DATA AND CORRELATIONS FOR TEST NO 22, TEST SECTION I,  $T_M=CONST$ ,

$J = 26.24$ ,  $S/D = 2.00$ ,  $H/D = 4.00$

Figure 51. Predicted Theta Distributions for Test No. 22.



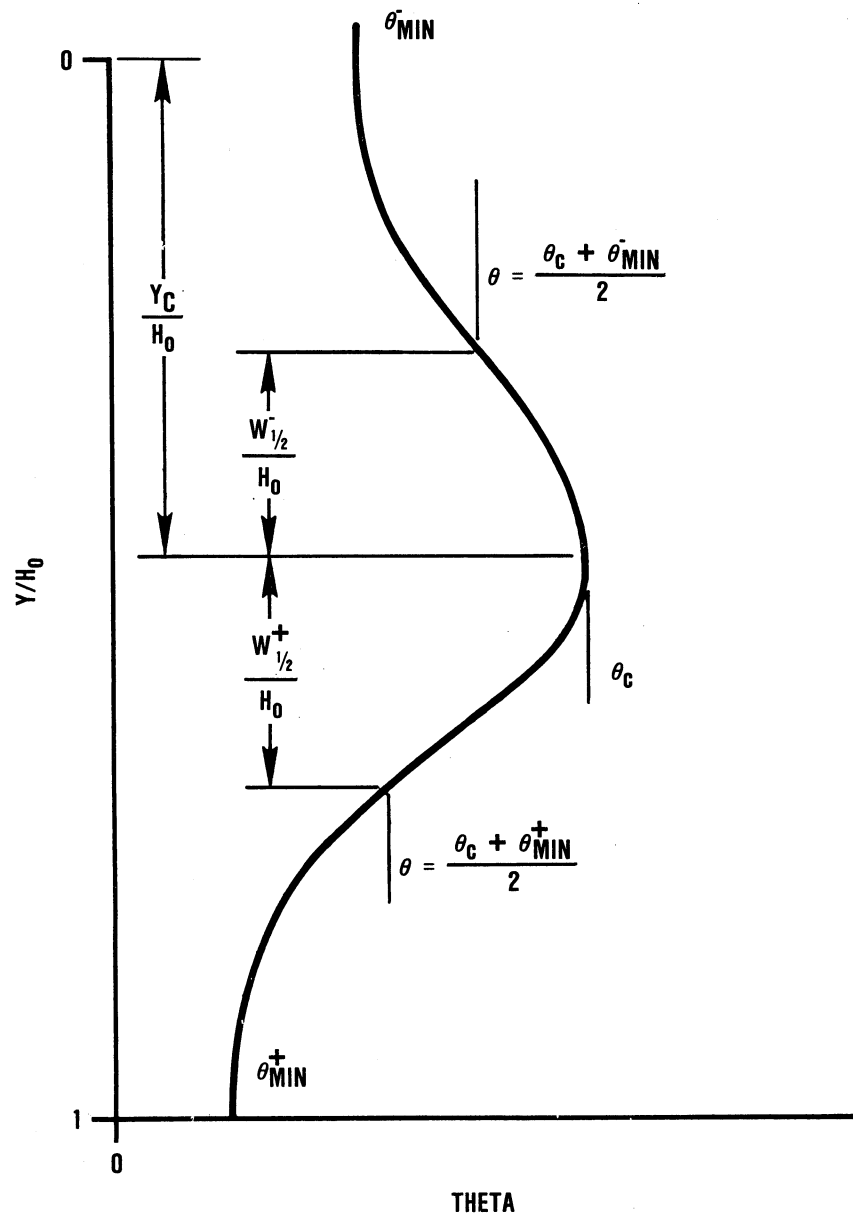


Figure 52. Schematic of Typical Vertical Theta Profile.

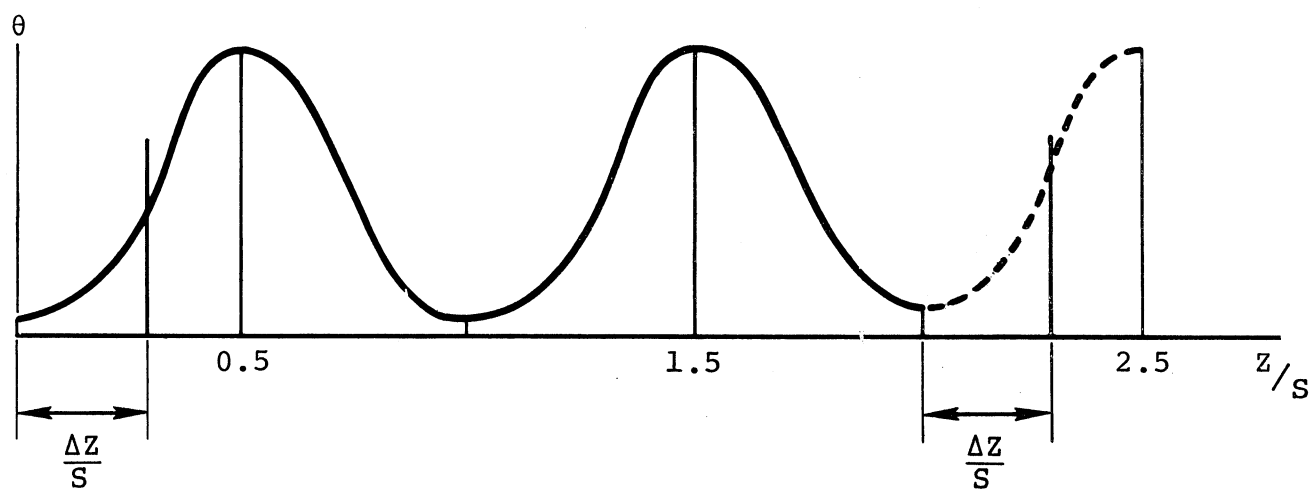


Figure 53. Theta Distributions Obtained from NASA/ Garrett Correlations for Angled Slots.

## APPENDIX A

### OPERATING CONDITIONS OF TESTS PERFORMED IN PHASES I AND II

During the review and evaluation of the test data obtained in the Dilution Jet Mixing Program, Phases I and II, it was discovered that the momentum flux values quoted earlier were incorrect. The correct values of momentum flux ratio, discharge coefficients and all relevant test conditions are provided in Tables A-1 through A-8.



TABLE A-1. PHASE I, SERIES 1 TEST CONFIGURATIONS AND FLOW CONDITIONS.

PHASE I SERIES 1 TESTS

Test No.	Test Section	Orifice Dia (CM)	$\frac{S}{D}$	$\frac{H_0}{D}$	Mainstream			Dilution Jet				Momentum Flux Ratio (J)	Density Ratio (Denratio)	Equilibrium Theta (Theb)	Regions of Measurement	
					Mass Flow Rate (KG/S)	Temp (Tmain) (K)	Velocity (Vmain) (M/S)	Mass Flow Rate (KG/S)	Temp (Tjet) (K)	Velocity (Vjet) (M/S)	$C_{DJ}$				Axial Direction (X/H <sub>0</sub> )	Transverse Direction (Z/S)
1	I	2.54	2	4	0.2739	650	15.8	0.05843	308	26.0	0.670	4.98	2.11	0.176	0.5 - 2.0	0.0 to 1.0
2	I	2.54	2	4	0.2856	651	16.3	0.1059	308	52.0	0.600	18.59	2.13	0.270	0.5 - 2.0	0.0 to 1.0
3	I	2.54	4	4	0.2657	649	15.2	0.03196	307	25.9	0.730	5.31	2.12	0.107	0.5 - 2.0	-0.5 to +0.5
4	I	2.54	4	4	0.2563	651	14.9	0.06072	304	52.2	0.675	23.51	2.17	0.191	0.5 - 2.0	-0.5 to +0.5
5	I	1.27	2	8	0.2604	649	15.0	0.05285	308	51.9	0.600	22.32	2.13	0.169	0.5 - 2.0	0.0 to 1.0
6	I	1.27	2	8	0.2655	650	15.1	0.1148	299	103.6	0.605	92.63	2.29	0.302	0.5 - 2.0	0.0 to 1.0
7	I	1.27	4	8	0.2630	651	15.2	0.0308	302	52.8	0.610	28.37	2.19	0.105	0.5 - 2.0	-0.5 to +0.5
8	I	1.27	4	8	0.2623	649	15.1	0.05791	299	104.1	0.605	96.00	2.30	0.181	0.5 - 2.0	-0.5 to +0.5
9	I	2.54	2	4	0.6207	306	15.4	0.1390	511	109.4	0.610	22.69	0.62	0.183	0.5 - 2.0	0.0 to 1.0
10	I	2.54	4	4	0.6327	293	15.2	0.07215	408	103.3	0.600	22.63	0.66	0.102	0.5 - 2.0	-0.5 to +0.5
11	I	1.27	2	8	0.6393	290	15.2	0.07298	445	102.2	0.600	22.33	0.67	0.102	0.5 - 2.0	-0.5 to +0.5
12	I	1.27	4	8	0.6311	293	15.3	0.04147	457	97.6	0.650	22.68	0.65	0.062	0.5 - 2.0	0.0 to 1.0

TABLE A-2. PHASE I, SERIES 2 TEST CONFIGURATIONS AND FLOW CONDITIONS.

PHASE I SERIES 2 TESTS

Test No.	Test Section	Orifice Dia (CM)	$\frac{S}{D}$	$\frac{H_0}{D}$	Mainstream			Dilution Jet				Momentum Flux Ratio (J)	Density Ratio (Denratio)	Equilibrium Theta (Theb)	Regions of Measurement	
					Mass Flow Rate (KG/S)	Temp (Tmain) (K)	Velocity (Vmain) (M/S)	Mass Flow Rate (KG/S)	Temp (Tjet) (K)	Velocity (Vjet) (M/S)	$C_{DJ}$				Axial Direction (X/H <sub>0</sub> )	Transverse Direction (Z/S)
13	I	2.54	2	4	0.2815	524	16.9	0.1277	294	59.7	0.610	31.79	1.81	0.312	0.5 - 2.0	0.0 to 1.0
14	I	2.54	4	4	0.2572	672	15.4	0.03311	305	28.4	0.682	6.70	2.21	0.114	0.5 - 2.0	-0.5 to +0.5
15	I	1.27	2	8	0.2777	616	15.5	0.1206	297	109.3	0.597	99.21	2.07	0.303	0.5 - 2.0	-0.5 to +0.5
16	I	1.27	4	8	0.3134	567	18.1	0.03465	311	63.0	0.670	24.38	1.86	0.100	0.5 - 2.0	0.0 to 1.0
17	I	2.54	2	4	0.3067	538	16.5	0.1347	303	57.9	0.675	24.45	1.80	0.305	0.5 - 2.0	0.0 to 1.0
18	I	1.27	4	8	0.3394	545	18.2	0.04052	317	72.2	0.675	29.55	1.76	0.107	0.5 - 2.0	-0.5 to +0.5

TABLE A-3. PHASE I, SERIES 3 TEST CONFIGURATIONS AND FLOW CONDITIONS.

PHASE I SERIES 3 TESTS

Test No.	Test Section	Orifice Dia (CM)	$\frac{S}{D}$	$\frac{H_0}{D}$	Mainstream			Dilution Jet				Momentum Flux Ratio (J)	Density Ratio (Denratio)	Equilibrium Theta (Theb)	Regions of Measurement	
					Mass Flow Rate (KG/S)	Temp (Tmain) (K)	Velocity (Vmain) (M/S)	Mass Flow Rate (KG/S)	Temp (Tjet) (K)	Velocity (Vjet) (M/S)	$C_{DJ}$				Axial Direction (X/H <sub>0</sub> )	Transverse Direction (Z/S)
19	II	1.27	4	8	0.2537	656	15.9	0.02994	330	58.1	0.650	27.07	2.02	0.106	0.25 - 2.0	0.0 to 1.0
20	II	1.27	4	8	0.2543	645	15.5	0.05892	314	106.4	0.630	102.5	2.19	0.188	0.25 - 2.0	0.0 to 1.0
21	II	2.54	2	4	0.2531	654	15.8	0.06222	308	28.1	0.660	6.76	2.13	0.197	0.50 - 2.0	0.0 to 1.0
22	II	2.54	2	4	0.2534	654	15.8	0.1125	304	54.5	0.600	26.07	2.18	0.307	0.50 - 2.0	0.0 to 1.0
23	IV	1.27	4	8	0.2775	646	17.0	0.02988	312	53.8	0.660	21.05	2.10	0.097	0.25 - 1.0	-0.5 to +0.5
24	IV	1.27	4	8	0.2772	643	16.9	0.06006	311	105.1	0.640	85.81	2.07	0.178	0.25 - 1.0	-0.5 to +0.5
25	IV	2.54	2	4	0.2462	643	15.1	0.05513	322	27.7	0.620	6.73	2.00	0.183	0.50 - 1.0	0.0 to 1.0
26	IV	2.54	2	4	0.2452	641	14.9	0.1045	330	55.1	0.600	26.73	1.96	0.299	0.50 - 1.0	0.0 to 1.0
27	V	1.27	4	8	0.2619	646	16.1	0.03122	320	58.7	0.650	27.18	2.05	0.107	0.25 - 1.0	0.0 to 1.0
28	V	1.27	4	8	0.2609	645	16.0	0.06071	319	112.5	0.625	106.7	2.02	0.189	0.25 - 1.0	0.0 to 1.0
29	V	2.54	2	4	0.2560	645	15.7	0.06334	314	29.1	0.660	7.07	2.06	0.198	0.50 - 1.0	-0.5 to +0.5
30	V	2.54	2	4	0.2542	646	15.6	0.1168	314	56.4	0.620	27.31	2.09	0.315	0.50 - 1.0	-0.5 to +0.5
31	VI	1.27	4	8	0.2649	649	16.4	0.03162	320	58.6	0.655	26.58	2.07	0.107	0.25 - 1.0	-0.5 to +0.5
32	VI	1.27	4	8	0.2687	647	16.5	0.06250	321	116.0	0.620	107.6	2.18	0.189	0.25 - 1.0	-0.5 to +0.5
33	VI	2.54	2	4	0.2646	650	16.3	0.06489	301	29.5	0.640	7.04	2.17	0.197	0.50 - 1.0	-0.5 to +0.5
34	VI	2.54	2	4	0.2629	651	16.2	0.1205	297	55.9	0.610	26.36	2.23	0.314	0.50 - 1.0	-0.5 to +0.5

TABLE A-4. PHASE 1, SERIES 4 TEST CONFIGURATIONS AND FLOW CONDITIONS.

PHASE I SERIES 4 TESTS

Test No.	Test Section	Orifice Dia (CM)	$\frac{S}{D}$	$\frac{H_0}{D}$	Mainstream			Dilution Jet				Momentum Flux Ratio (J)	Density Ratio (Denratio)	Equilibrium Theta (Theb)	Regions of Measurement	
					Mass Flow Rate (KG/S)	Temp (Tmain) (K)	Velocity (Vmain) (M/S)	Mass Flow Rate (KG/S)	Temp (Tjet) (K)	Velocity (Vjet) (M/S)	CDJ				Axial Direction (X/H0)	Transverse Direction (Z/S)
35	V	1.27	4	8	0.3566	561	18.7	0.03971	308	70.9	0.650	26.13	1.86	0.100	0.25 - 1.0	0.0 to 1.0
36	V	1.27	4	8	0.3579	568	18.8	0.07689	305	139.1	0.600	105.7	2.01	0.177	0.25 - 1.0	0.0 to 1.0
37	V	1.27	4	8	0.3532	417	16.0	0.02419	319	40.7	0.725	11.27	1.32	0.064	0.25 - 1.0	0.0 to 1.0
38	V	1.27	4	8	0.3645	416	16.0	0.04355	315	75.4	0.660	40.18	1.36	0.107	0.25 - 1.0	0.0 to 1.0



TABLE A-5. PHASE II, SERIES 5 TEST CONFIGURATIONS AND FLOW CONDITIONS.

PHASE II SERIES 5 TESTS

Test No.	Orifice Dia (CM)	S D	$\frac{H_0}{D}$	Mainstream			Top Dilution Jet					Bottom Dilution Jet					Equilibrium Theta (Theb)	Regions of Measurement	
				Mass Flow Rate (KG/S)	Temp (Tmain) (K)	Velocity (Vmain) (M/S)	Mass Flow Rate (KG/S)	Momentum Ratio JT	Temp (TJT) (K)	Velocity (VJT) (M/S)	(CD)T	Mass Flow Rate (KG/S)	Momentum Ratio JB	Temp (TJB) (K)	Velocity (VJB) (M/S)	(CD)B		Axial Direction X/H0	Transverse Direction (Z/S)
1	1.27	2 (INL)	8	0.2526	645.9	15.5	0.03109	6.81	310.4	28.1	0.665	0.03138	6.90	308.6	28.2	0.665	0.1983	0.25 - 2.0	-0.5 to +0.5
2	1.27	2 (INL)	8	0.2530	646.6	15.6	0.05893	24.94	306.8	53.3	0.650	0.0590	24.88	305.2	52.9	0.650	0.3179	0.25 - 2.0	-0.5 to +0.5
3	1.27	2 (INL)	8	0.2523	646.2	15.5	0.1204	101.8	303.9	104.3	0.640	0.1200	101.5	304.1	104.5	0.640	0.4879	0.25 - 2.0	-0.5 to +0.5
4	1.27	2 (STG)	8	0.2664	648.9	16.6	0.03118	6.52	325.7	30.0	0.660	0.03091	6.43	326.6	30.2	0.660	0.1890	0.25 - 2.0	-0.5 to 1.0
5	1.27	2 (STG)	8	0.2642	646.2	16.3	0.06199	25.15	314.5	56.7	0.660	0.06152	24.71	313.2	56.1	0.660	0.3186	0.25 - 2.0	-0.5 to 1.0
6	1.27	2 (STG)	8	0.2660	645.2	16.4	0.1252	99.23	313.5	110.2	0.650	0.1248	98.57	310.9	109.1	0.650	0.4845	0.25 - 2.0	-0.5 to 1.0
7	1.27	4 (INL)	8	0.2554	645.4	15.2	0.0159	7.23	326.3	30.2	0.670	0.01632	7.39	317.5	29.6	0.670	0.1121	0.25 - 2.0	-0.5 to +0.5
8	1.27	4 (INL)	8	0.2446	647.1	14.4	0.02952	25.74	322.2	54.5	0.650	0.02886	26.36	325.0	54.6	0.650	0.1896	0.25 - 2.0	-0.5 to +0.5
9	1.27	4 (INL)	8	0.2454	647.6	14.5	0.05932	108.2	319.8	107.7	0.650	0.05953	107.4	317.6	107.1	0.650	0.3291	0.25 - 2.0	-0.5 to +0.5
10	1.27	4 (STG)	8	0.2546	646.6	15.8	0.01435	5.97	329.1	27.6	0.670	0.01452	6.03	325.7	27.8	0.670	0.1019	0.25 - 2.0	-0.5 to 1.0
11	1.27	4 (STG)	8	0.2549	645.0	15.7	0.02974	25.57	322.2	55.8	0.660	0.02957	25.20	321.6	55.8	0.660	0.1888	0.25 - 1.0	-0.5 to 1.0
12	1.27	4 (STD)	8	0.2582	645.9	16.0	0.06076	103.0	317.9	109.9	0.640	0.0601	101.5	320.6	111.0	0.640	0.3187	0.25 - 2.0	-0.5 to 1.0

TABLE A-6. PHASE II, SERIES 6 TEST CONFIGURATIONS AND FLOW CONDITIONS.

PHASE II SERIES 6 TESTS

Test No.	Orifice Dia (CM)	$\frac{S}{D}$	$\frac{H_0}{D}$	Mainstream			Top Dilution Jet					Bottom Dilution Jet					Equilibrium Theta (Theb)	Regions of Measurement	
				Mass Flow Rate (KG/S)	Temp (Tmain) (K)	Velocity (Vmain) (M/S)	Mass Flow Rate (KG/S)	Momentum Ratio JT	Temp (TJT) (K)	Velocity (VJT) (M/S)	(CD)T	Mass Flow Rate (KG/S)	Momentum Ratio JB	Temp (TjB) (K)	Velocity (VJB) (M/S)	(CD)B		Axial Direction X/H0	Transverse Direction (Z/S)
13	1.27	<sup>2</sup> (INL)	8	0.3356	559.3	18.9	0.07235	27.49	309.9	69.3	0.620	0.07204	27.42	313.9	69.7	0.620	0.6402	0.25 - 2.0	-0.5 to +0.5
14	1.27	<sup>2</sup> (STG)	8	0.3346	553.9	19.0	0.03633	6.92	321.7	35.5	0.640	0.03712	6.96	329.7	36.4	0.660	0.5990	0.25 - 2.0	-0.5 to 1.0
15	1.27	<sup>2</sup> (STG)	8	0.3336	554.6	18.9	0.0716	27.42	318.5	69.6	0.630	0.07608	27.74	316.7	68.5	0.660	0.6541	0.25 - 2.0	-0.5 to 1.0
16	1.27	<sup>4</sup> (INL)	8	0.3269	549.9	18.6	0.03539	27.42	321.3	68.5	0.640	0.0361	27.70	330.7	70.0	0.655	0.6017	0.25 - 2.0	-0.5 to +0.5
17	1.27	<sup>4</sup> (STG)	8	0.3321	548.1	18.8	0.07975	27.71	315.4	68.7	0.636	0.08172	26.84	327.7	70.2	0.670	0.6004	0.25 - 2.0	-0.5 to 1.0
18	1.27	<sup>4</sup> (STG)	8	0.3347	551.1	18.9	0.07606	115.3	313.5	137.7	0.630	0.08041	115.1	315.6	135.2	0.655	0.6589	0.25 - 2.0	-0.5 to 1.0

TABLE A-7. PHASE II, SERIES 7 TEST CONFIGURATIONS AND FLOW CONDITIONS.

PHASE II SERIES 7 TESTS

Test No.	Orifice Dia (CM)	$\frac{S}{D}$	$\frac{H_0}{D}$	Mainstream			Top Dilution Jet					Bottom Dilution Jet					Equilibrium Theta (Theb)	Regions of Measurement	
				Mass Flow Rate (KG/S)	Temp (Tmain) (K)	Velocity (Vmain) (M/S)	Mass Flow Rate (KG/S)	Momentum Ratio JT	Temp (TJT) (K)	Velocity (VJT) (M/S)	(Cd)T	Mass Flow Rate (KG/S)	Momentum Ratio JB	Temp (TjB) (K)	Velocity (VJB) (M/S)	(Cd)B		Axial Direction X/H0	Transverse Direction (Z/S)
19	1.27	2 (INL)	8	0.2662	644.8	16.5	0.06453	25.97	298.2	56.5	0.650	0.0638	25.57	298.2	56.3	0.650	0.3253	0.25 - 1.0	-0.5 to +0.5
20	1.27	2 (INL)	8	0.2669	644.6	16.4	0.1340	106.5	297.0	111.3	0.650	0.1348	107.7	295.0	111.3	0.650	0.5019	0.25 - 1.0	-0.5 to +0.5
21	1.27	4 (STG)	8	0.2691	644.6	16.4	0.03155	25.92	302.9	57.1	0.640	0.03275	26.69	290.2	54.7	0.640	0.1929	0.25 - 1.0	-0.5 to 1.0
22	1.27	4 (STG)	8	0.2690	644.2	16.4	0.06504	107.7	298.5	112.8	0.630	0.06506	107.7	299.9	113.7	0.630	0.3260	0.25 - 1.0	-0.5 to 1.0
23	2.54	4 (STG)	4	0.2681	644.9	16.5	0.03311	6.78	311.0	29.7	0.670	0.03367	6.75	310.4	30.0	0.680	0.1994	0.25 - 1.0	-0.5 to 1.0
24	2.54	4 (STG)	4	0.2683	644.5	16.4	0.06359	25.76	304.2	56.9	0.650	0.0669	26.0	301.1	56.7	0.675	0.3272	0.25 - 1.0	-0.5 to 1.0
25	2.54	2 (INL)	4	0.2675	645.1	16.4	0.06522	6.67	300.4	28.9	0.655	0.06554	6.70	298.9	28.9	0.655	0.3284	0.25 - 1.0	-0.5 to +0.5
26	2.54	2 (INL)	4	0.2684	644.7	16.4	0.1238	25.58	300.8	56.4	0.630	0.1250	25.90	298.9	56.6	0.630	0.4810	0.25 - 1.0	-0.5 to +0.5

TABLE A-8. PHASE II, SERIES 8 TEST CONFIGURATIONS AND FLOW CONDITIONS.

PHASE II SERIES 8 TESTS

Test No.	Test Section	Orifice Dia (CM)	$\frac{S}{D}$	$\frac{H_0}{D}$	Mainstream			Top Dilution Jet					Bottom Dilution Jet					Equilibrium Theta (Theb)	Regions of Measurement	
					Mass Flow Rate (KG/S)	Temp (Tmain) (K)	Velocity (Vmain) (M/S)	Mass Flow Rate (KG/S)	Momentum Ratio JT	Temp (TJT) (K)	Velocity (VJT) (M/S)	(CD) <sub>T</sub>	Mass Flow Rate (KG/S)	Momentum Ratio JB	Temp (TJB) (K)	Velocity (VJB) (M/S)	(CD) <sub>B</sub>		Axial Direction X/H <sub>0</sub>	Transverse Direction (Z/S)
27	I	2.54	4 (STG)	4	0.2719	646.3	16.6	0.03314	6.75	313.4	30.1	0.665	0.03455	6.82	305.0	29.5	0.680	0.1993	0.25 - 2.0	-0.5 to 1.0
28	I	2.54	4 (STG)	4	0.2747	644.7	16.9	0.06534	26.41	307.4	59.4	0.650	0.06823	26.27	303.6	58.6	0.670	0.3271	0.25 - 2.0	-0.5 to 1.0
29	I	2.54	4 (INL)	4	0.2681	645.4	16.5	0.06407	26.85	307.5	58.6	0.645	0.06515	27.05	300.6	57.4	0.645	0.3253	0.25 - 2.0	-0.5 to +0.5
30	I	2.54	4 (INL)	4	0.2700	645.4	16.6	0.1306	106.9	306.9	114.9	0.640	0.1324	107.0	304.8	113.6	0.640	0.4936	0.25 - 2.0	-0.5 to +0.5
31a	I	0.5144	1	19.75	0.2739	646.0	16.8	0.03782	6.69	310.5	29.9	0.750	---	---	---	---	---	0.1213	0.25 - 2.0	0 to 40
31b	I	0.5144	1	19.75	0.2720	646.7	16.7	0.07358	26.36	308.6	21.33	0.735	---	---	---	---	---	0.2129	0.25 - 2.0	0 to 40
31c	I	0.5144	1	19.75	0.2747	646.3	16.8	0.1492	105.4	305.1	113.8	0.715	---	---	---	---	---	0.3520	0.25 - 2.0	0 to 40
32	I	2.25	2 (INL)	4	0.2732	646.5	16.8	0.06414	24.23	311.0	59.1	0.670	---	---	---	---	---	0.1902	0.25 - 2.0	-0.5 to +0.5
33	I	1.27	2 (INL)	8	0.2713	645.1	16.6	0.07874	40.87	303.7	72.3	0.630	0.04895	15.20	299.1	43.2	0.640	0.3201	0.25 - 2.0	-0.5 to +0.5
34	I	1.27	2 (INL)	8	0.2703	645.3	16.6	0.09437	58.36	303.2	85.7	0.630	0.03289	6.77	300.6	28.7	0.650	0.3201	0.25 - 1.0	-0.5 to +0.5
35	III	1.27	2 (INL)	8	0.2684	645.0	16.4	0.06265	26.20	303.4	57.2	0.630	0.06279	26.12	301.0	56.7	0.630	0.3185	0.25 - 1.0	-0.5 to +0.5
36	III	1.27	2 (INL)	8	0.2698	644.5	16.4	0.1300	106.9	301.1	112.8	0.630	0.1294	106.4	301.6	113.4	0.630	0.4902	0.25 - 1.0	-0.5 to +0.5
37	III	1.27	4 (STG)	8	0.2683	645.6	16.4	0.03104	25.68	310.7	57.5	0.640	0.03115	25.67	309.0	57.7	0.640	0.1882	0.25 - 1.0	-0.5 to 1.0
38	III	1.27	4 (STG)	8	0.2680	645.6	16.4	0.06494	108.8	303.3	113.8	0.630	0.06379	105.8	303.3	113.8	0.630	0.3245	0.25 - 1.0	-0.5 to 1.0
39	III	2.54	4 (STG)	4	0.2707	645.6	16.5	0.03352	6.69	311.9	29.7	0.675	0.0339	6.75	307.5	29.5	0.675	0.1994	0.25 - 1.0	-0.5 to 1.0
40	III	2.54	4 (STG)	4	0.2727	645.7	16.6	0.06481	25.95	302.7	57.4	0.645	0.06635	26.34	293.6	55.4	0.645	0.3247	0.25 - 1.0	-0.5 to 1.0
41	III	2.54	2 (INL)	4	0.2723	645.6	16.5	0.06612	6.62	305.5	29.2	0.660	0.06633	6.65	304.9	29.3	0.660	0.3272	0.25 - 1.0	-0.5 to +0.5
42	III	2.54	2 (INL)	4	0.2726	645.8	16.4	0.1248	26.12	302.5	57.2	0.620	0.1243	26.0	303.0	57.4	0.620	0.4774	0.25 - 1.0	-0.5 to +0.5

TABLE A-8. PHASE II, SERIES 8 TEST CONFIGURATIONS AND FLOW CONDITIONS (CONTINUED).

PHASE II SERIES 8 TESTS

Test No.	Test Section	Orifice Dia (CM)	$\frac{S}{D}$	$\frac{H_0}{D}$	Mainstream			Top Dilution Jet					Bottom Dilution Jet					Equilibrium Theta (Theb)	Regions of Measurement	
					Mass Flow Rate (KG/S)	Temp (Tmain) (K)	Velocity (Vmain) (M/S)	Mass Flow Rate (KG/S)	Momentum Ratio $J_T$	Temp (TJT) (K)	Velocity (VJT) (M/S)	(CD) <sub>T</sub>	Mass Flow Rate (KG/S)	Momentum Ratio $J_B$	Temp (Tjb) (K)	Velocity (Vjb) (M/S)	(CD) <sub>B</sub>		Axial Direction X/H <sub>0</sub>	Transverse Direction (Z/S)
43	III	2.54	2	4	0.3348	506.5	17.9	0.07832	7.79	310.2	34.9	0.665	--	--	--	--	--	0.5873	0.25 - 1.0	-0.5 to +0.5
44	III	2.54	2	4	0.3350	508.4	17.9	0.1526	30.00	307.9	67.9	0.650	--	--	--	--	--	0.6460	0.25 - 1.0	-0.5 to +0.5
45a	I	1.024	1	9.92	0.2688	644.7	16.5	0.0749	6.66	307.8	29.4	0.750	--	--	--	--	--	0.2179	0.25 - 2.0	0.0 to 4.0
45b	I	1.024	1	9.92	0.2708	644.4	16.6	0.1434	25.33	308.7	57.3	0.725	--	--	--	--	--	0.3462	0.25 - 2.0	0.0 to 4.0
45c	I	1.024	1	9.92	0.2735	644.9	16.7	0.2545	78.20	307.5	98.9	0.710	---	---	---	---	---	0.4820	0.25 - 2.0	0.0 to 4.0
46	I	2.54	2 (INL)	4	0.2707	644.3	16.5	0.06667	6.70	304.8	29.4	0.665	0.06656	6.67	304.6	29.4	0.665	0.3299	0.25 - 2.0	-0.5 to +0.5
47	I	2.54	2 (INL)	4	0.2710	644.3	16.6	0.1276	25.54	302.2	57.0	0.645	0.1273	25.52	303.6	57.3	0.645	0.4846	0.25 - 2.0	-0.5 to +0.5
48	I	2.54	2 (INL)	4	0.2710	644.1	16.5	0.2334	84.14	302.5	101.4	0.640	0.2334	84.04	302.5	101.2	0.640	0.6327	0.25 - 2.0	-0.5 to +0.5
49	I	1.80	2.83	5.67	0.2701	644.4	16.7	0.03539	6.49	309.5	29.4	0.725	---	---	---	---	---	0.1159	0.25 - 2.0	-0.5 to +0.5
50	I	1.80	2.83	5.67	0.2679	644.9	16.5	0.06924	25.46	299.5	56.3	0.705	--	--	--	--	--	0.2054	0.25 - 2.0	-0.5 to +0.5
51	I	2.54	4 (INL)	4	0.2679	644.3	16.5	0.03334	6.67	305.6	29.2	0.675	0.03421		295.8	28.6		0.2014	0.25 - 1.0	-0.5 to +0.5

REPORT DOCUMENTATION PAGE			Form Approved OMB No. 0704-0188	
Public reporting burden for this collection of information is estimated to average 1 hour per response, including the time for reviewing instructions, searching existing data sources, gathering and maintaining the data needed, and completing and reviewing the collection of information. Send comments regarding this burden estimate or any other aspect of this collection of information, including suggestions for reducing this burden, to Washington Headquarters Services, Directorate for Information Operations and Reports, 1215 Jefferson Davis Highway, Suite 1204, Arlington, VA 22202-4302, and to the Office of Management and Budget, Paperwork Reduction Project (0704-0188), Washington, DC 20503.				
1. AGENCY USE ONLY (Leave blank)		2. REPORT DATE June 1985		3. REPORT TYPE AND DATES COVERED Final Contractor Report
4. TITLE AND SUBTITLE  Dilution Jet Mixing Program Phase III Report			5. FUNDING NUMBERS  WU-None NAS3-22110	
6. AUTHOR(S)  R. Srinivasan, G. Myers, E. Coleman, and C. White				
7. PERFORMING ORGANIZATION NAME(S) AND ADDRESS(ES)  Garrett Turbine Engine Company P.O. Box 5217 Phoenix, Arizona 85010			8. PERFORMING ORGANIZATION REPORT NUMBER  E-None	
9. SPONSORING/MONITORING AGENCY NAME(S) AND ADDRESS(ES)  National Aeronautics and Space Administration Washington, DC 20546-0001			10. SPONSORING/MONITORING AGENCY REPORT NUMBER  NASA CR-174884 Garrett 21-5418	
11. SUPPLEMENTARY NOTES  Project Manager, James D. Holdeman, NASA Lewis Research Center, Cleveland, Ohio 44135.				
12a. DISTRIBUTION/AVAILABILITY STATEMENT  Unclassified - Unlimited Subject Category: 00  Available electronically at <a href="http://gltrs.grc.nasa.gov">http://gltrs.grc.nasa.gov</a> This publication is available from the NASA Center for AeroSpace Information, 301-621-0390.			12b. DISTRIBUTION CODE	
13. ABSTRACT (Maximum 200 words)  The main objectives of the NASA Dilution Jet Mixing Phase III Program were as follows: 1) Extend the data base on the mixing of single-sided rows of jets in a confined cross flow to discrete slots, including streamlined, bluff, and angled injections; 2) Quantify the effects of geometrical and flow parameters on penetration and mixing of multiple rows of jets into a confined cross flow. Investigate in-line, staggered, and dissimilar hole configurations; 3) Determine the effects of unequal flow rates through the axially staged jets; and 4) Develop empirical correlations for predicting temperature distributions for discrete slots and multiple rows of dilution holes.				
14. SUBJECT TERMS  Dilution-zone; Jet-mixing; Combustion			15. NUMBER OF PAGES 138	
			16. PRICE CODE	
17. SECURITY CLASSIFICATION OF REPORT Unclassified	18. SECURITY CLASSIFICATION OF THIS PAGE Unclassified	19. SECURITY CLASSIFICATION OF ABSTRACT Unclassified	20. LIMITATION OF ABSTRACT	